Dynamics of vortices in complex wakes: modeling, analysis, and experiments

Saikat Basu

Dissertation submitted to faculty of
Virginia Polytechnic Institute and State University
in partial fulfillment of the requirements for the degree of

Doctor of Philosophy
in
Engineering Mechanics

Mark A. Stremler, Chair
Saad A. Ragab
Shane D. Ross
Sunghwan Jung
Traian Iliescu

April 03, 2014
Blacksburg, Virginia

Keywords: Vortex dynamics, Point vortices, Bluff body wake, Fluid-structure interactions, Vortex-induced vibrations

Dynamics of vortices in complex wakes: modeling, analysis, and experiments

Saikat Basu

(ABSTRACT)

The thesis develops singly-periodic mathematical models for complex laminar wakes which are formed behind vortex-shedding bluff bodies. These wake structures exhibit a variety of patterns as the bodies oscillate or are in close proximity of one another. The most well-known formation comprises two counter-rotating vortices in each shedding cycle and is popularly known as the von Kármán vortex street. Of the more complex configurations, as a specific example, this thesis investigates one of the most commonly occurring wake arrangements, which consists of two pairs of vortices in each shedding period. The paired vortices are, in general, counter-rotating and belong to a more general definition of the 2P mode, which involves periodic release of four vortices into the flow. The 2P arrangement can, primarily, be sub-classed into two types: one with a symmetric orientation of the two vortex pairs about the streamwise direction in a periodic domain and the other in which the two vortex pairs per period are placed in a staggered geometry about the wake centerline. The thesis explores the governing dynamics of such wakes and characterizes the corresponding relative vortex motion.

In general, for both the symmetric as well as the staggered four vortex periodic arrangements, the thesis develops two-dimensional potential flow models (consisting of an integrable Hamiltonian system of point vortices) that consider spatially periodic arrays of four vortices with their strengths being $\pm\Gamma_1$ and $\pm\Gamma_2$. Vortex formations observed in the experiments inspire the assumed spatial symmetry. The models demonstrate a number of dynamic modes that are classified using a bifurcation analysis of the phase space topology, consisting of level curves of the Hamiltonian. Despite the vortex strengths in each pair being unequal in magnitude, some initial conditions lead to relative equilibrium when the vortex configuration moves with invariant size and shape.

The scaled comparisons of the model results with experiments conducted in a flowing soap film with an airfoil, which was imparted with forced oscillations, are satisfactory and validate the reduced order modeling framework. The experiments have been performed by a collaborator group at the Department of Physics and Fluid Dynamics at the Technical University of Denmark (DTU), led by Dr. Anders Andersen. Similar experiments have also been run at Virginia Tech as part of this dissertation and the preliminary results are included in this treatise.

The thesis also employs the same dynamical systems techniques, which have been applied to study the 2P regime dynamics, to develop a mathematical model for the P+S mode vortex wakes, with three vortices present in each shedding cycle. The model results have also been compared favorably with an experiment and the predictions regarding the vortex circulation data match well with the previous results from literature.

Finally, the thesis introduces a novel concept of clean and renewable energy extraction from vortex-induced vibrations of bluff bodies. The slow-moving currents in the off-shore marine environments and riverine flows are beyond the operational capabilities of the more established hydrokinetic energy converters and the discussed technology promises to be a significant tool to generate useful power from these copiously available but previously untapped sources.

Dedicated to my parents Anindita Basu and Subrata Basu,
and to my younger brother Swastik Basu

Acknowledgements

First of all, I must acknowledge and thank my parents, Anindita Basu and Subrata Basu, for being the greatest inspiration and for being a constant support. None of my academic or non-academic pursuits and achievements would have been possible without them on my side. Two of the other most significant persons in my life are my younger brother Swastik Basu and my grandmother Bhabani Nandini Kar, and I owe a lot to them. Acknowledgements are also due to my uncle Abhijit Kar, my aunt Anamika Ray, my late grandmother Gayatri Basu, my grandfather Satindra Nath Bose, my late grandfather Ajit Kumar Kar, and my late uncle Samar Basu.

I also most importantly thank my doctoral advisor Dr. Mark A. Stremler for the guidance I have received from him over the last four and half years. Dr. Stremler has been a friend, a teacher, and a mentor to me. I feel sheerly blessed to have pursued such an important phase of my academic career under his resourceful tutelage. I would also thank my doctoral committee members Dr. Saad A. Ragab, Dr. Shane D. Ross, Dr. Sunghwan Jung, and Dr. Traian Iliescu for graciously agreeing to be on my committee and for extending help and guidance whenever I needed them. I also express my heartfelt regards to late Professor Hassan Aref. I have learnt a lot about my research topic by being a student in a vortex dynamics course which he had taught at Virginia Tech (Spring 2011) and by perusing his mathematically exquisite journal articles. I also take this opportunity to thank the professors at my undergraduate alma mater Jadavpur University (Kolkata, India). Here special mention should be made of Dr. Debasish Roy, Dr. Partha Bhattacharya, and Dr. Somnath Ghosh. And, I sincerely thank all the graduate students at Virginia Tech with whom I have collaborated at various phases of my doctoral years. Most notable among them are Gary Nave, Wenchao Yang, Sean Gart, and Alireza Salmanzadeh. My former lab-colleagues Pradeep Rao and Pankaj Kumar also deserve mention in this regard. Discussions with them helped me appreciate many of the finer nuances of my research. I also extend my utmost thanks to the staff-members at the Department of Engineering Science and Mechanics, more specifically Sally Shrader and Lisa L. Smith for helping me out with the various administrative details.

Finally, I forward my sincere thanks to my old friends from high school and college: Samrat Mandal, Abhishek Mondal, Olive Sen, and Shamik Bhadra. At Virginia Tech, I specifically thank Saikat Jana, Souvick Chatterjee, Arnab Roy, Arnab Gupta, and Brato Chakrabarti for helping me out with their technical expertise at various stages of my doctoral research. I also thank my numerous other friends and colleagues in Blacksburg; including Anupam Pandey, Suvojit Ghosh, Hossain Aziz, Wrik Mallik, Abhijit Sarkar, Bikramjit Mukherjee, Souvik Pal, Shibabrat Naik, and Surya Deb for all the fun and companionship.

Saikat Basu
Blacksburg, Virginia, USA *April, 2014*

Contents

Vortex wakes behind bluff bodies in flows - Painted by Leonardo da Vinci (1513)

List of Figures

List of Tables

Chapter 1

Introduction

1.1 Thesis overview

Wakes consisting of distinctly identifiable vortex structures occur in flows over an extensive range of Reynolds numbers (see Fig. 1.1 for representative complicated wake configurations generated in soap films by altering the flow parameters). A classical example is the von Kármán vortex street, which has a pair of counter-rotating vortices in each shedding cycle of the bluff body. Vortex generation and the subsequent wake evolution constitute important aspects of the fluid-structure interaction problems at intermediate and high Reynolds numbers. A better understanding of the dynamics that govern the wakes is a key to answering a wide spectrum of questions ranging from what are the possible effects of the surrounding flows on offshore structures to how the fish generates propulsive forces during its swimming. Applications can be both typical as well as quite novel. Designing small-scale bio-inspired or biomimetic flights and development of energy harvesting mechanisms utilizing the mechanical energy from the vortex induced vibrations of the wake-shedding structures are some significant examples. The wakes generated in the flow are frequently quite complex as far as the arrangement of vortices is concerned. However, despite all these, the staggered vortex street model [10, 11, 12] developed by von Kármán in 1911-12 still stays as an important modeling tool to study and predict the effects of vortex wakes. The simplistic arrangement of the wake vortices assumed in von Kármán's work, despite the presence of a number of complicated wake geometries, serves as a motivation to build a more robust analytical theory for the fully developed complex vortex wakes.

The primary objectives of this doctoral thesis are to establish a reduced order mathematical model to predict and characterize the dynamics of complex, vortex-dominated bluff body wakes; to validate the modeling framework through comparisons with experimental wakes; and to explore the wake-induced dynamic response of the bodies generating such wakes.

Hence, development of a robust mathematical model, which will enable a better understanding of complex vortex wake dynamics, constitutes the main essence of this dissertation. The three key aspects that will be addressed in the treatise are as follows:

- Characterization of the dynamics of wakes comprising distinct vortex structures.
- Validation of the modeling approach by comparing the model results with experiments.
- Insight into the body-wake interaction phenomena and the resulting applications.

As specific examples, the thesis employs tools of dynamical systems theory to develop mathematical models for wake arrangements with four vortices in each shedding period. Comprising of two pairs of counter-rotating vortices, they can be of two types when the pairs of vortices are placed symmetrically (*symmetric four vortex wake*) about the wake centerline or are arranged in a staggered orientation (*staggered four vortex wake*). After the well-known

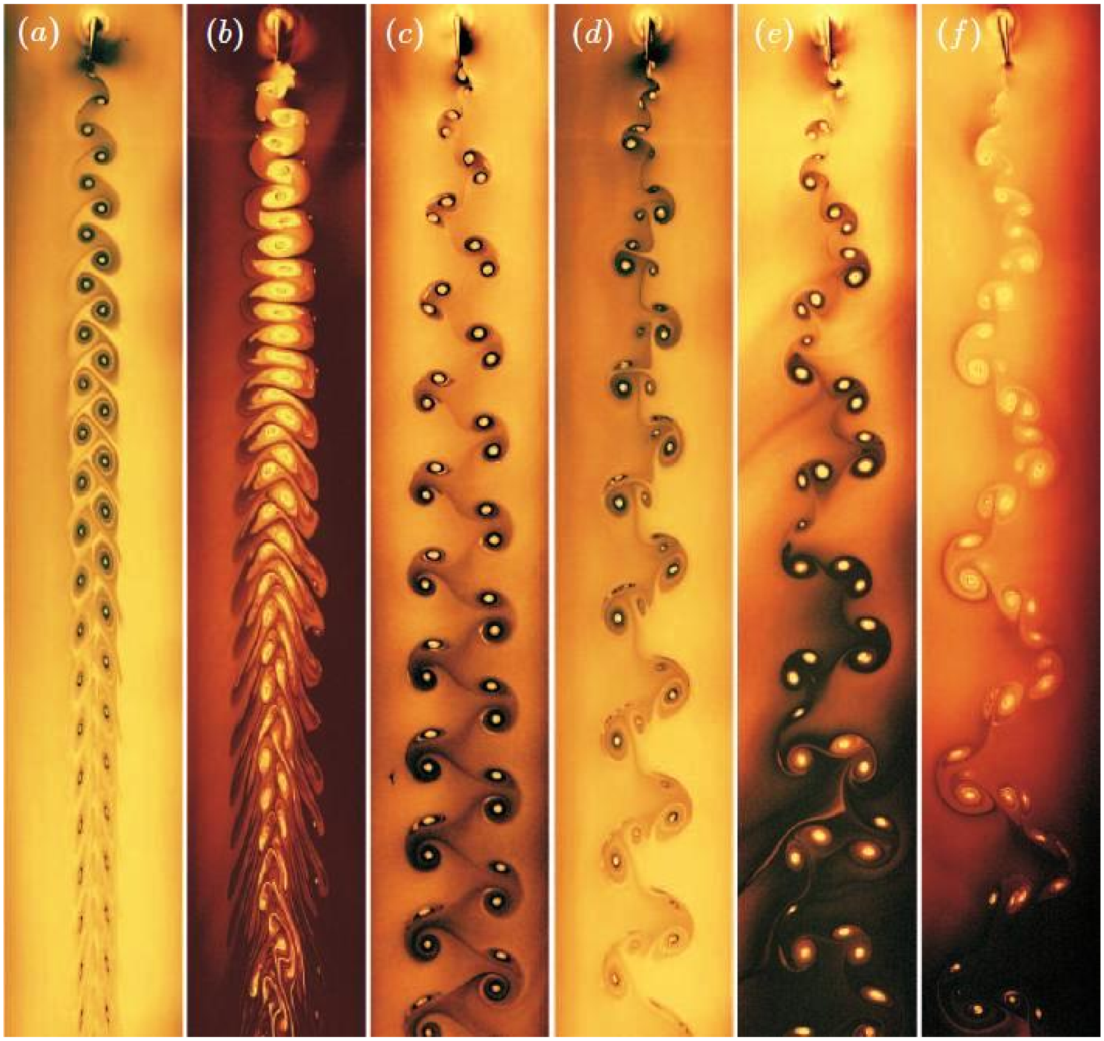

Figure 1.1: Varying wake geometries generated by a flapping foil on a thin flowing soap film by altering the oscillation frequencies and amplitudes, and the background flow velocities [1]. Original image is provided by A. Andersen (DTU, Denmark).

von Kármán street, this is the most commonly occurring [13] wake structure behind oscillating objects. Similar techniques are also applied to study the dynamics of vortex wakes with three vortices per shedding cycle.

To summarize, the rest of the dissertation has been arranged into the following segments:

- §1.2 of the current Chapter 1 discusses the commonly observed vortex wake patterns and then establishes the mathematical framework for modeling periodic vortex wakes with a point vortex approximation.

- Chapter 2 introduces the reduced order modeling approach and develops the mathematical model for the symmetric four vortex wake.
- Chapter 3 outlines the development of the mathematical model for the staggered four vortex wake. It further discusses and characterizes the different categories of relative vortex motion that are possible in the model.
- Chapter 4 presents the comparison of the model results with experimentally observed wakes.
- Chapter 5 illustrates the applicability of the same modeling tools for wake arrangements with three vortices per period.
- Chapter 6 comprises two sections on some significant application areas of vortex wake analysis. §6.1 describes an energy harvesting mechanism from vortex-induced vibrations of a bluff body. §6.2 discusses experiments performed in laminar soap film flows involving wake-structure interactions.
- Chapter 7 summarizes the comprehensive impacts and ramifications expected from this thesis work.

1.2 Governing principles

Vortex wakes are formed behind bluff bodies when they are submerged in a free stream of viscous fluid moving with a velocity, say, U. In general, such a wake represents the standard von Kármán vortex street [10, 11, 12], with two counter-rotating vortices per shedding cycle.

This has been identified as the 2S mode[1], in accordance with the nomenclature of [2]. For such a wake, the relative vortex spacing stays essentially conserved as the vortices progress downstream. More complex wake patterns, with vortex positions evolving dynamically, are exhibited when the bodies move and/or oscillate with respect to the oncoming fluid stream, or are placed in closed proximity to one another. In many cases these patterns consist of regular groupings of four vortices [13], broadly classified as the 2P mode. In general, the 2P wake regime[2] can be classified into two types with the two vortex pairs being arranged symmetrically or staggered about the wake centerline. Each of the vortex pairs in these two arrangements consists of two counter-rotating vortices. In addition, the 2C wake[3] with two pairs of co-rotating vortices in each shedding cycle is considered to be a special case in the general definition for the 2P wake mode. As examples, 2P configurations with counter-rotating vortex pairs have been observed behind vibrating airfoils [1, 5], oscillating cylinders [14], and elastic membranes [15]. It has also been seen in the biological world, for example in the wake of a swimming zebra fish larva [16]. As for 2C wakes, experimental generation of it behind two closely spaced stationary circular cylinders can be traced back to [17]. Such a configuration is also observed for vortex-induced vibrations behind a pivoted cylinder [18].

Two examples of exotic wakes are shown in Fig. 1.2(a,b). The first example shows the wake generated by pulling a cylinder through water along a sinusoidal path, with three vortices generated during each shedding cycle. The vortices from each cycle interact as a pair of counter-rotating vortices and a single, somewhat isolated vortex, leading to this configuration being labeled a 'P+S' wake[4] [2]. The second example shows the wake generated

---

[1] The nomenclature symbol 'S' signifies the presence of one *single* vortex per cycle. Therefore, '2S' implies two vortices per shedding period.

[2] The nomenclature symbol 'P' signifies the presence of a *pair* of vortices per cycle. Therefore, '2P' implies two vortex pairs in each period.

[3] The nomenclature symbol 'C' here stands for the *co-rotating* nature of two vortices in each pair.

[4] Going by the established nomenclature implication for 'P' and 'S', the term 'P+S' implies one *pair* of vortices along with another *single* vortex in each shedding period of the wake.

in a vertically-flowing soap film as it moves past a flapping foil, with four vortices being shed into the flow during each oscillation cycle. These four vortices move as two counter-rotating pairs, giving what has been termed in the previous paragraph as a '2P' wake [2]. In both of these examples, there is substantially more relative motion of the vortices than is seen in the standard Kármán street, or '2S' wake, in which two vortices are generated during each shedding cycle, as shown in Fig. 1.2(c).

The point vortex model as a tool to study vortex wakes was famously used by von Kármán [10] in his model for the 2S wake mode. This two-dimensional potential flow model consists of two point vortices having equal and opposite strengths $\pm\Gamma$, placed at staggered locations within a singly periodic strip of width L. This point vortex system is in unstable relative equilibrium and the vortices translate downstream with constant inter-vortex separation. The least unstable states are given by the Dolaptschiew-Maue criterion [19]

$$\sinh(\pi b/L) = \sin(\pi a/L), \tag{1.1}$$

where a and b represent respectively the streamwise and the spanwise separations between the alternating vortices. The famous stability criterion $\sinh(\pi b/L) = 1$ (see [11]) can be derived from equation (1.1) by substituting $a = L/2$, i.e. when oblique motion is absent. Despite the progress in experimental and computational analysis of vortex wakes since then, the efficacy of a reduced order model to study vortex wakes is still significant as it can provide valuable insight into the evolving wake dynamics. For more exotic wakes, such a point vortex model must also allow for a relative motion of the vortices. If the wake consists of regular groupings of three vortices (P+S mode wake), a spatially periodic point vortex model [20] has been demonstrated to give a qualitative representation of the relative vortex dynamics. This thesis aims to utilize the same idea by setting up a point vortex model for other complex wake geomteries involving more number of vortices per shedding period.

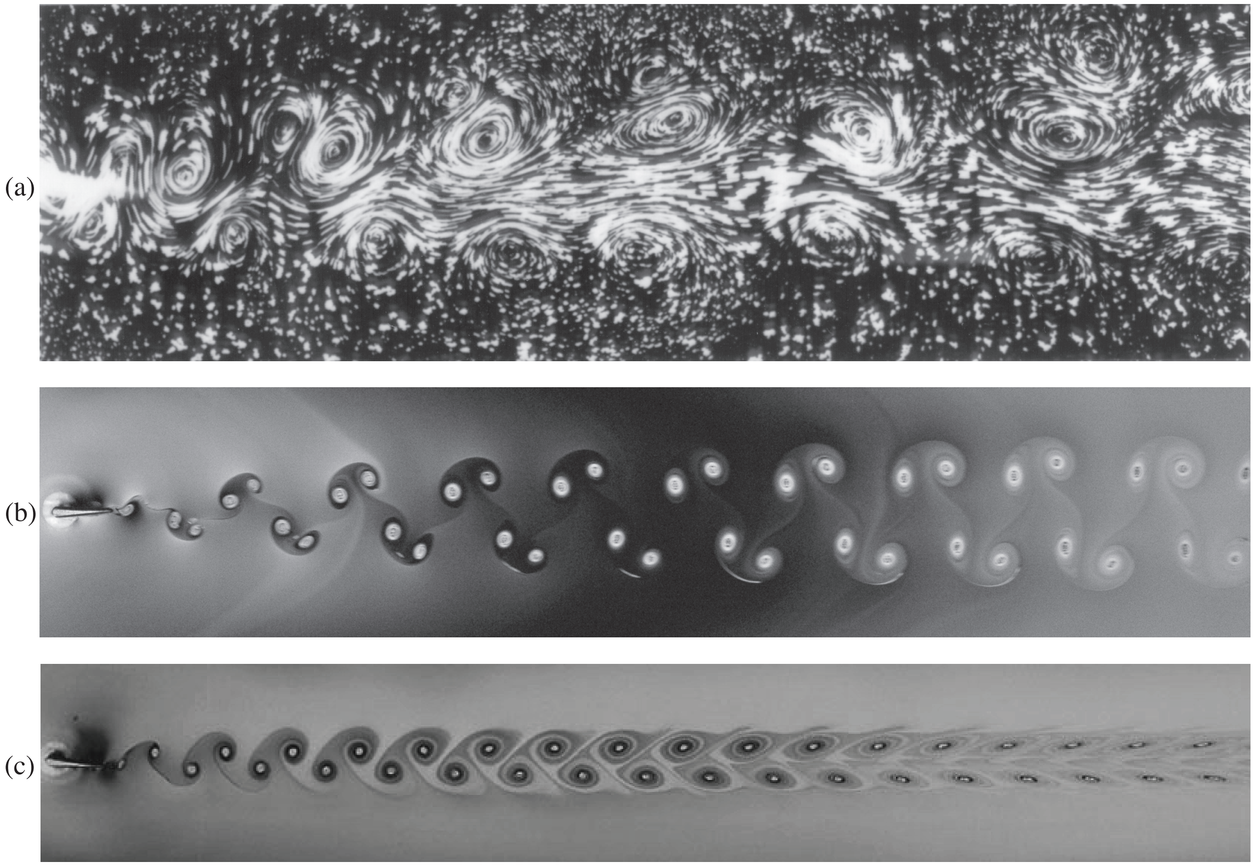

Figure 1.2: Examples of exotic wakes behind an oscillating body. Flow with respect to the body is from left to right. (a) P+S wake in water generated by a circular cylinder that was pulled left to right, from [2]; original image provided by A. Roshko. (b) 2P wake in a flowing soap film generated by a symmetrical foil that was flapped about a point near its leading edge, from [3]; original image provided by A. Andersen. (c) 2S wake in a flowing soap film generated by a symmetric foil that was flapped about a point near its leading edge, from [1].

The current treatise focus is on the considerable length of the mid-wake region where the vortex centers form a distinct street configuration. There is indeed some viscous dissipation as the vortices propagate downstream, but the reduction in the vortex circulations is not appreciable untill a significant distance and although the idealization of point vortices becomes increasingly unrealistic as we move further downstream, the present results demonstrate that the dynamics in the mid-wake region of the vortex street is fairly well-represented by the proposed model.

1.2.1 Equations of point vortex motion in periodic domains

To model the complex vortex wakes in periodic domains, the starting point for this treatise is the same as that introduced by von Kármán: an infinite system of point vortices is assumed to represent a finite wake in the region where the vortices form a distinct street-like configuration. In von Kármán's case, the experimental vortices show very little relative motion, so the full mid-wake region is reasonably well approximated by a spatially periodic configuration. In contrast, the vortices in an exotic wake typically exhibit significant relative motion, which breaks the spatial periodicity. However, in order to keep the model mathematically tractable, it is assumed that the influence of any vortices upstream or downstream of a given cluster of N vortices can be approximated as being due to the spatially periodic images of those N vortices. That is, the assumption is that the periodically forced wakes in Fig. 1.2 can be modeled by the temporal evolution of N point vortices in a spatially periodic domain.

The finite vortex wake is modeled as an infinite, spatially periodic arrangement of point vortices. In each periodic strip of width L, there are N base vortices. The position of the base vortex α is given by $z_\alpha = x_\alpha + \mathrm{i}\, y_\alpha$ and its circulation is represented by Γ_α. The Γ_α remain constant in this mathematical framework, so clearly the sum of the vortex strengths,

$$S_1 = \sum_{\alpha=1}^{N} \Gamma_\alpha, \tag{1.2}$$

is a constant of the motion. Since the discussion is motivated by periodic shedding from a bluff body, we assume that $S_1 = 0$ in every case considered here.

The base arrangement has an infinite number of periodic images on either side located at $z_\alpha \pm nL$, where $n \in I$. Substitution of this representation into the point vortex equations leads to

$$\frac{\mathrm{d}z_\alpha^*}{\mathrm{d}t} = \frac{1}{2\pi \mathrm{i}} \sum_{\beta=1}^{4}{}' \left\{ \frac{\Gamma_\beta}{z_\alpha - z_\beta} + \sum_{n=1}^{\infty} \left[\frac{\Gamma_\beta}{z_\alpha - (z_\beta + nL)} + \frac{\Gamma_\beta}{z_\alpha - (z_\beta - nL)} \right] \right\}, \tag{1.3a}$$

where the asterisk on the left hand side signifies complex conjugation and the prime over the summation implies the exclusion of the $\alpha = \beta$ term. The summation is done pairwise, adding the contributions from images on the left, $z_\beta - nL$, and the right, $z_\beta + nL$, spaced at equal distances from the "base vortex" at the location z_β. Such a prescription renders the sum to be convergent (sums of this kind, which are made convergent by specifying a distinct order in which to add are described as *conditionally convergent*).

The resulting sum can, hence, be transcribed as follows,

$$\frac{\mathrm{d}z_\alpha^*}{\mathrm{d}t} = \frac{1}{2\pi \mathrm{i}} \sum_{\beta=1}^{N}{}' \Gamma_\beta \left[\frac{1}{z_\alpha - z_\beta} + 2 \sum_{n=1}^{\infty} \frac{z_\alpha - z_\beta}{(z_\alpha - z_\beta)^2 - (nL)^2} \right]. \tag{1.3b}$$

Within the square brackets, the function can be simplified in the following form,

$$\frac{1}{z} + 2 \sum_{n=1}^{\infty} \frac{z}{z^2 - (nL)^2} = \frac{\pi}{L} \left[\frac{L}{\pi z} + 2 \sum_{n=1}^{\infty} \frac{\pi z / L}{(\pi z/L)^2 - (n\pi)^2} \right] = \frac{\pi}{L} \cot \left(\frac{\pi z}{L} \right). \tag{1.4a}$$

The above derivation uses the *partial fraction decomposition* of cot, which is

$$\frac{1}{z} + 2z \sum_{n=1}^{\infty} \frac{1}{z^2 - (n\pi)^2} = \cot z. \tag{1.4b}$$

Thus, from equation (1.3b),

$$\frac{\mathrm{d}z_\alpha^*}{\mathrm{d}t} = \frac{1}{2L\mathrm{i}} \sum_{\beta=1}^{N}{}' \Gamma_\beta \cot \left[\frac{\pi}{L} (z_\alpha - z_\beta) \right]. \tag{1.5}$$

These represent the equations of motion for N vortices in a periodic strip of width L, or equivalently for N vortex rows with the spacing between the identical vortices in each row being L. Thus, here the point vortex motion is considered in a frame of reference that moves along with the background flow (implying $U = 0$). These equations have been developed previously in [20, 21].

The equations (1.3b) share properties with equations of motion on the infinite plane. This periodic system of N vortices in a single period can be cast in the Hamiltonian form, with the Hamiltonian being given by

$$H(z_1, z_2, z_3, ..., z_N) = -\frac{1}{4\pi} \sum_{\alpha,\beta=1}^{N}{}' \Gamma_\alpha \Gamma_\beta \; \ln \left| \sin \left[\frac{\pi}{L} (z_\alpha - z_\beta) \right] \right| . \tag{1.6}$$

The Hamiltonian represents a constant of motion. The corresponding canonical equations are in the form, first demonstrated in [22],

$$\Gamma_\alpha \frac{\mathrm{d}x_\alpha}{\mathrm{d}t} = \frac{\partial H}{\partial y_\alpha}, \qquad \Gamma_\alpha \frac{\mathrm{d}y_\alpha}{\mathrm{d}t} = -\frac{\partial H}{\partial x_\alpha}. \tag{1.7}$$

Two other common integrals on the infinite plane are the components of the linear impulse, $\mathcal{Q}$ and $\mathcal{P}$,

$$\mathcal{Q} + \mathrm{i}\mathcal{P} = \sum_{\alpha=1}^{N} \Gamma_\alpha \, z_\alpha . \tag{1.8}$$

These remain integrals for the periodic strip system as well [23]. The invariance in the transverse y-direction is comprehensible as the motion occurs in the streamwise direction (i.e. in the x-direction). As for the invariance to translation in the x-direction, each x_α appearing in $\mathcal{Q}$ is only defined modulo the strip width L, i.e. if a vortex "leaves" the base strip at $x = L$, it "reappears" at $x = 0$. Therefore, while verifying the invariance of the $\mathcal{Q}$ component of the linear impulse; just consideration of the instantaneous configuration of the vortices in the base strop is not sufficient and how often each vortex has gone through the strip becomes an important parameter. It should also be noted here that for point vortex motion on the unbounded plane, the angular impulse is also a constant of the motion, but it is not conserved for this periodic system.

Finally, before proceeding to the details of the mathematical modeling work for the few-vortex problems (in the periodic domain), it is worthwhile to note that the flow field produced at $z = x + \mathrm{i}y$ by a periodic row of vortices (having N vortices in each periodic domain) is obtained as follows, by the generalization of equation (1.5),

$$u - \mathrm{i}v = \frac{1}{2L\mathrm{i}} \sum_{\alpha=1}^{N} \Gamma_\alpha \cot\left[\frac{\pi}{L}(z - z_\alpha)\right]. \tag{1.9}$$

Subsequent chapters deal with variants of the discussed general configuration by putting $N = 4$ and $N = 3$ respectively (with N, as has been defined, being the number of vortices in each periodic strip).

Chapter 2

Mathematical model for symmetric four vortex wakes

2.1 Equations of motion

From the developments in §1.2.1, the Hamiltonian formalism for four point vortices contained in a periodic domain can be transcribed as (following equation (1.6))

$$H(z_1, z_2, z_2, z_4) = -\frac{1}{4\pi} {\sum_{\alpha,\beta=1}^{4}}' \Gamma_\alpha \Gamma_\beta \;\ln \left| \sin \left[\frac{\pi}{L} \left(z_\alpha - z_\beta \right) \right] \right| . \tag{2.1}$$

Following the previous discussions, the canonical equations governing the motion of each point vortex in this periodic setup are again given by

$$\Gamma_\alpha \frac{\mathrm{d}x_\alpha}{\mathrm{d}t} = \frac{\partial H}{\partial y_\alpha}, \qquad \Gamma_\alpha \frac{\mathrm{d}y_\alpha}{\mathrm{d}t} = -\frac{\partial H}{\partial x_\alpha}, \tag{2.2}$$

and the two conserved linear impulse components, $\mathcal{Q}$ and $\mathcal{P}$, are defined by

$$\mathcal{Q} + \mathrm{i}\mathcal{P} = \sum_{\alpha=1}^{4} \Gamma_\alpha \, z_\alpha. \tag{2.3}$$

The linear impulse is conserved owing to the fact that this Hamiltonian system is invariant to shifts in the location of the origin, and we thus are able to analyze our problems of interest in terms of the dimensionless vortex separation

$$Z = X + \mathrm{i}\, Y = \pi(z_1 - z_2)/L. \tag{2.4}$$

It is noted that even on the unbounded plane [24], there are not sufficient constants of motion for the four-vortex system to be integrable. Hence, so as to render the system mathematically tractable, imposition of a new set of constraints on the point vortex setup becomes essential.

2.1.1 Modeling approach

Based on the experimentally observed wake arrangements with two pairs of vortices placed symmetrically about the streamwise direction (see Fig. 2.1(a)), the following are assumed in regards to the vortex circulations and positions,

$$\Gamma_3 = -\Gamma_1, \quad z_3 = z_1^* \equiv \zeta_1, \tag{2.5a}$$

$$\Gamma_4 = -\Gamma_2, \quad z_4 = z_2^* \equiv \zeta_2, \tag{2.5b}$$

where the asterisk denotes complex conjugation. Thus, the two vortex pairs shed into the flow in each oscillation cycle of the corresponding bluff body are assumed to represent the mirror images of each other and the net sum of the vortex circulations within the periodic

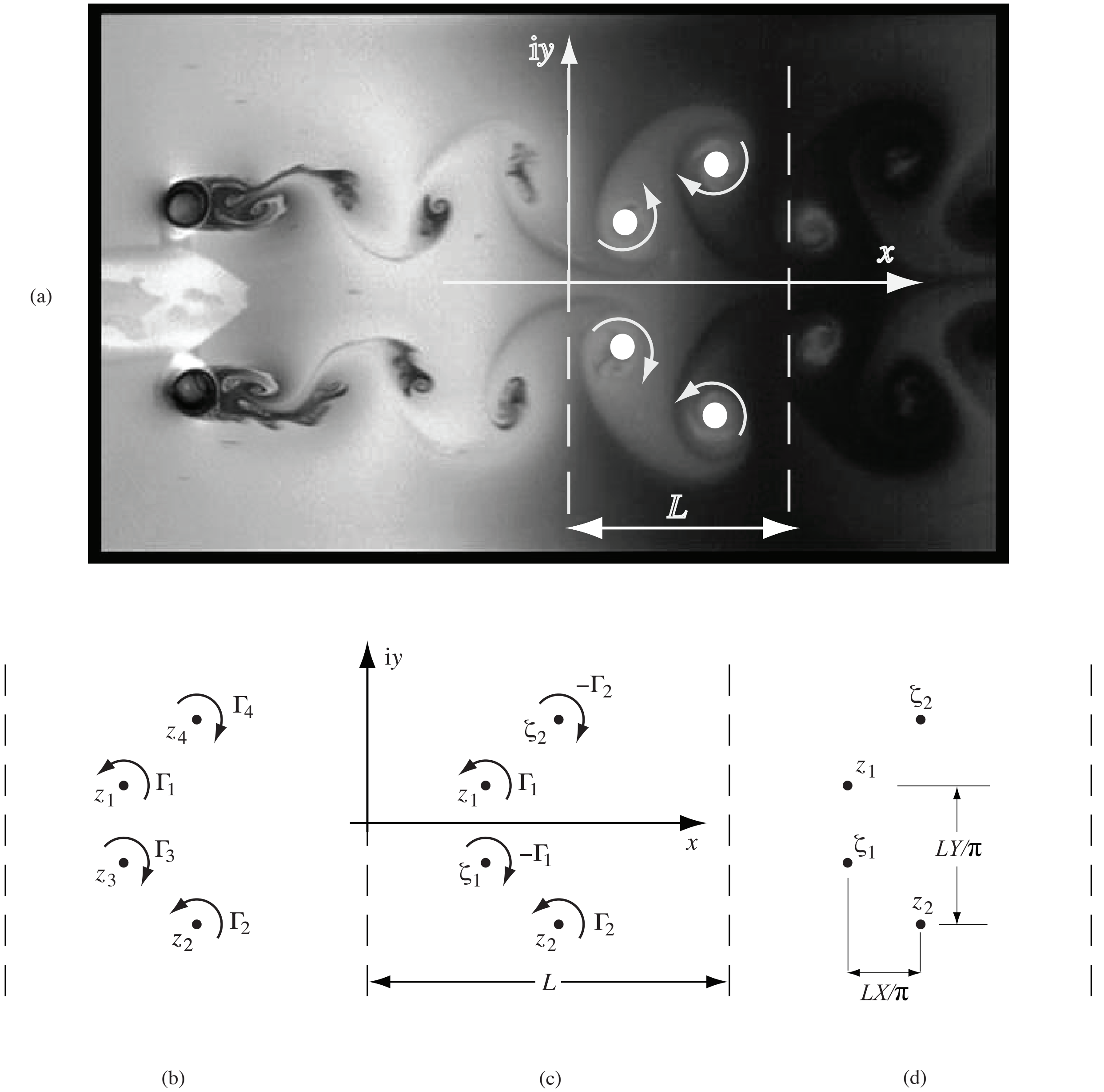

Figure 2.1: (a) Four vortex symmetric wake as observed in experiments [4]. The assumed spatial arrangement of the model vortices, along with the rotational features, are marked in white. (b) The general symmetric four vortex setup. (c) Model vortex locations with the assumed spatial symmetry. (d) Periodic setup showing the separation parameters between the two positively-signed (rotating counter-clockwise) vortices.

strip system is zero. The panels (c) and (d) in Fig. 2.1 illustrate the introduced spatial assumptions.

The following quantities are also defined,

$$\mathbb{S} = \Gamma_1 + \Gamma_2, \qquad \gamma = \Gamma_1/\mathbb{S}, \tag{2.6}$$

so as to explicitly identify the different vortex ratio values. These notations have been used consistently henceforth in the subsequent sections and chapters.

The constraints (2.5) make it possible to reduce the model problem to a two degree-of-freedom Hamiltonian system. Using (2.3), the components of the linear impulse are calculated as follows:

$$\mathcal{Q} = d(\Gamma_1 - \Gamma_2), \qquad \mathcal{P} = 2\left(\Gamma_1 y_1 + \Gamma_2 y_2\right). \tag{2.7a}$$

Non-dimensionalized forms of the horizontal and vertical components of the linear impulse are respectively

$$\mathbb{Q} = \mathcal{Q}/L\mathbb{S} = d\left(2\gamma - 1\right)/L, \qquad \mathbb{P} = \mathcal{P}/L\mathbb{S} = 2\left[\gamma y_1 + \left(1-\gamma\right) y_2\right]/L. \tag{2.7b}$$

Coupling these with $z_1 - z_2 = \Delta x + \mathrm{i}\,\Delta y$, it is possible to express

$$y_1 = \frac{\mathbb{P}L}{2} + \left(1-\gamma\right)\Delta y, \qquad y_2 = \frac{\mathbb{P}L}{2} - \gamma\Delta y. \tag{2.8}$$

It is additionally possible to non-dimensionalize the Hamiltonian, defined in equation (2.1), to the following form,

$$\mathbb{H} = \frac{H}{\mathbb{S}^2\gamma\left(1-\gamma\right)}. \tag{2.9}$$

With proper substitutions from equations (2.4), (2.7), and (2.8) in equation (2.1), and using the non-dimensionalized formalism defined in equation (2.9), the Hamiltonian for the four vortex symmetric wake arrangement can be reduced to,

$$\begin{aligned}\mathbb{H}(Z;\gamma,\mathbb{P}) = -\frac{1}{2\pi}\Bigg[\ln\left|\frac{\sin^2 X + \sinh^2 Y}{\cos^2 X - \cosh^2\big[\pi\mathbb{P} + (1-2\gamma)Y)\big]}\right| \\ - \frac{\gamma}{2\,(1-\gamma)}\ln\big|\big[1-\cosh^2\big[\pi\mathbb{P}+2\,(1-\gamma)Y)\big]\big| - \frac{1-\gamma}{2\,\gamma}\ln\big|\big[1-\cosh^2\big[\pi\mathbb{P}-2\gamma Y\big]\big|\Bigg].\end{aligned} \tag{2.10}$$

This reduced Hamiltonian satisfies the following canonical equations of motion,

$$\frac{2}{\mathbb{S}}\frac{\mathrm{d}(\Delta x)}{\mathrm{d}t} = \frac{\partial\mathbb{H}}{\partial(\Delta y)} \tag{2.11a}$$

$$\frac{2}{\mathbb{S}}\frac{\mathrm{d}(\Delta y)}{\mathrm{d}t} = -\frac{\partial\mathbb{H}}{\partial(\Delta x)}. \tag{2.11b}$$

Introducing the dimensionless time variable

$$\tau = \left(\pi^2\mathbb{S}\right)t/2L^2, \tag{2.12}$$

the equations (2.11) can be simplified to the following form,

$$\frac{\mathrm{d}X}{\mathrm{d}\tau} = \frac{\partial\mathbb{H}}{\partial Y}, \qquad \frac{\mathrm{d}Y}{\mathrm{d}\tau} = -\frac{\partial\mathbb{H}}{\partial X}. \tag{2.13}$$

2.2 Phase plane representation

The dynamics of the model vortices can now be characterized by considering the (X, Y) evolution along the level curves of the Hamiltonian drawn on the (X, Y)-phase plane (Z-plane). Fig. 2.2 lays out the evolution of the phase space as the constant of motion $\mathbb{P}$ is

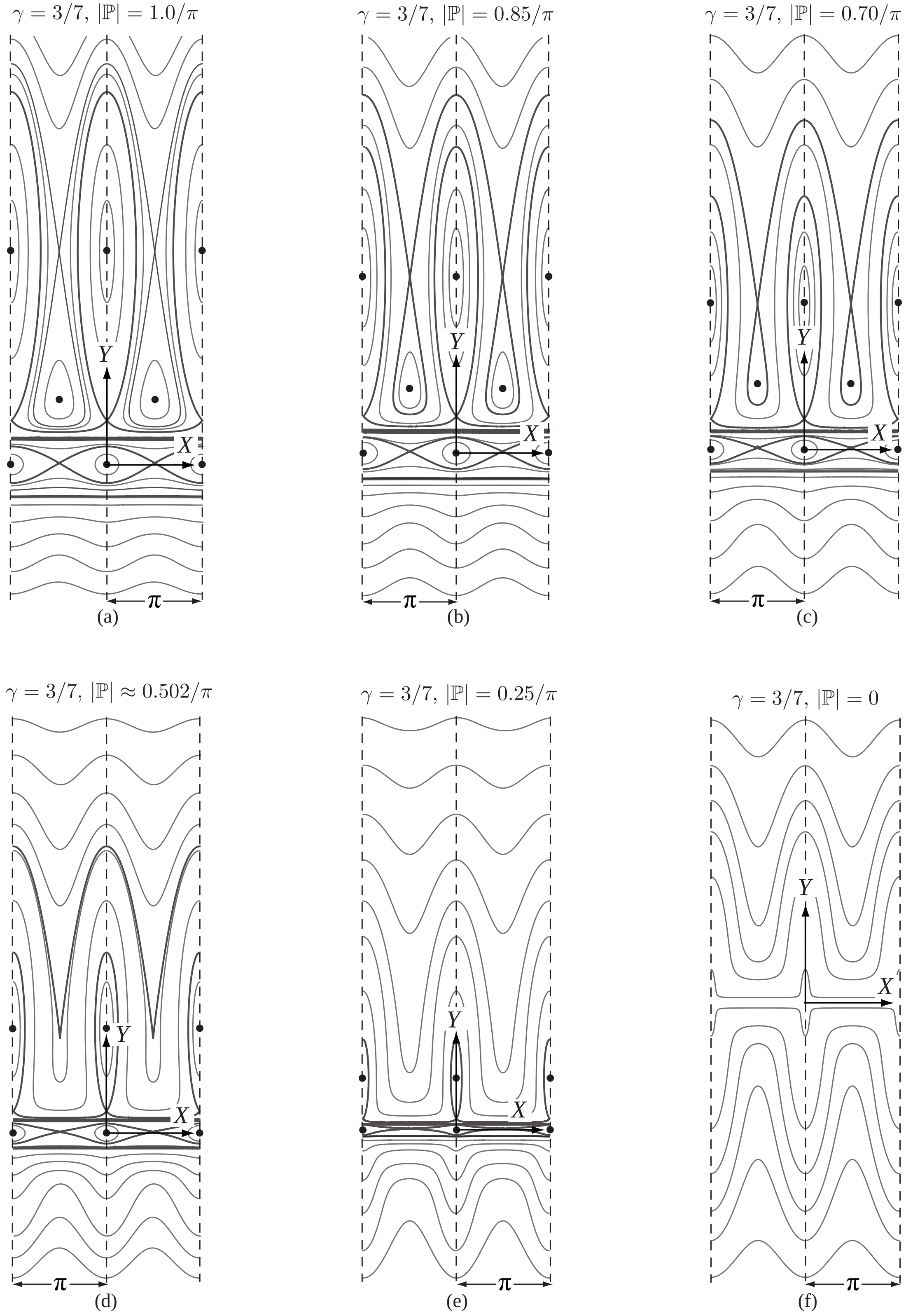

(a) (b) (c)

(d) (e) (f)

Figure 2.2: Representative phase space topology for symmetric four-vortex wakes. Panel (d) involves a bifurcation owing to the connection between the (unstable) fixed points.

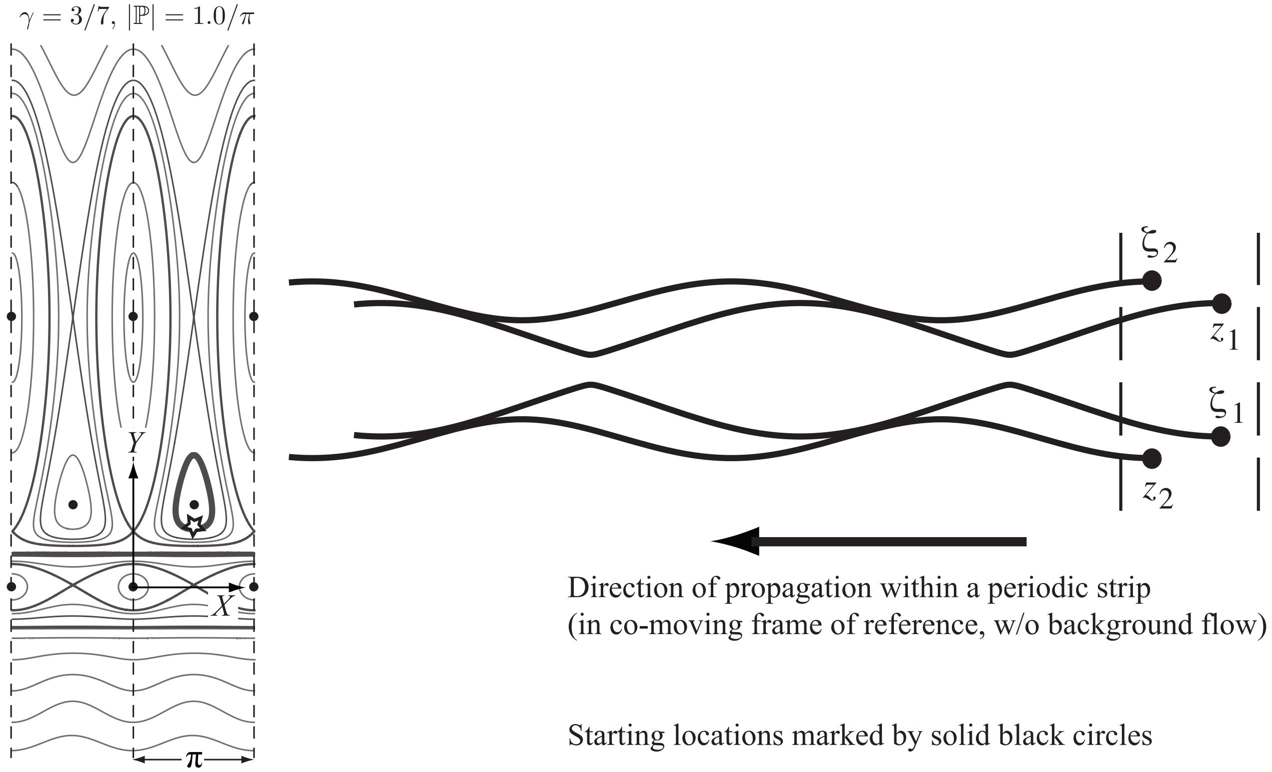

Figure 2.3: (a) Phase plane diagram on the Z plane. Real space trajectories of the vortices are obtained by integrating along the level curves of Hamiltonian. The tracked level curve has been marked by a star. (b) Trajectories of the vortices in the physical space. Based on the topology of the chosen level curve (which, in turn, dictates the variation of the relative displacement parameters X, Y between the positive vortex locations z_1 and z_2); the corresponding real space motion of the vortices can show distinct features. More details of these relative vortex motions and their characterization follow in Chapter 3.

gradually varied for the selected case when $\gamma = 3/7$ (or, $\Gamma_1/\Gamma_2 = 3/4$). The phase spaces illustrate a unique feature in the form of a constrained region of phase topology adhering to the horizontal axis and marked by two horizontal bands of level curves on either side of it. These regions correspond to the singularity which arises when the energy of the system approaches ∞. This occurs as the vertical separation $|Y|$ reduces and two vortices (counterpart vortices from each individual pair from either side of the wake centerline) try to cross over each other. It is interesting to note here that such a situation cannot arise in the staggered configuration owing to the horizontal separation between the vortex pairs (for

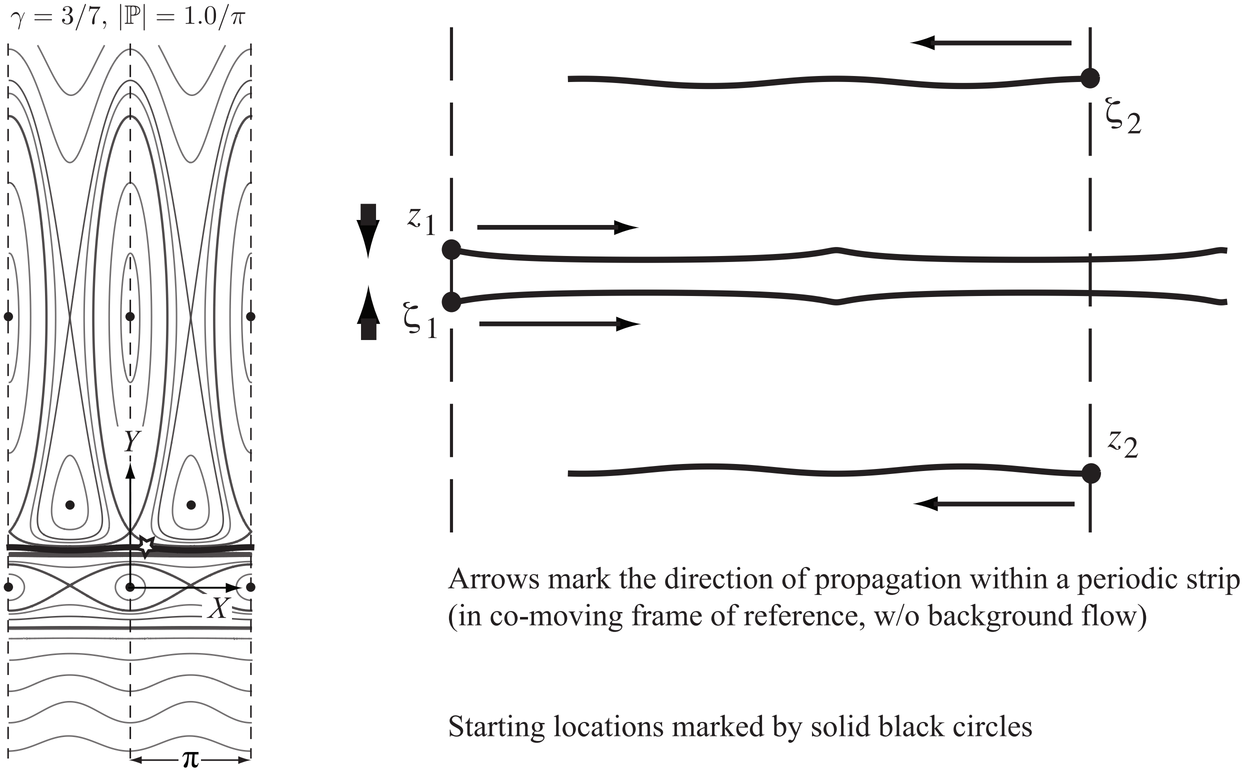

Figure 2.4: ((a) Phase plane diagram on the Z plane. Real space trajectories of the vortices are obtained by integrating along the level curves of Hamiltonian. The tracked level curve has been marked by a star. (b) Trajectories of the vortices in the physical space. Based on the topology of the chosen level curve (which, in turn, dictates the variation of the relative displacement parameters X, Y between the positive vortex locations z_1 and z_2); the corresponding real space motion of the vortices can show distinct features. More details of these relative vortex motions and their characterization follow in Chapter 3.

details, see Chapter 3).

At the limiting case when the vertical component of the linear impulse of the system vanishes i.e. when $\mathbb{P} = 0$, there are some added complexities which are discussed henceforth. For the following calculations, it should be recalled that the coordinates (x_1, y_1) and (x_2, y_2) respectively denote the positive base vortex locations z_1 and z_2. Using (2.7b) and making the right hand side to be equal to zero, the following is obtained,

$$\frac{y_1}{y_2} = -\frac{\Gamma_2}{\Gamma_1} = -\frac{1-\gamma}{\gamma} \tag{2.14}$$

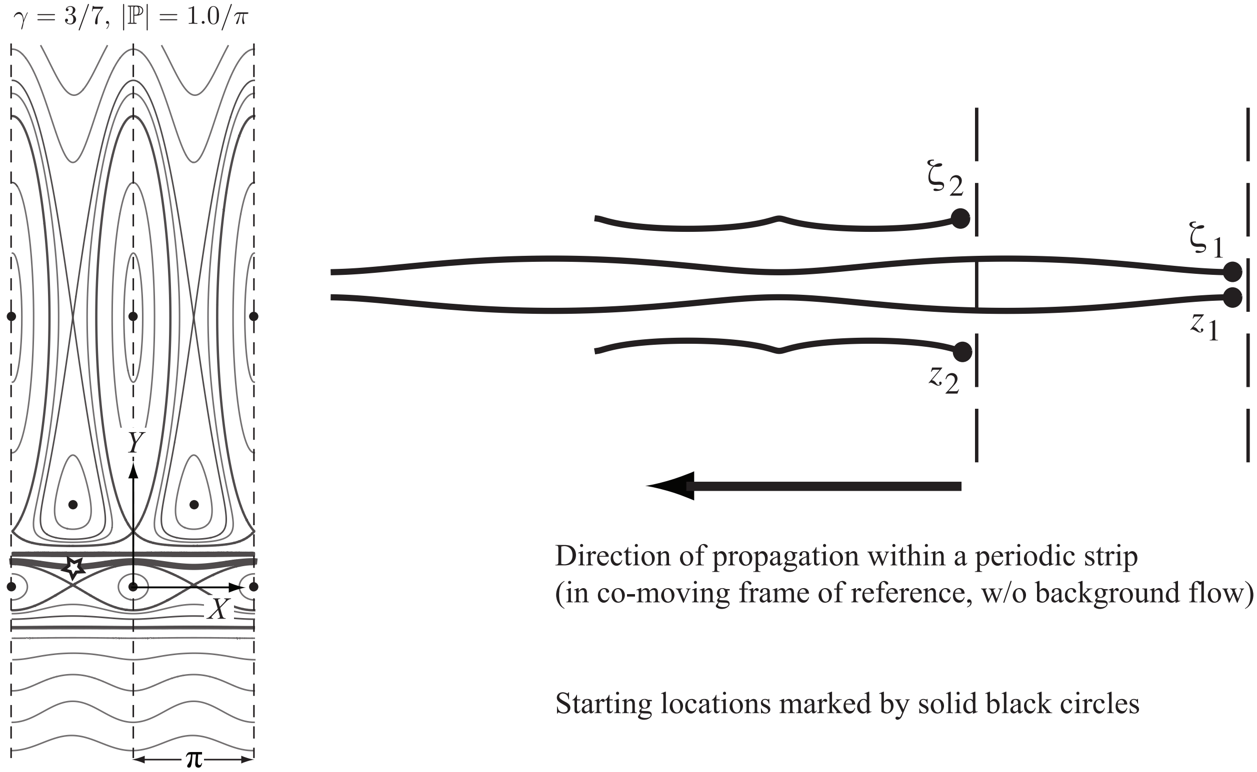

Figure 2.5: (a) Phase plane diagram on the Z plane. Real space trajectories of the vortices are obtained by integrating along the level curves of Hamiltonian. The tracked level curve has been marked by a star. (b) Trajectories of the vortices in the physical space. Based on the topology of the chosen level curve (which, in turn, dictates the variation of the relative displacement parameters X, Y between the positive vortex locations z_1 and z_2); the corresponding real space motion of the vortices can show distinct features. More details of these relative vortex motions and their characterization follow in Chapter 3.

Coupling this up with $y_1 - y_2 = \Delta y$, it is straight-forward to show that.

$$y_1 = (1 - \gamma)\,\Delta y, \qquad y_2 = -\gamma\,\Delta y. \tag{2.15}$$

For the represented case where $\gamma = 3/7$. these simplify to $y_1 = \frac{4}{7}\,\Delta y$ and $y_2 = -\frac{3}{7}\,\Delta y$. This implies that when $|\Delta y| \to 0$ (i.e. $|Y| = |\pi \Delta y / L| \to 0$), the system has $y_1 \approx y_2$. This signifies a merging together of the vortex locations thereby giving rise to a special singularity where both the vortices from the individual pairs approach their counterparts in the other pair.

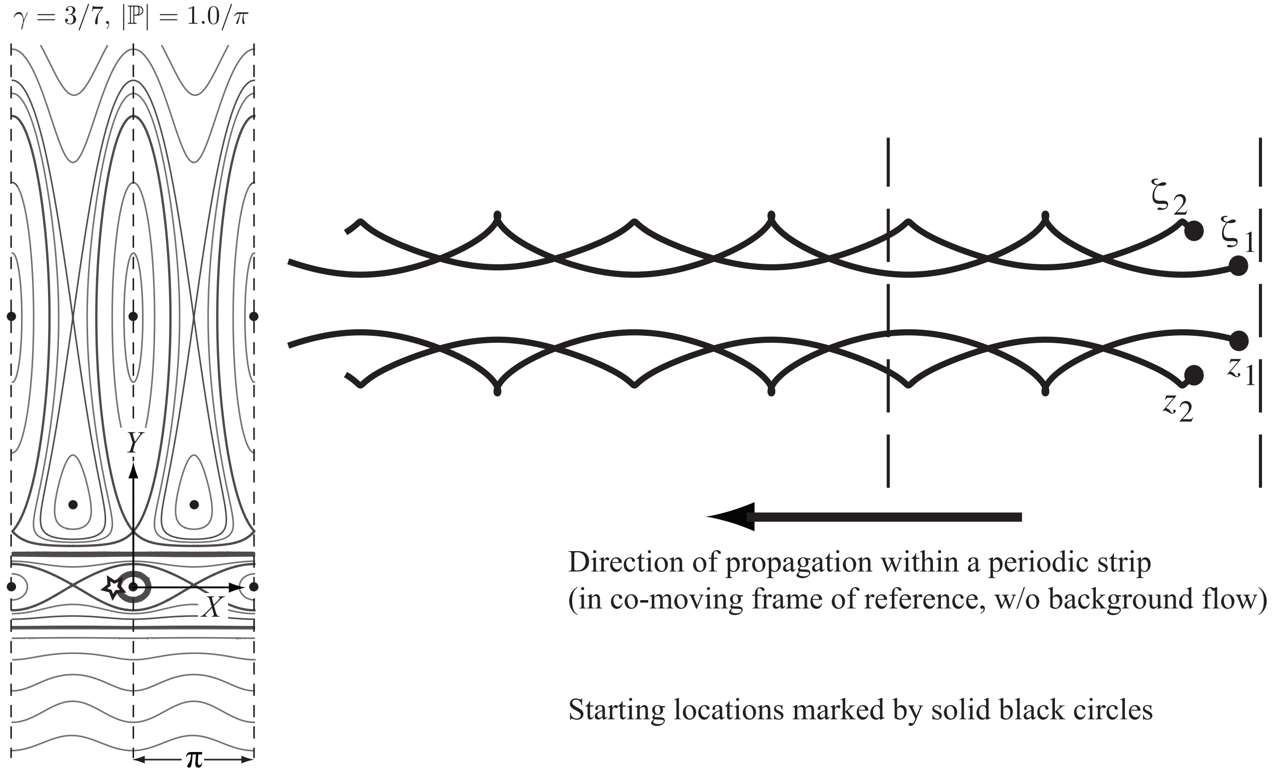

Figure 2.6: (a) Phase plane diagram on the Z plane. Real space trajectories of the vortices are obtained by integrating along the level curves of Hamiltonian. The tracked level curve has been marked by a star. (b) Trajectories of the vortices in the physical space. Based on the topology of the chosen level curve (which, in turn, dictates the variation of the relative displacement parameters X, Y between the positive vortex locations z_1 and z_2); the corresponding real space motion of the vortices can show distinct features. More details of these relative vortex motions and their characterization follow in Chapter 3.

2.3 Physical trajectories of the point vortices

The real space trajectories of the point vortices in a co-moving frame of reference can be derived for given values of γ and $\mathbb{P}$ through numerical integration of equation (2.1), subject to the imposed constraints (2.5). The Hamiltonian being a constant of motion; the relative vortex motion always occurs along a specific Hamiltonian level curve. This implies that the relative separation (X, Y) values in a vortex arrangement will vary in such a way (as the vortex setup progresses downstream) that the Hamiltonian formalism, which is a function of

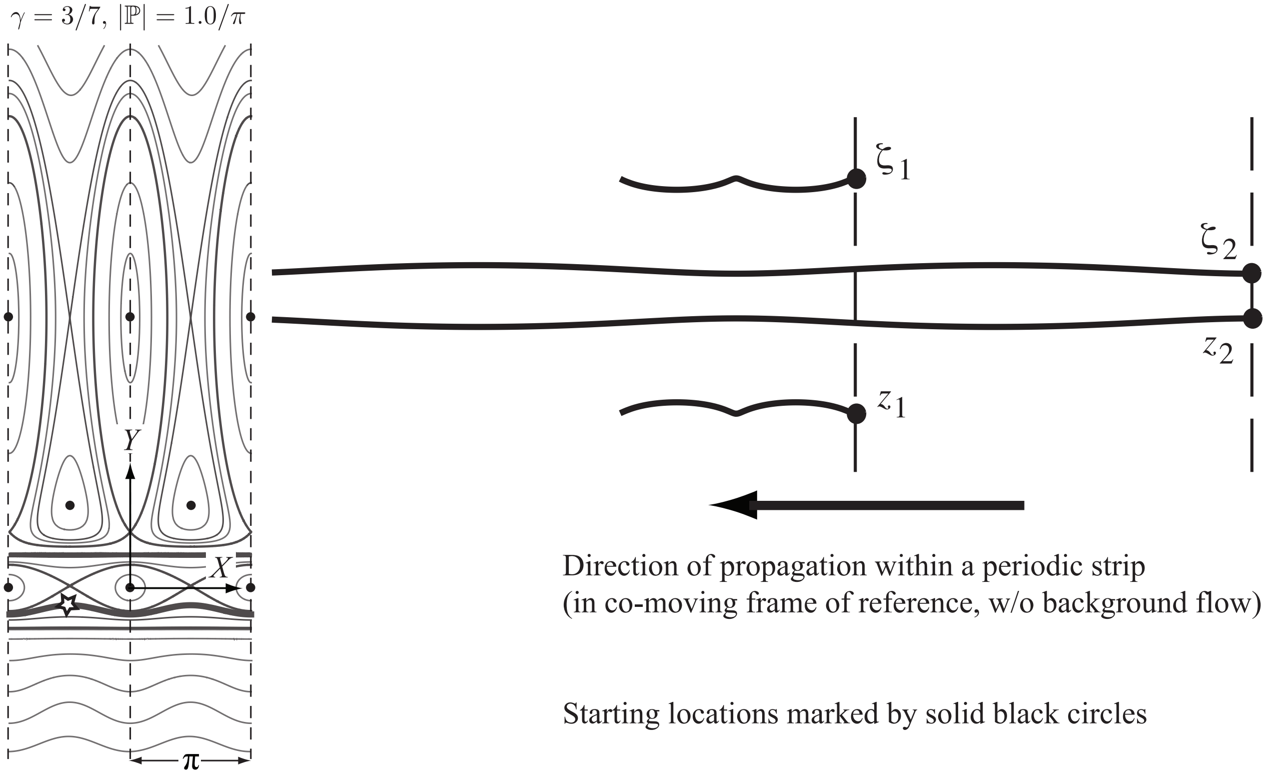

Direction of propagation within a periodic strip
(in co-moving frame of reference, w/o background flow)

Starting locations marked by solid black circles

Figure 2.7: (a) Phase plane diagram on the Z plane. Real space trajectories of the vortices are obtained by integrating along the level curves of Hamiltonian. The tracked level curve has been marked by a star. (b) Trajectories of the vortices in the physical space. Based on the topology of the chosen level curve (which, in turn, dictates the variation of the relative displacement parameters X, Y between the positive vortex locations z_1 and z_2); the corresponding real space motion of the vortices can show distinct features. More details of these relative vortex motions and their characterization follow in Chapter 3.

X and Y, stays conserved. Thus, by tracking the different topologies of Hamiltonian level curves on the phase domain, various distinct types of relative vortex motion are identifiable.

The detailed characterization of all the different sub-modes of relative vortex motion, based on phase space analysis, will be discussed for the more general orientation of staggered vortex pairs in Chapter 3. As for the symmetric configuration, this section presents some representative and interesting examples of relative vortex dynamics.

Fig. 2.3 depicts a type of *orbiting* mode, where the motion is tracked along an orbital level

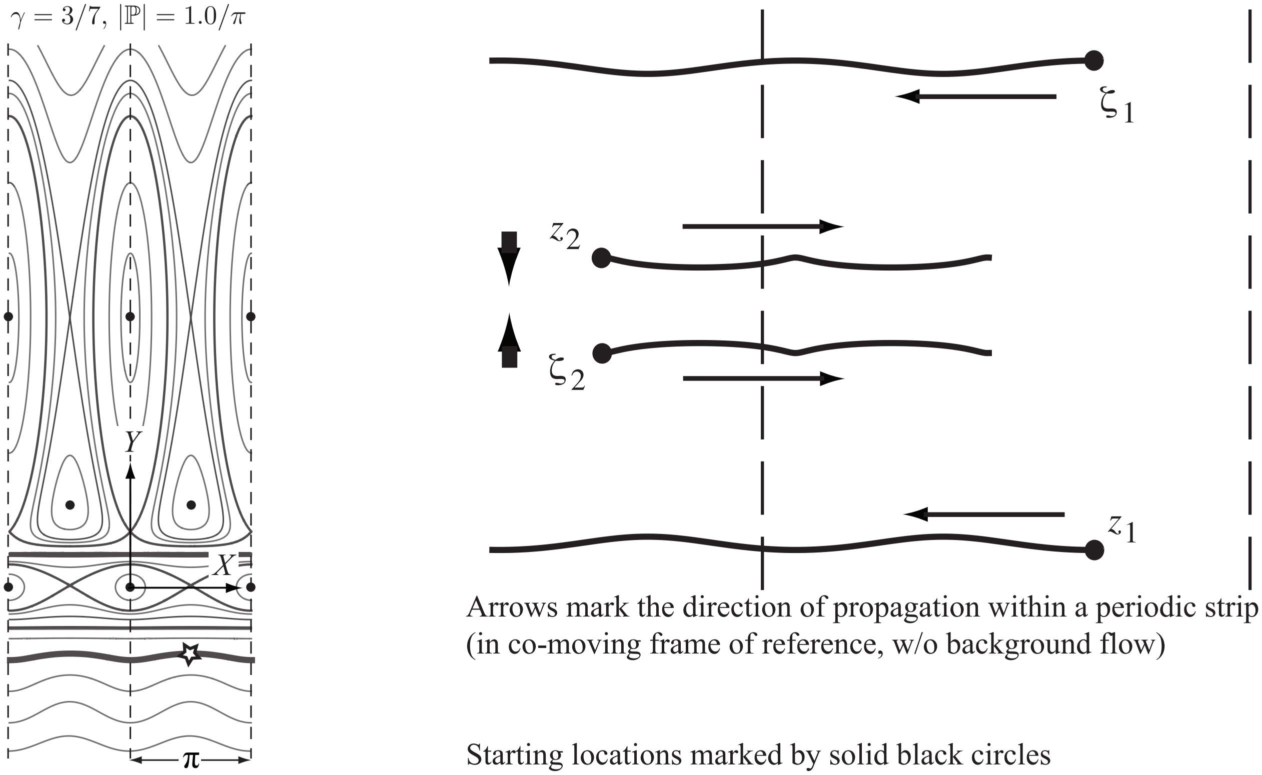

Arrows mark the direction of propagation within a periodic strip (in co-moving frame of reference, w/o background flow)

Starting locations marked by solid black circles

Figure 2.8: (a) Phase plane diagram on the Z plane. Real space trajectories of the vortices are obtained by integrating along the level curves of Hamiltonian. The tracked level curve has been marked by a star. (b) Trajectories of the vortices in the physical space. Based on the topology of the chosen level curve (which, in turn, dictates the variation of the relative displacement parameters X, Y between the positive vortex locations z_1 and z_2); the corresponding real space motion of the vortices can show distinct features. More details of these relative vortex motions and their characterization follow in Chapter 3.

curve of the Hamiltonian (marked in Fig. 2.3(a)). In this this particular example, the vortex trajectories approach each other and then subsequently move away periodically. Based on the selected parameters γ and $\mathbb{P}$, the vortex trajectories can also wrap and orbit around each other (typical examples have been discussed in Chapter 3) and this justifies the nomenclature.

Fig. 2.4 represents the vortex configuration just before hitting the singular region when two of the vortices tend to cross over each other. Here, the vortices at locations z_1 and ζ_1 are of opposite rotations (the one at z_1 being positive and counter-clockwise, and the one at ζ_1 being negative and clockwuse) and hence when they are very close to each other they shoot off in the opposite direction to the two outer vortices in the periodic domain. Subsequently, when the singular cross-over region has been circumvented, the trajectories for all the four vortices progress in the same direction (see Fig. 2.5). A similar phenomenon occurs in Fig. 2.6 and Fig. 2.7. The real space motion shown in Fig. 2.5 belongs to another sub-type of *orbiting* motion where the vortex trajectories orbit around each other as they propagate downstream. The contents of this chapter can be sourced back to [25] and [26].

Chapter 3

Mathematical model for staggered four vortex wakes

3.1 Equations of motion

Focus of this chapter is on the mathematical modeling of 2P regime wake arrangements with the two vortex pairs in each shedding cycle being placed in a staggered orientation with respect to the central streamwise axis (for examples, see Figs. 1.2(b) and 4.1).

The finite vortex wake is modeled as an infinite, spatially periodic arrangement of point vortices. In each periodic strip of width L, there are $N = 4$ base vortices. As in §1.2.1, which has introduced the mathematical framework for the model, the position of the base vortex α is represented as $z_\alpha = x_\alpha + \mathrm{i}\, y_\alpha$ and the circulation is Γ_α.

Following the developments of §1.2.1 and §2.1, the equations of motion of the point vortices in the periodic domain can again be written in the form,

$$\frac{\mathrm{d}z_\alpha^*}{\mathrm{d}t} = \frac{1}{2L\mathrm{i}} \sum_{\beta=1}^{4}{}' \, \Gamma_\beta \cot\left[\frac{\pi}{L}(z_\alpha - z_\beta)\right]. \tag{3.1}$$

This represents a Hamiltonian system, with the Hamiltonian being given by

$$H(z_1, z_2, z_2, z_4) = -\frac{1}{4\pi} \sum_{\alpha,\beta=1}^{4}{}' \, \Gamma_\alpha \Gamma_\beta \, \ln \left| \sin \left[\frac{\pi}{L} \left(z_\alpha - z_\beta \right) \right] \right| . \tag{3.2}$$

The general Hamiltonian formalism for the staggered arrangement remains same as that for the symmetric setup and hence does not have any special geometry correspondence.

As before the conserved Hamiltonian satisfies the following canonical equations [22],

$$\Gamma_\alpha \frac{\mathrm{d}x_\alpha}{\mathrm{d}t} = \frac{\partial H}{\partial y_\alpha}, \qquad \Gamma_\alpha \frac{\mathrm{d}y_\alpha}{\mathrm{d}t} = -\frac{\partial H}{\partial x_\alpha}. \tag{3.3}$$

The linear impulse, another constant of motion, is also given by

$$\mathcal{Q} + \mathrm{i}\mathcal{P} = \sum_{\alpha=1}^{4} \Gamma_\alpha \, z_\alpha . \tag{3.4}$$

Following similar strategies as in §2.1.1, a discrete spatial symmetry is imposed on this point vortex system in order to make it mathematically tractable. Based on the experimental wake patterns (see Fig. 4.1), the following are assumed regarding the vortex circulations and positions,

$$\Gamma_3 = -\Gamma_1, \quad z_3 = z_1^* - d \equiv \zeta_1, \tag{3.5a}$$

$$\Gamma_4 = -\Gamma_2, \quad z_4 = z_2^* + d \equiv \zeta_2, \tag{3.5b}$$

where the asterisk again denotes complex conjugation and d is a real-valued constant. Therefore, it is assumed that the two vortex pairs that are shed by the body during a single cycle are mirror images of each other about the wake centerline, but are separated by a horizontal offset d that is independent of the vortex motion. The central and right panels of Fig. **??**

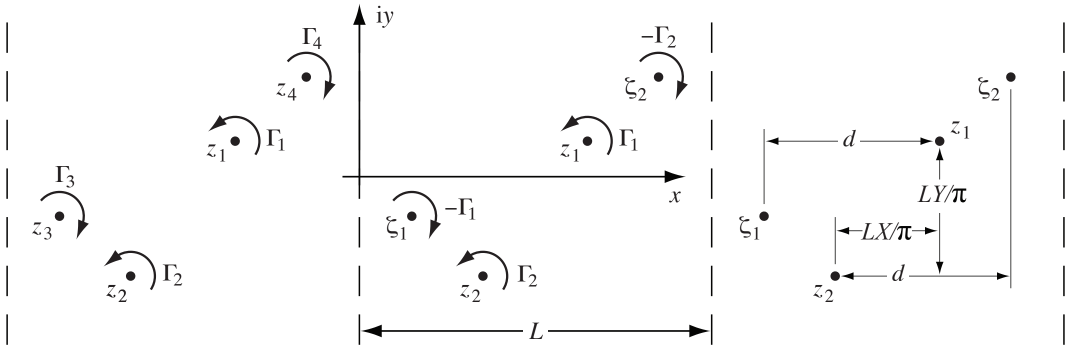

Figure 3.1: Model representation of a staggered vortex street configuration with four vortices per period.

portray these spatial assumptions. The generalization $\Gamma_1 \neq \Gamma_2$ makes the system resemble the real wakes more closely. The imposed spatial constraints imply that $\mathrm{d}\zeta_\alpha/\mathrm{d}t = \mathrm{d}z_\alpha^*/\mathrm{d}t$, whereby equations (3.1) make it necessary that

$$d = nL/2, \quad n \in I. \tag{3.6}$$

Here the focus is on the case of staggered vortex pairs and hence it is assumed that $n = 1$.

3.1.1 General case

The general case considers arbitrary γ, which is a measure of the positive vortex circulation ratio (for definition of γ, see equation (2.6)). Using equations (2.6), (2.7), (2.8), (2.9); in conjunction with (3.5) and (3.6), it is possible to reduce the general four vortex Hamiltonian formalism (see equation (3.2)) to the form here-under,

$$\begin{aligned}\mathbb{H}(Z;\gamma,\mathbb{P}) = -\frac{1}{2\pi}\Bigg\{ &\ln\left[\frac{\sin^2 X + \sinh^2 Y}{\cos^2 X + \sinh^2\left[\pi\mathbb{P} + (1-2\gamma)\, Y\right]}\right] \\ &- \frac{\gamma}{1-\gamma}\ln\Big[\cosh\left[\pi\mathbb{P} + 2\,(1-\gamma)\, Y\right]\Big] - \frac{1-\gamma}{\gamma}\ln\Big[\cosh\left[\pi\mathbb{P} - 2\gamma Y\right]\Big]\Bigg\}. \end{aligned}\tag{3.7}$$

The reduced Hamiltonian satisfies the following canonical equations (the structure being same as in equation (2.13)) relating the time evolution of the relative separation between the positive base vortices,

$$\frac{\mathrm{d}X}{\mathrm{d}\tau} = \frac{\partial \mathbb{H}}{\partial Y}, \qquad \frac{\mathrm{d}Y}{\mathrm{d}\tau} = -\frac{\partial \mathbb{H}}{\partial X}, \tag{3.8a}$$

with the non-dimensional time being same as that introduced in equation (2.12), i.e. $\tau = (\pi^2 \mathbb{S})\, t/2L^2$.

The constrained system is hence integrable, and the dynamics can be characterized by considering motion along the level curves of $\mathbb{H}$ in the (X, Y) phase space. Subsequently, the individual vortex trajectories in the physical domain are obtained by integrating along the level curves using numerical quadrature.

3.1.2 Special case: Vortex strengths of equal magnitude

Consider $\Gamma_1 = \Gamma_2$ i.e. all the vortex strengths are of equal magnitude. This formation is popularly known as the *Domm system* [27], [28]. Here, equation (2.6) gives $\gamma = 1/2$. Under this consideration, the non-dimensionalized components of the linear impulse transform to

$$\mathbb{Q} = 0, \qquad \mathbb{P} = (y_1 + y_2)/L, \tag{3.9}$$

and the Hamiltonian derived in (3.7) can be further simplified to

$$\mathbb{H}(\Delta x, \Delta y) = -\frac{1}{2\pi} \ln \left\{ \frac{\sin^2 X + \sinh^2 Y}{\left(\cos^2 X + \sinh^2 [\pi\, \mathbb{P}]\right) \left(\cosh^2 Y + \sinh^2 [\pi\, \mathbb{P}]\right)} \right\}. \tag{3.10}$$

The equation (3.10) has been presented in an alternate form in [29] and is hence a special case of the generalized form (3.7) discussed here.

3.2 Model characterization and results

3.2.1 Bifurcations in the phase space topology

The reduced form of the Hamiltonian from equation (3.7) enables the transformation of the problem to a two degree-of-freedom system in terms of the separation variables between the positive base vortices (locations z_1 and z_2 on Fig. 3.1). The motion of the point vortex system is, therefore, characterized using the (X, Y) phase space topology, consisting of the level curves of Hamiltonian. The phase plane is parameterized by the linear impulse through $\mathbb{P}$ and the vortex strengths through γ.

It should be noted here that in Fig. 3.1, $y_1 > 0$ and $y_2 < -y_1$, which gives $\mathbb{P} < 0$. Note that $\mathbb{H}$ is invariant under the transformation $\{Y \to -Y, \mathbb{P} \to -\mathbb{P}\}$. In general (i.e. unless $\mathbb{P} = 0$), the phase space representation is not symmetric about the X axis, so changing the sign of $\mathbb{P}$ corresponds to a reflection about the X-axis. Changing the sign of $\mathbb{P}$ is equivalent to changing the signs of all the point vortices, which also reverses the direction of the phase space trajectories and the direction of net vortex translation in physical space. In comparisons with experiments (to follow in Chapter 4), the vortex locations and circulations for the 2P wakes typically correspond to negative values of $\mathbb{P}$, so we will assume $\mathbb{P} < 0$ throughout this manuscript without any loss of generality. Finally, it is to be further noted that $\mathbb{H}$ is invariant under the transformation $X = X + n\pi$, with $n \in I$.

Discussion of the dynamics follows next by considering in detail a somewhat generic and representative case with $\gamma = 2/5$ and $\mathbb{P} = -1$. This value of γ corresponds to the vortex strength ratio $\Gamma_1 : \Gamma_2 = 2 : 3$. The corresponding phase-space trajectories are shown

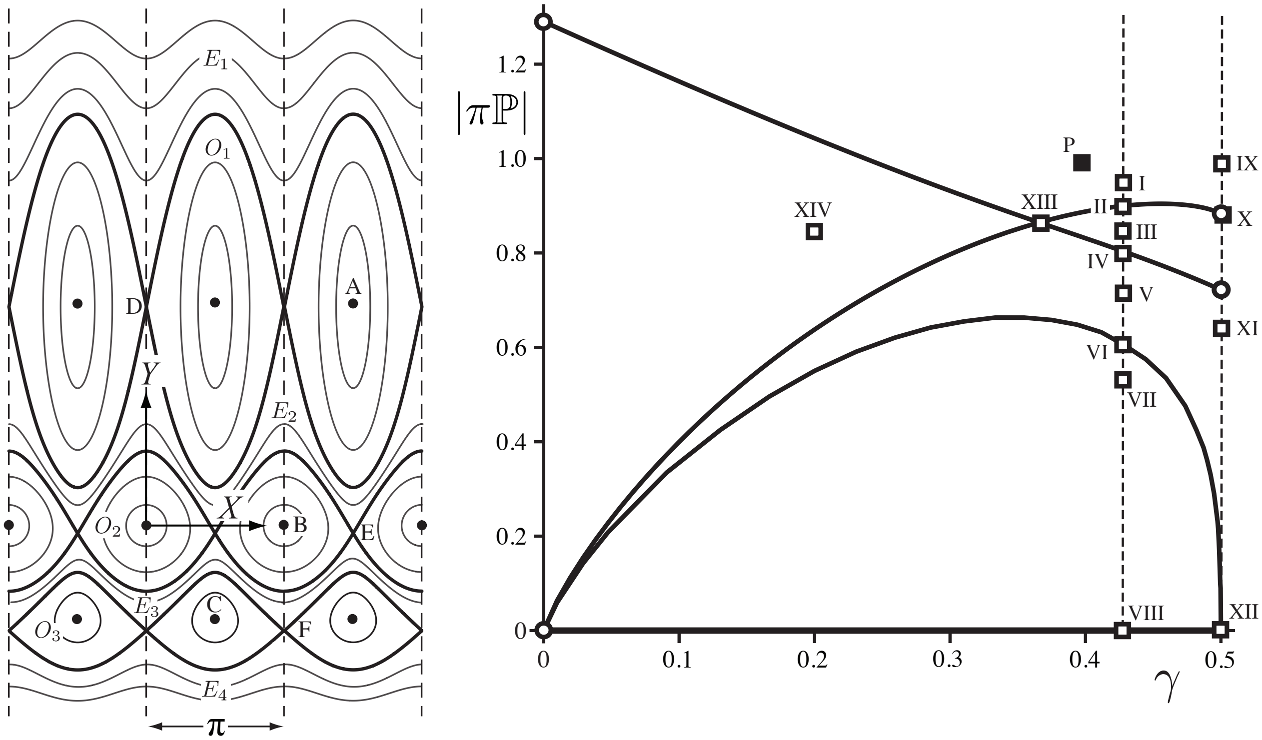

(a)

(b)

Figure 3.2: (a) Model phase space representation for $\gamma = 2/5$ and $\mathbb{P} = -1.0/\pi$. The critical points are marked as A, B, C, D, E, and F. The solid circles represent the stable fixed points, unstable fixed points are at the intersection of two level curves. Level curves are marked with solid lines; separatrices joining the unstable fixed points are shown with heavy lines, and these curves delineate seven distinct regimes of motion. Regimes with orbiting motion are labeled O_i, and those with exchanging motion are labeled E_i. Corresponding real-space vortex trajectories are discussed in §3.2.2. (b) Bifurcation diagram for phase space topology. The diagram has reflective symmetry about $\gamma = 1/2$. The line $\mathbb{P} = 0$ also is a bifurcation curve. The solid square (marked as P) corresponds to the representative phase space diagram of panel (a). The open squares correspond to the representative case from each region of the bifurcation diagram, the phase spaces for which have been plotted subsequently. Open cicles indicate singularity.

in Fig. 3.2(a). Each trajectory is a level curve of the Hamiltonian obtained by setting $\mathbb{H} =$ constant, with different curves corresponding to different values of the constant. There are six fixed points (per period) corresponding to relative equilibrium vortex configurations, which are discussed below. The point vortex system exhibits limiting behavior at these (X, Y) inter-vortex separations, which are designated as A, B, C, D, E, and F, marked on Fig 3.2(a). The heteroclinic trajectories, or *separatrices*, which join the unstable fixed points, divide the phase space into seven distinct *regimes of motion*. All initial conditions from within a given regime of motion lead to qualitatively similar relative vortex motions, as discussed in §3.2.2.

Three of these fixed points, the centers labeled A–C (and their periodic images), are Lyapunov stable to perturbations that preserve the vortex strengths, the assumed reflective symmetry, and the value of the impulse. Note that perturbations of these cases will not preserve the value of the Hamiltonian. The saddle points labeled D–F (and their periodic images) are unstable to infinitesimal perturbations. In these latter three cases it is possible to maintain the value of the Hamiltonian under perturbation, in which case the phase space trajectory will move along a separatrix as the vortex configuration evolves from one relative equilibrium to another.

Consider first the point labeled B, for which $Y = 0$ and $X = n\pi$ (with n any integer), giving $z_1 = z_2 \pm nL$ and $\zeta_1 = \zeta_2 \pm (n-1)L$. That is, for this point in phase space the positions of the like-signed vortices coincide, giving a singular case in which the Hamiltonian in equation (3.7) is infinite. This relative equilibrium configuration consists of a staggered 2S street of vortices having strengths of $\pm(\Gamma_1 + \Gamma_2) = \pm\mathbb{S}$. The vortex arrangement for this case is shown in Fig. 3.3(B) together with streamlines in the comoving frame of reference. The horizontal (streamwise) spacing between neighboring, oppositely-signed vortices is $L/2$ and the vertical (spanwise) spacing is $b = |\mathbb{P}|\, L/\pi$. This vertical spacing is slightly larger than that determined by von Kármán to give a linearly stable 2S configuration, namely $\cosh(\pi b/L) = \sqrt{2}$, or $b \approx 0.881\, L/\pi$ [12]. This comparison highlights the importance of the perturbation employed when considering vortex street stability: the 2S street corresponding to point B is unstable to perturbations in the vortex locations that break the 2S symmetry and keep the number of vortices fixed at two per period [12], but it is stable to perturbations in which each vortex is split into two vortices (notably with unequal strengths) that preserve the spatial symmetry and the linear impulse.

Point A is also a singular case with infinite $\mathbb{H}$. When $X = (1 + 2n)\pi/2$, the oppositely signed vortices coincide when $y_1 = -y_2$ (namely z_1 with ζ_2 and z_2 with ζ_1), which by equation (2.7b) gives $\Delta y = \mathbb{P}L/(2\gamma - 1)$. This relative equilibrium configuration, illustrated in Fig. 3.3(A), consists of two widely spaced rows of oppositely signed vortices with strengths of $\pm\,(\Gamma_1 - \Gamma_2) = \pm 2\mathbb{Q}\,\mathbb{S}$.

Point C corresponds to a unique relative equilibrium configuration that is Lyapunov stable and consists of four separate base vortices, as illustrated in Fig. 3.3(C). The value of Y is determined numerically by solution of $\partial\mathbb{H}/\partial Y = 0$ with $X = \pi/2 + n\pi$. The corresponding value of $\mathbb{H}$ is finite and is a local minimum. Each vortex pair consists of two vertically aligned vortices of opposite circulation. The circulation magnitudes are unequal, which in isolation would cause a vortex pair to travel on a circular path about the center of vorticity, but in this case the cumulative effect of the image vortices restricts all motion to be parallel to the x-axis. Perturbations of this vortex configuration leads to relative vortex motion from regime O_3, as discussed in §3.2.2.

The relative equilibrium vortex configuration corresponding to point D is shown in Fig. 3.3(D). Like that for point C, this configuration consists of staggered vortex pairs in which the vortices in a pair are aligned vertically and travel horizontally. In contrast to the configuration for point C, the vertical offset of the pairs is quite small, and the configuration is unstable

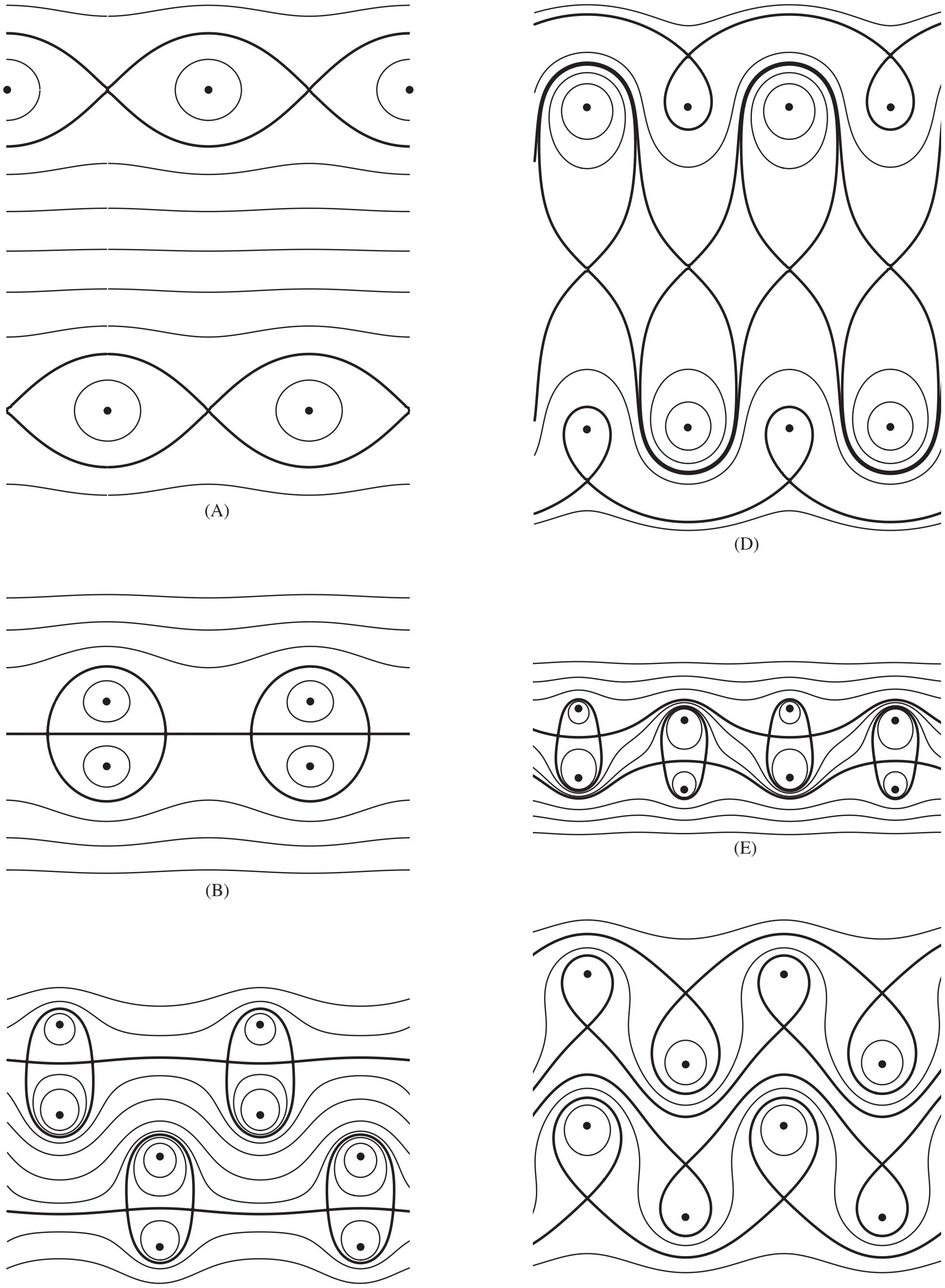

(A)

(D)

(B)

(E)

(C)

(F)

Figure 3.3: Relative equilibrium configurations of vortices in the appropriate co-moving frame of reference for the case $\gamma = 2/5$, $\mathbb{P} = -1/\pi$. Vortex locations are marked with solid circles, and representative streamlines are shown with solid lines; separatrices that join stagnation points in the co-moving frame are shown with heavy lines. Panels are labeled according to the corresponding fixed point in phase space, as shown in Fig. 3.2(a). Each of these configurations translates steadily to the left. Panel C represents a stable configuration; the others are unstable.

to small perturbations in the vortex locations.

Points E and F both have $X = n\pi$ and correspond to two parallel, 2S-like wakes containing vortices of different strengths, as shown in Fig. 3.3(E,F). Point E is very close to producing two parallel lines of vortices with alternating sign. Both of these configurations are unstable to perturbations in the vortex locations.

Vortex motions extracted from within the same regime of phase topology domain are qualitatively similar. The structure of the phase space depends on the values of the constants of motion i.e $\mathbb{P}$ and γ. Bifurcations in the phase space topology occur when the separatrices connect fixed points of multiple types at specific values of γ and $\mathbb{P}$. Fig. 3.2(b) shows the curves for the four different bifurcation types; depicting the values of $\mathbb{P}$ at which bifurcations occur for a particular γ. Based on the possible combinations of γ and $\mathbb{P}$, the diagram segregates five distinct regions of vortex motion. Phase plane figures that correspond to points from the same region are qualitatively equivalent. This imples that similar types of vortex trajectories in real space would result from the numerical integration of (3.1) by considering the motion along the Hamiltonian level curves of such phase plots. The diagram (Fig. 3.2(b)) has reflective symmetry about $\gamma = 1/2$ in the interval $\gamma \in [0, 1]$, which essentially covers all possible relative vortex strengths. For $\Gamma_1/\Gamma_2 \leq 1$, the quantity $\gamma \in [0, 1/2]$ and when $\Gamma_1/\Gamma_2 > 1$, the quantity $\gamma \in (1/2, 1]$.

Representative phase plane diagrams from each region of Fig. 3.2(b) are shown in Fig. 3.4 and Fig. 3.5. The points are marked on Fig. 3.2(b) by Roman numerals and correspond to the similarly-numbered panels of Figs. 3.4 and 3.5. Points I, II, III, IV, V, VI, VII, and VIII depict the evolution of the phase space topology as $\mathbb{P}$ is varied, when the relative vortex strength ratio Γ_1/Γ_2 is 3/4 (or, $\gamma = 3/7$). In Fig. 3.4, the panels marked as II, IV, VI, and VIII respectively exhibit the four different types of bifurcation. In panel II, the (unstable) fixed points belonging to the critical vortex configurations D and F get connected by a sepa-

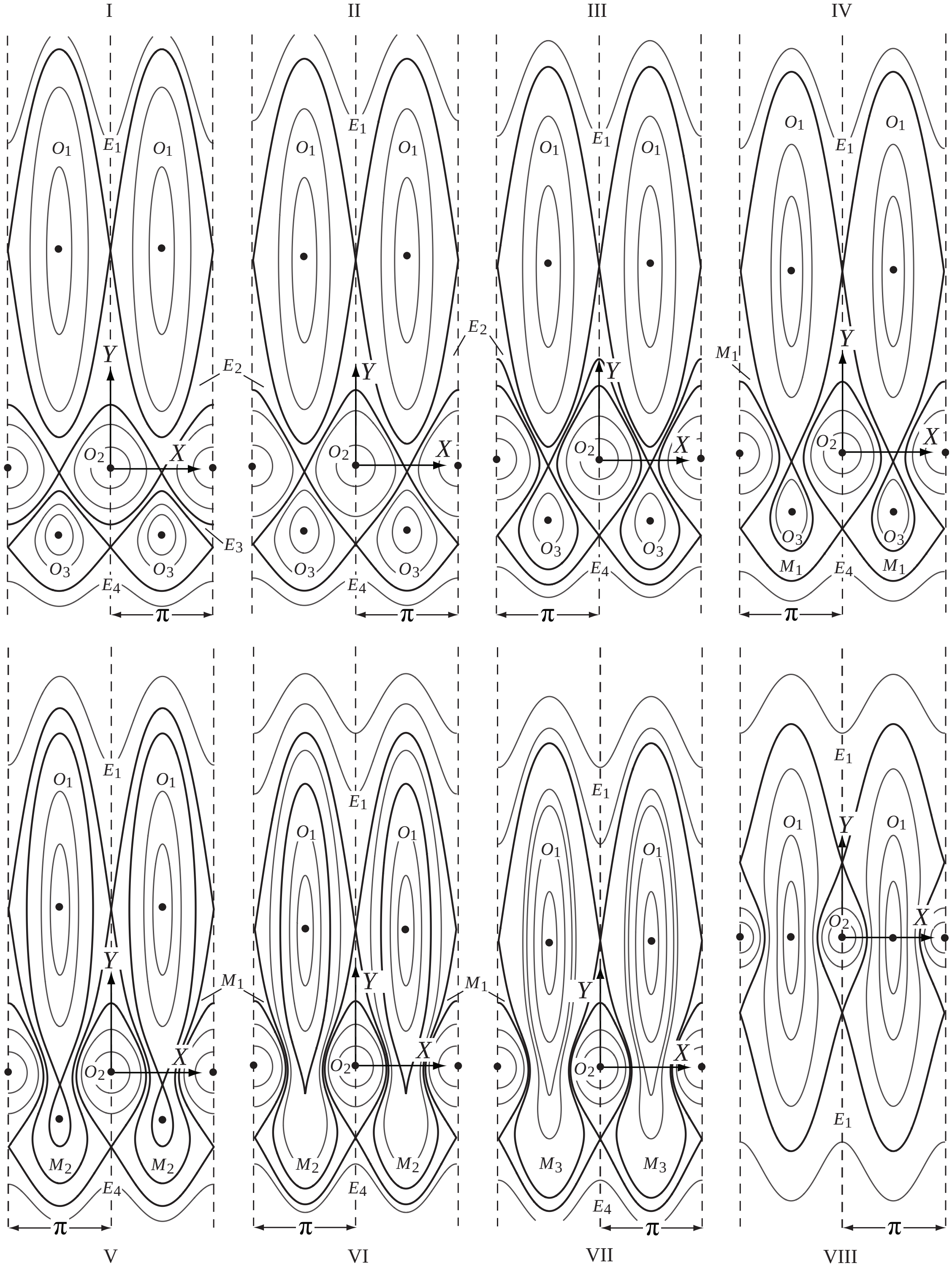

Figure 3.4: Representative phase space topology (panels are marked by Roman numerals which correspond to the similarly-numbered points in Fig. 3.2(b) and represent the phase space for the values of $|\mathbb{P}|$ and γ at the respective points). In this figure, all the phase diagrams are for $\gamma = 3/7$ as $\mathbb{P}$ is varied.

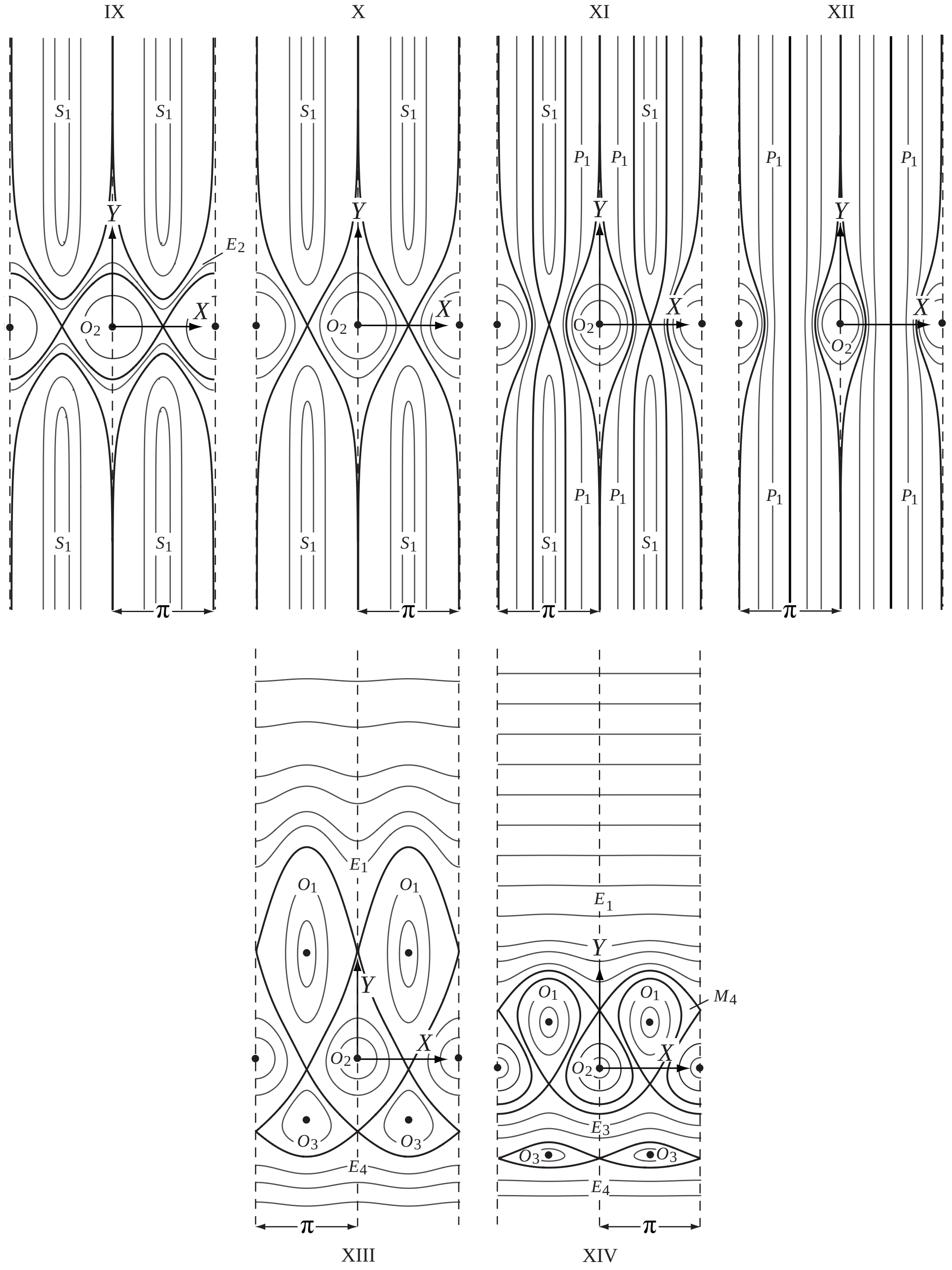

Figure 3.5: Representative phase space topology (panels are marked by Roman numerals which correspond to the similarly-numbered points in Fig. 3.2(b) and represent the phase space for the values of $|\mathbb{P}|$ and γ at the respective points). For panels IX – XII: $\gamma = 1/2$ as $\mathbb{P}$ is varied. The parameter values for panels XIII and XIV are respectively $\gamma = 0.37$, $\mathbb{P} = -0.86/\pi$ and $\gamma = 0.20$, $\mathbb{P} = -0.85/\pi$

ratrix. This causes an inherent change in the topology of the phase space. Panel IV involves the bifurcation owing to the connection between the (unstable) fixed points belonging to the critical cases D and E. Following this, the (stable) fixed point belonging to configuration C and the (unstable) fixed point belonging to configuration D mutually approach and eventually annihilate each other, thereby causing the third bifurcation type (shown in panel VI). In panel VIII, the (unstable) fixed points belonging to critical configurations E and F get connected by a level curve.

In Fig. 3.5, the panels IX, X, XI, and XII correspond to the situation when $\Gamma_1 = \Gamma_2$ (or, $\gamma = 1/2$). The phase space become symmetric about the horizontal axis in this case and the phase structures are vertically stretched versions of those in Fig. 3.4, so that the (unstable) fixed points, corresponding to the vortex configurations E and F, lie at $(X, Y) = (0, +\infty)$ and $(X, Y) = (0, -\infty)$ respectively. The fixed points for the configuration D move to $(X, Y) = (n\pi/2, 0)$ and thus get oriented along the wake centerline. Panel XIII refers to the case when two of the bifurcation types merge and occur simultaneously. Here the fixed points corresponding to the critical configurations E, D, and F get connected by a level curve. When $\gamma \neq 1/2$, it represents a unique point in the $(\gamma, \mathbb{P})$ plane and can happen only when $\gamma \approx 0.37$ and $|\mathbb{P}| \approx 0.86/\pi$.

The special case $\gamma = 0$

Taking $\gamma = 0$ corresponds to setting $\Gamma_1 = 0$, in which case the 'restricted four-vortex problem' consists of passive particles at locations z_1 and ζ_1 being advected by point vortices at locations z_2 and ζ_2. These (non-zero) vortices are arranged in a 2S street with horizontal spacing L and vertical spacing $b = 2\,y_2$. Since the passive particles have no influence on the dynamics of the vortices, the phase space representation is equivalently the real space representation for the passive particle motion in a frame of reference moving with the vortices. Depending

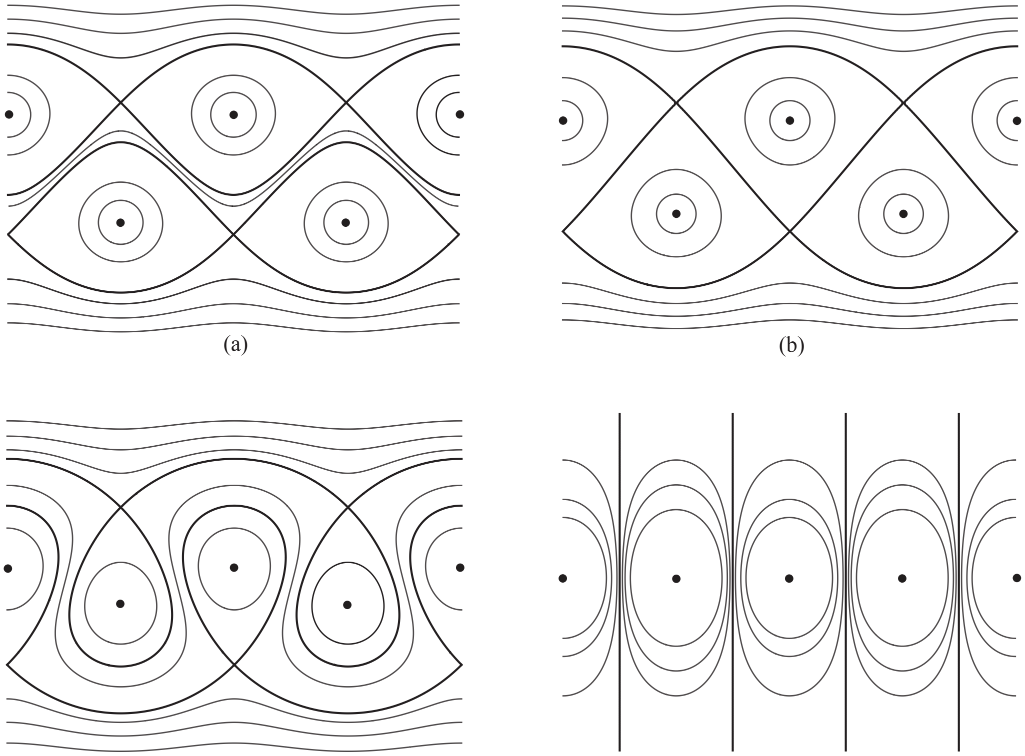

Figure 3.6: Phase space representations for $\gamma = 0$. The $|\mathbb{P}|$ values are $1.50/\pi$, $1.29/\pi$ (bifurcation point in the phase space topology),$0.50/\pi$ and 0.0 in figures (a), (b), (c), and (d) respectively.

on the value of $\mathbb{P}$, there are four different cases of phase space topology, as shown in Fig. 3.6. Regimes O_1, O_2, E_1, E_4, and M_1 are present for all non-degenerate values of $\mathbb{P}$ when $\gamma = 0$.

3.2.2 Real space trajectories of the point vortices

Similar to the developments of § 2.3, the trajectories of the point vortices in the physical space are determined by numerical integration of equation (3.1), subject to the imposed constraints (3.5), for given values of γ and $\mathbb{P}$. It is also imperative to identify the Hamiltonian level curve, along the contour of which the integration is performed. Similar types of trajectories occur when the vortex configurations belong to the same region of Fig. 3.2(b), owing to the

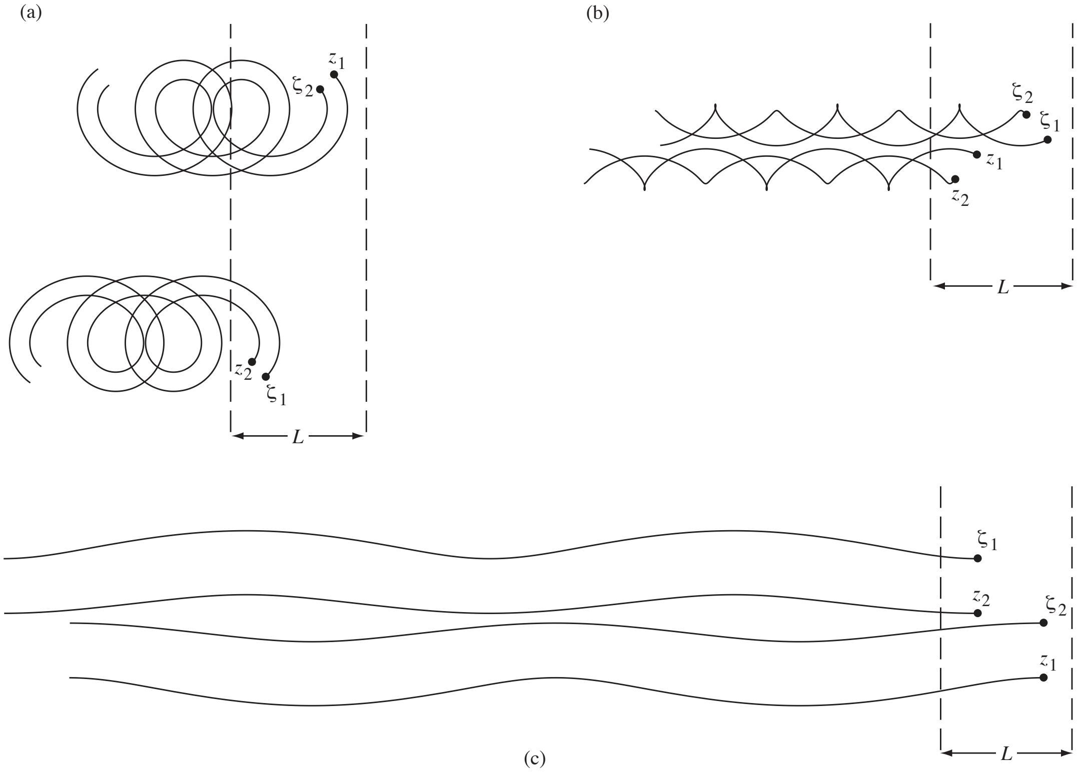

Figure 3.7: Representative vortex trajectories for the orbiting modes, with $\mathbb{P} = -1.0/\pi$, $\gamma = 3/7$. The corresponding phase plane diagram corresponds to Fig. 3.2(a) and is represented by the point P marked on Fig. 3.2(b). Γ_2 is assumed to have a scaled value of $1\,\mathrm{cm}^2/\mathrm{s}$. (a) O_1 regime for elapsed time $\Delta t = 7.2\,L^2/\mathbb{S}\,(1-\gamma)$, (b) O_2 regime for elapsed time $\Delta t = 4.2\,L^2/\mathbb{S}\,(1-\gamma)$, (c) O_3 regime for elapsed time $\Delta t = 19.0\,L^2/\mathbb{S}\,(1-\gamma)$. Solid circles mark the initial positions of the base vortices and solid lines show the base vortex trajectories.

equivalent nature of the phase space structures consisting of the Hamiltonian level curves. Six unique regimes of real space motion are identified, along with a number of sub-categories.

Figs. 3.4 and 3.5 show that for all values of $\mathbb{P}$ there is a regime of motion, labeled O_2, in which the phase trajectories move in closed orbits about the stable fixed point belonging to the critical configuration D, i.e. about $(X, Y) = (n\pi, 0)$. The vortex separations are bounded at all time. A representative example of the corresponding vortex trajectories in the real space is shown in Fig. 3.7(b). Here the like-signed base vortices are very close and as the configuration propagates downstream, these vortices orbit each other. There are also two

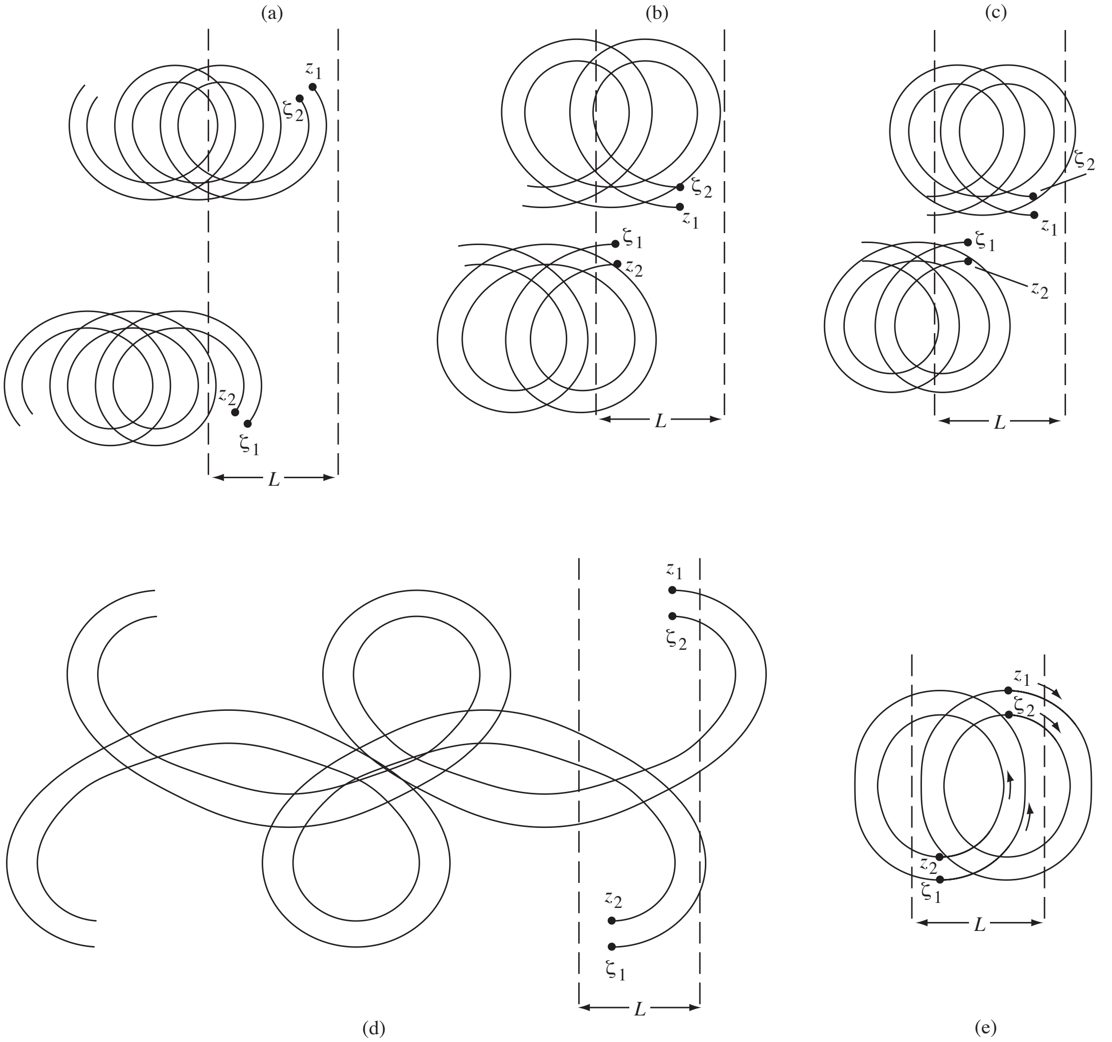

Figure 3.8: Comparison of the physical trajectories for the same class (O_1) of orbiting mode for different selections of the parameter $\mathbb{P}$. The corresponding phase spaces correspond to Fig. 3.4, with $\gamma = 3/7$. Here Γ_2 is assumed to have a scaled value of $1\,\mathrm{cm}^2/\mathrm{s}$. (a) Phase point III, $\mathbb{P} = -0.85/\pi$, $\Delta t = 7.75\,L^2/\mathbb{S}\,(1-\gamma)$, (b) Phase point V, $\mathbb{P} = -0.71/\pi$, $\Delta t = 9.5\,L^2/\mathbb{S}\,(1-\gamma)$, (c) Phase point VI, $\mathbb{P} = -0.605/\pi$, $\Delta t = 7.0\,L^2/\mathbb{S}\,(1-\gamma)$, (d) Phase point VII, $\mathbb{P} = -0.55/\pi$, $\Delta t = 22.0\,L^2/\mathbb{S}\,(1-\gamma)$, (e) Phase point VIII, $\mathbb{P} = 0$, $\Delta t = 6.0\,L^2/\mathbb{S}\,(1-\gamma)$. Solid circles mark the initial positions of the base vortices and solid lines show the base vortex trajectories.

other types of motion where the phase trajectories move in closed orbits and are labeled as O_1 and O_3 in Figs. 3.4 and 3.5. These (O_1, O_2, O_3) are, in general, referred to as the *orbiting modes*. Fig. 3.8 compares the O_1 trajectories for various selections of $\mathbb{P}$. In this motion,

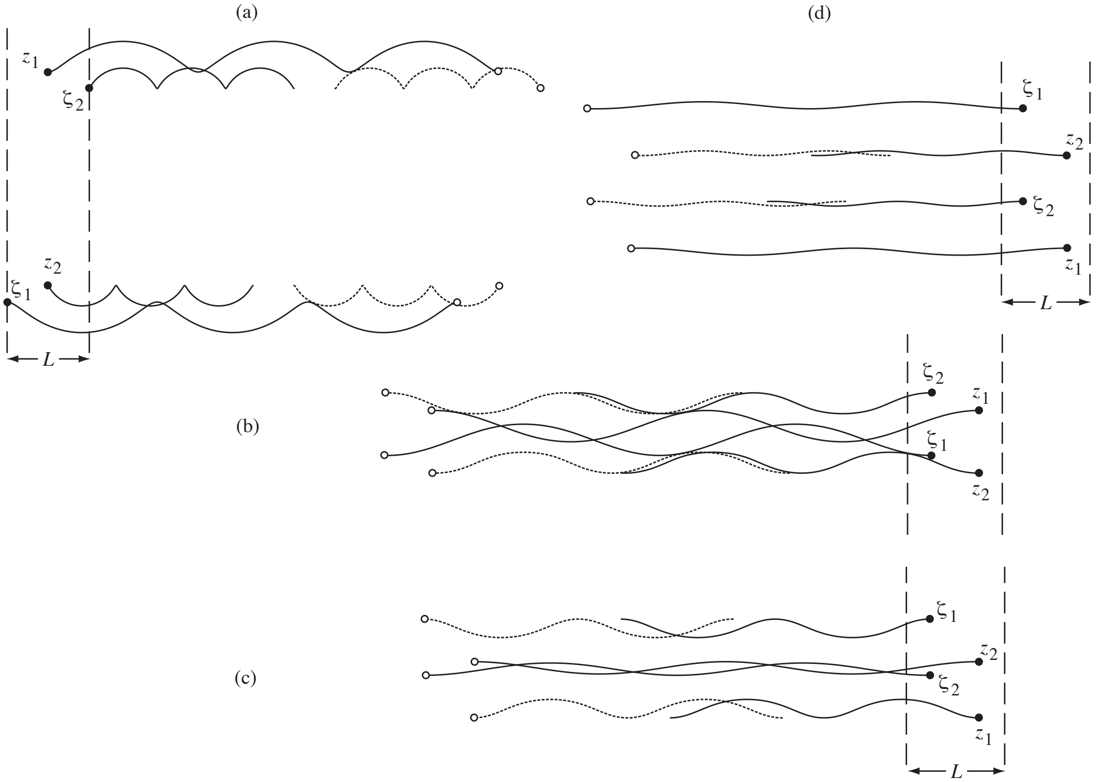

Figure 3.9: Representative vortex trajectories for the exchanging modes, with $\mathbb{P} = -1.0/\pi$, $\gamma = 0.40$. The corresponding phase plane diagram corresponds to Fig. 3.2(a) and is represented by the point P marked on Fig. 3.2(b). Γ_2 is assumed to have a scaled value of $1\,\mathrm{cm}^2/\mathrm{s}$. (a) E_1 regime for elapsed time $\Delta t = 20.8\, L^2/\mathbb{S}\,(1-\gamma)$, (b) E_2 regime for elapsed time $\Delta t = 8.0\, L^2/\mathbb{S}\,(1-\gamma)$, (c) E_3 regime for elapsed time $\Delta t = 8.5\, L^2/\mathbb{S}\,(1-\gamma)$, (d) E_4 regime for elapsed time $\Delta t = 15.0\, L^2/\mathbb{S}\,(1-\gamma)$. Solid circles mark the initial positions of the base vortices and solid lines show the base vortex trajectories; open circles and dotted lines show the periodic images.

the phase trajectories move in closed orbits about the (stable) fixed point for the critical configuration B, i.e. about the point $(X, Y) = (n\pi/2, k)$, with k positive finite. The O_1-type exists for all $\mathbb{P}$, except when the vortex strengths Γ_1 and Γ_2 are equal. The representative real space trajectories are shown in Fig 3.7(a). The vertical separation between the vortex pairs is constrained, but it is too large for the like-signed vortices to orbit one another. The O_3-type of motion also exists for all values of $\mathbb{P}$, except when there is a simultaneous occurence of two different bifurcations (shown in panel VIII of Fig. 3.4) and when the vortex

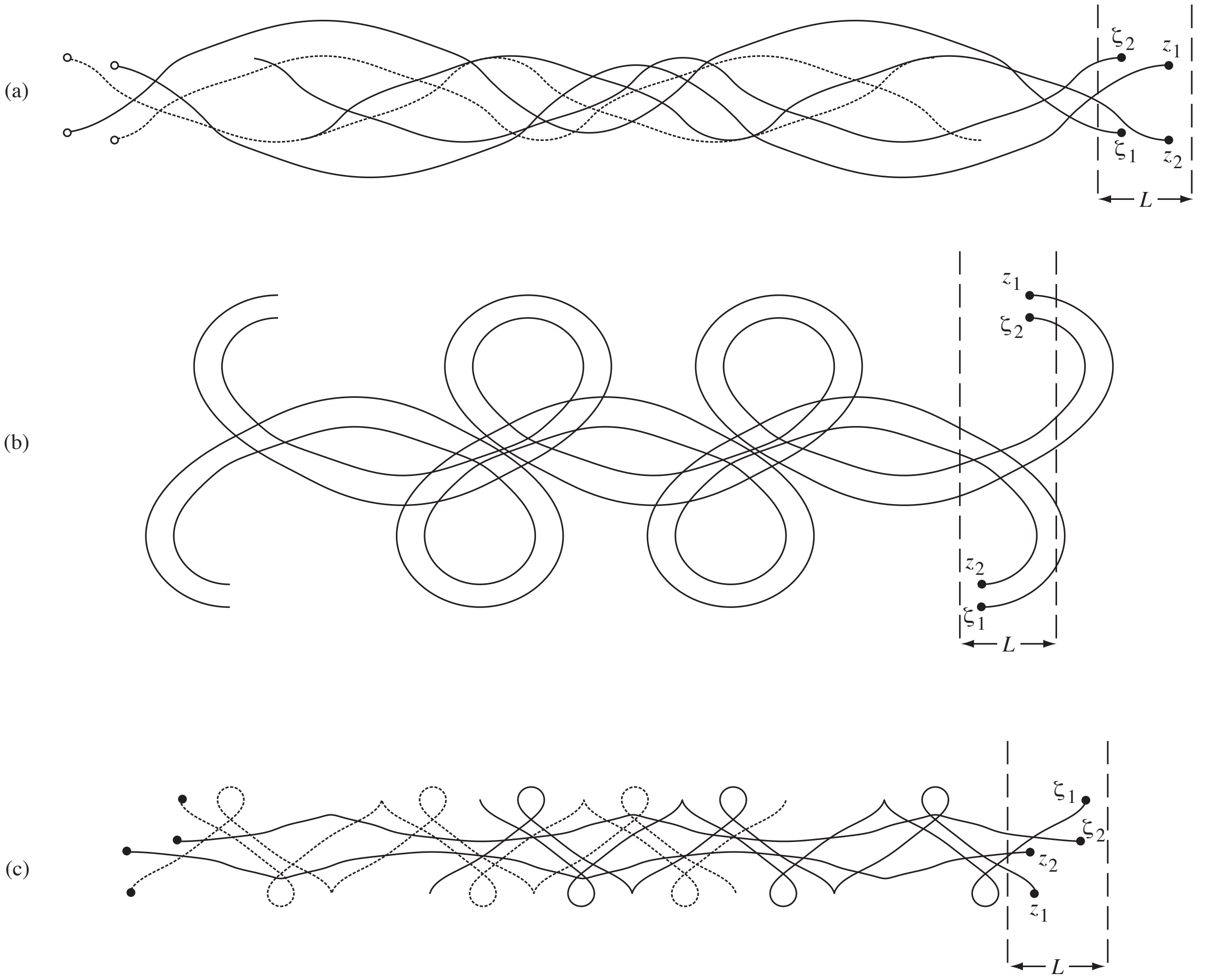

Figure 3.10: Representative vortex trajectories for the three types of mixed modes. The first two (M_1, M_2) correspond to the parameter values $\mathbb{P} = -0.605/\pi$, $\gamma = 3/7$ (the corresponding phase plane diagram is shown in panel VI of Fig. 3.4). The third (M_3) corresponds to the parameter values $\mathbb{P} = -0.85/\pi$, $\gamma = 1/5$ (the corresponding phase plane diagram is shown in panel XIV of Fig. 3.5). Γ_2 is assumed to have a scaled value of $1\,\mathrm{cm}^2/\mathrm{s}$. (a) M_1 regime for elapsed time $\Delta t = 31.0\,L^2/\mathbb{S}\,(1-\gamma)$, (b) M_2 regime for elapsed time $\Delta t = 43.35\,L^2/\mathbb{S}\,(1-\gamma)$, (c) M_3 regime for elapsed time $\Delta t = 24.2\,L^2/\mathbb{S}\,(1-\gamma)$. Solid circles mark the initial positions of the base vortices and solid lines show the base vortex trajectories; open circles and dotted lines show the periodic images.

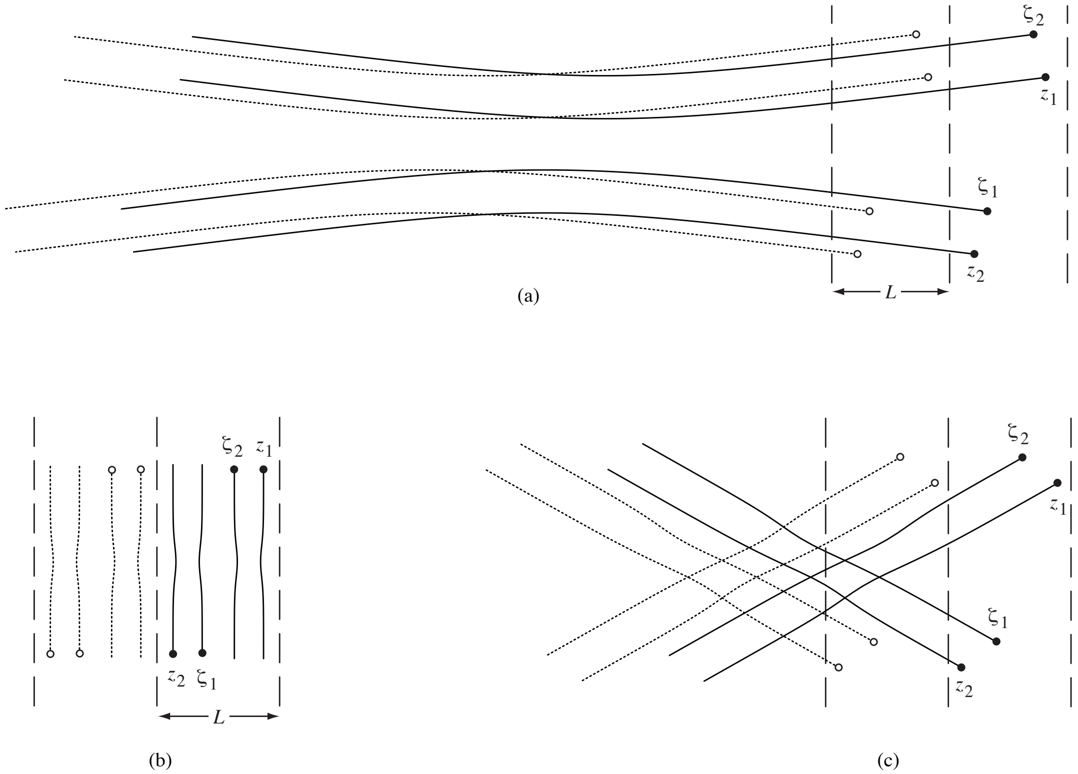

Figure 3.11: (a) Representative vortex trajectories for the scattering mode from the S_1 regime, with $\mathbb{P} \approx 1.15/\pi$, $\gamma = 1/2$. The elapsed time is $\Delta t = 12.0\, L^2/\mathbb{S}\,(1-\gamma)$. (b) Representative vortex trajectories for the passing mode from the P_1 regime, with $\mathbb{P} = 0$, $\gamma = 1/2$. The elapsed time is $\Delta t = 2.5$. (c) Representative vortex trajectories for the passing mode from the P_1 regime, with $\mathbb{P} \approx 0.66$, $\gamma = 1/2$. The elapsed time is $\Delta t = 6.0\, L^2/\mathbb{S}\,(1-\gamma)$. It is assumed that Γ_2 has a scaled value of $1\,\mathrm{cm}^2/\mathrm{s}$. Solid circles mark the initial positions of the base vortices and solid lines show the base vortex trajectories; open circles and dotted lines show the periodic images.

strengths Γ_1 and Γ_2 are equal. Here the phase trajectories move in closed orbits about the (stable) fixed point for the critical configuration F, i.e. about $(X, Y) = (n\pi/2, k)$, with k being negative finite. The corresponding representative vortex trajectories in the physical space are shown in Fig. 3.7(c). The transverse separation between the like-signed vortices is constrained, but it is still too large for the vortices to orbit around one another. The separation however fluctuates periodically in a wavy motion as the configuration propagates downstream. The spatial extent of all these orbiting modes depends on the values of the parameters γ and $\mathbb{P}$.

Panels I, II, and III in Fig. 3.4 and panel IX in Fig. 3.5 exhibit a type of phase trajectory, labeled as E_2. In this motion, X is unbounded while Y remains bounded. Owing to the spatial periodicity of the system, as $|X|$ increases, vortices that may initially be identified as a pair will successively exchange partners with the neighboring image pairs. A representative example of the real space trajectories is shown in Fig. 3.9(b). A similar type of motion, labeled as E_3, is seen in panel I in Fig. 3.4, but here the Y separation between the positive base vortices is always negative. Representative vortex trajectories are shown in Fig. 3.9(c). There are two other types of such exchanging motion, labeled as E_1 and E_4 on Figs. 3.4 and 3.5. The corresponding real space trajectories are shown in Figs. 3.9(a) and 3.9(d) respectively. In general, these (E_1, E_2, E_3, and E_4) are referred to as the *exchanging modes*.

Four entirely new regimes of motion are further identified from the topological behavior of the phase space structures. The corresponding phase trajectories are labeled as M_1 in panels IV, V, VI, VII; M_2 in panels V and VI, M_3 in panel VII (both in Fig. 3.4); and M_4 in panel XIV (in Fig. 3.5). These are *mixed modes* exhibiting properties of both orbiing motion and exchanging motion. The representative vortex trajectories for M_1, M_2, and M_3 are shown in Fig. 3.10. Note that the extent of predominance of the features of orbiting and/or exchanging motion(s) depends on the evolution and the present value of Δx and varies periodically as the wake propagates downstream.

Finally consider the special case when $\gamma = 1/2$. The symmetric topology (about the X-axis) of the phase space leads to the development of two distinct types of phase motion. They have been labeled as S_1 in panels IX, X, XI, XII and P_1 in panels XI, XII in Fig. 3.5. In the S_1 regime, X stays bounded while Y is unbounded. Phase trajectories initiating with a large $|Y|$ (and an appropriate X) approach the horizontal X-axis without crossing it, and then again diverge out to large $|Y|$. This regime exists for all $|\mathbb{P}| > 0$ (with $\gamma = 1/2$).

Representative real space motion is shown in Fig. 3.11(a). Here two obliquely translating 2S vortex streets propagate towards each other while approaching the wake asis, there is a reorientation in the translating pairs owing to the mutual interaction and eventually the streets move away from each other. This regime is named as the *scattering mode.* The motion is similar to the 'direct scattering' phenomenon observed during the collision of two vortex pairs on the unbounded plane [30]. The regime labeled as P_1 is considered next. Here also the Y is unbounded and the phase space trajectories pass through through the X-axis. Representative examples of the vortex motion in the physical space are shown in Figs. 3.11(a) and 3.11(b). This regime is referred to as the *passing mode.* It involves two 2S streets approaching each other. They finally cross the wake centerline and continue on their oblique trajectories. The spatial extent of this regime in the (X, Y) plane increases with decreasing $|\mathbb{P}|$, after it first emerges following the bifurcation at $|\mathbb{P}| \approx 0.88/\pi$ (with $\gamma = 1/2$) when the fixed points at $(0, \pm\infty)$ and $(n\pi/2, 0)$ get connected by a separatrix.

Thus, to summarize, the following different regimes of vortex motion have been broadly identified:

- *Orbiting modes*: Three sub-types (O_1, O_2, O_3) are observed. Based on the transverse separation between the vortex pairs, the base vortices (a pair of like-signed/oppositely-signed vortices based on the parameter values) actually orbit one another or mutually approach each other periodically. However, the spanwise separation between the base vortices stays bounded.

- *Exchanging modes*: Four sub-types (E_1, E_2, E_3, E_4) are identified based on the location of the phase trajectories on the Z plane. The transverse separation between the vortices is constrained, but the four base vortices continually separate in the streamwise direction. There is also a periodic exchange of partners between the neighboring vortex pairs.

- Four types of *mixed modes*: These are labeled as M_1, M_2, M_3, and M_4; and exhibit characteristics of both orbiting as well as exchanging motion.

- *Scattering modes*: These are labeled as S_1. Based on the initial conditions, the two 2S streets propagate towards each other while approaching the wake centerline. However, there is a reorientation in the pairs owing to the mutual interaction and finally they diverge away from horizontal axis, instead of crossing it.

- *Passing mode*: These are labeled as P_1. Here two 2S vortex streets approach each other obliquely, eventually cross the wake axis and then they continue on their oblique trajectories. Thus, the two 2S wakes cross each other instead of scattering. Both for the scattering as well as the passing mode, owing to the transient interactions between the vortex pairs, the existence of a four vortex configuration is very brief.

Publication based on the contents of this chapter will follow in [31]. Also refer to [32], [33], and [34] for associated reading.

Chapter 4

Comparisons with physical experiments for the staggered model

4.1 Soap film experiments with a flapping foil

The experiments (Fig. 4.1 shows reprsentative experimental wakes, generated by the research group of Dr. Anders Andersen at DTU, Denmark) photograph the 2P wakes formed behind a rigid foil in a two-dimensional free stream, created by a vertically flowing soap film driven by gravity. In the experiments, a symmetric foil (Fig. 4.2) with a round leading edge and a sharp trailing edge is driven with simple harmonic pitching oscillations. The oscillations are characterized by two dimensionless parameters that can be varied independently, i.e. the width-based Strouhal number $St_D = Df/U$, and the dimensionless amplitude $A_D = 2A/D$, where D is the width of the foil, f is the frequency of the simple harmonic oscillation, U is the free-stream flow speed and A is the flapping amplitude. The vortex structures in the soap film are observed by following thickness variations visualized using a monochromatic light source which gives rise to interference fringes formed by the light reflected at the front

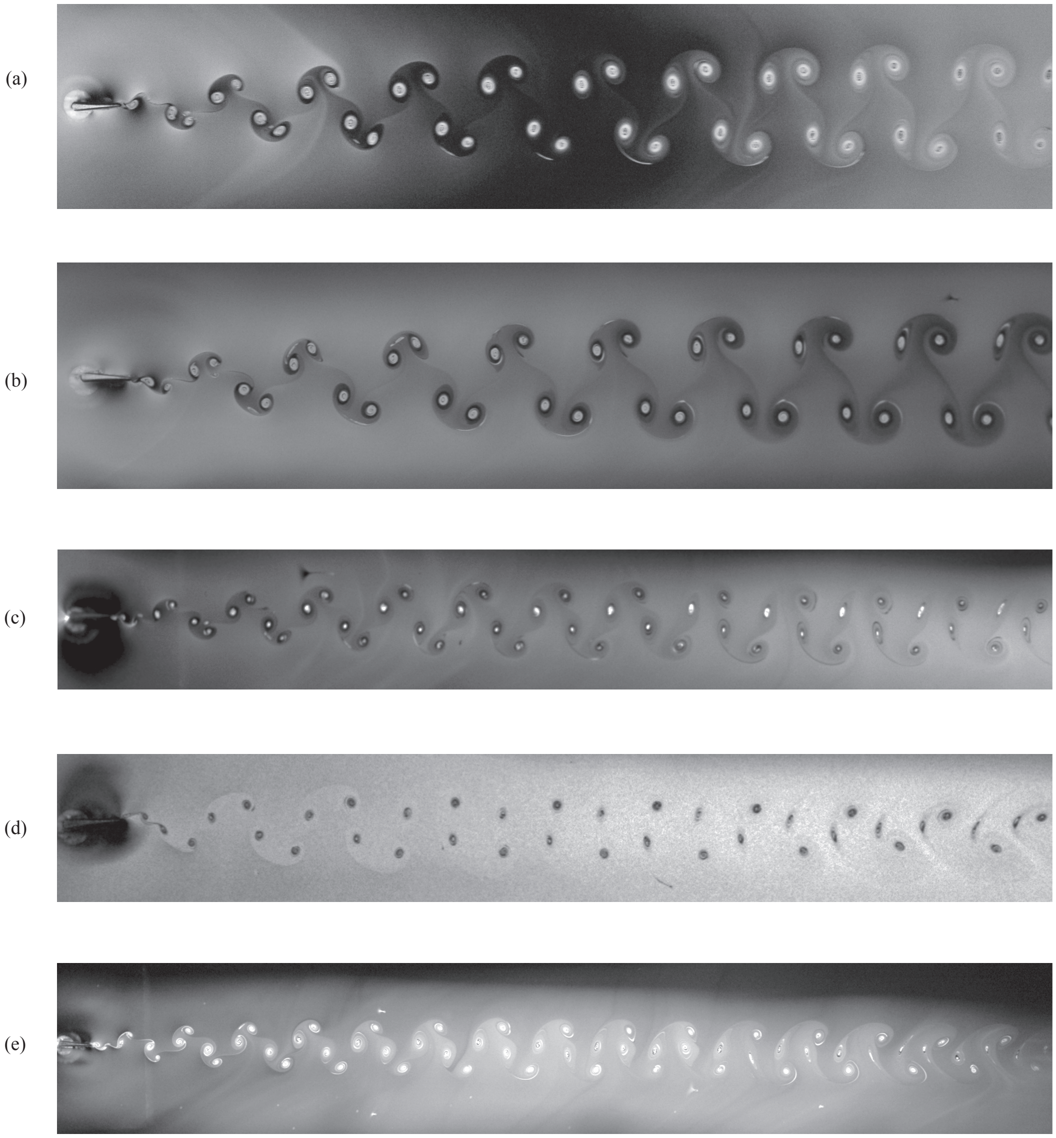

Figure 4.1: Experimental wakes generated by the flapping foil with chord length $C_e = 0.60\,\mathrm{cm}$ and thickness $D_e = 0.10\,\mathrm{cm}$ in a flowing soap film. (a) Experiment 1 [5]: Background velocity is $U_e = 190\,\mathrm{cm/s}$ with $Re \approx 280$. The foil flaps up and down with frequency $f_e = 166.5\,\mathrm{s}^{-1}$ and amplitude $A_D = 1.5$. (b) Experiment 2 [1]: Background velocity is $U_e = 150\,\mathrm{cm/s}$ with $Re \approx 220$. The foil flaps up and down with frequency $f_e = 120.0\,\mathrm{s}^{-1}$ and amplitude $A_D = 1.4$. (c) Experment 3: Background velocity is $U_e = 170\,\mathrm{cm/s}$ with $Re \approx 250$. The foil flaps up and down with frequency $f_e = 135.0\,\mathrm{s}^{-1}$ and amplitude $A_D = 0.73$. (d) Experiment 4: Background velocity is $U_e = 170\,\mathrm{cm/s}$ with $Re \approx 250$. The foil flaps up and down with frequency $f_e = 148.4\,\mathrm{s}^{-1}$ and amplitude $A_D = 1.07$. (e) Experiment 5: Background velocity is $U_e = 170\,\mathrm{cm/s}$ with $Re \approx 250$. The foil flaps up and down with frequency $f_e = 134.7\,\mathrm{s}^{-1}$ and amplitude $A_D = 0.79$. For all the experiments, the flow is from left to right, and the foil rotates about a point near its left edge. See [1] for the procedural details of the experiments.

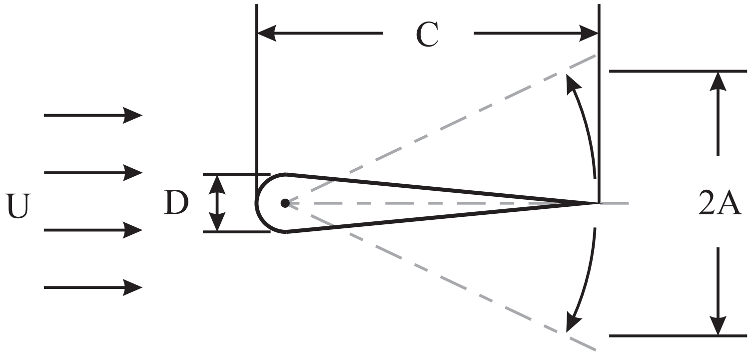

Figure 4.2: A schematic representation of the oscillating foil which is used to generate vortex wakes on a flowing soap film through the shedding mechanism [1]. Here U is the background flow velocity of the soap film. Image is provided by A. Andersen.

and at the back of the film. By varying the structural oscillation and the flow parameters, it is possible to generate widely different wake configurations. This document includes the comparison of three such experimental vortex streets with model predictions. For a more detailed description of the experiments and the soap film technique, see [1], [5] and the references therein.

4.2 Comparison of the model with experimental wakes

The point vortex model is substantiated by making a quantitative comparison between the model results and the vortex dynamics of the bluff body wakes observed in the soap film experiments. The five experiments shown here (Figs. 4.1) represent motions from the different characterized regimes. Despite the soap film flow not being a two-dimensional Newtonian flow, a good correspondence is observed between the model and the experiments.

The mathematical framework, discussed so far, in general consists of N point vortices in an otherwise quiescent inviscid fluid in a spatially periodic domain. That is, the model vortex motion is produced by interactions between an infinite number of point vortices arranged on N parallel rows, with each cluster of N vortices displaying identical relative motion. In a bluff body wake, on the other hand, the relative vortex motion develops both temporally and spatially owing to the fact that clusters of vortices are shed from the body at successive intervals of time. In most cases the vortices are also moving under the influence of an imposed background flow. In order to use our spatially periodic model to represent the developing wakes shown in Figs. 1.2 and 4.1, it is necessary to make several assumptions.

The model till now primarily considers the motion of four base vortices (Chapter 5 deals with a variant of the model with three base vortices) in a spatially periodic domain in an otherwise quiescent flow and the temporal evolution of the base vortex positions results in the relative vortex motion. On the other hand, in the experiments the shed vortices are swept downstream and the relative motion of the vortices is observed in the spatial evolution of the wake. Thus, a transformation between the model results and the experimental data is essential for a proper comparison. In this regard, two different types of transformation techniques can be employed.

The first one involves locating the experimental vortex positions in a co-moving frame of reference and then comparing them with the evolution of the model base vortices. This involves transformation of the instantaneous experimental vortex positions into (approximated) time-dependent motion by shifting each spatially-distributed cluster of N (here 4) vortices a distance $\pm i\,U/f$ (where f is the shedding frequency). The estimated wavelength of the vorticity production, U_e/f_e (the subscript e is used to denote the experimental values), does not account for expected spatial variations in background velocity or uncertainty in the measured values. Thus we set $U/f = c\,U_e/f_e$ and choose the value of c to minimize the mean squared error between the model and experimental vortex locations in the model frame.

The second transformation involves the imposition of this background flow on to the evolving dynamics of the model vortices and then their positions are compared with the experimental wake vortices. Thus, here the inversion is such that the model vortex locations mimic those in the experimental images. A background velocity U is added to the model, and the vortex locations are recorded at time intervals $t = i/f$. Such a mode of comparison has been shown in Fig. 4.4(d) for the second experimental comparison in the current section.

Locations, grouping and spatial periodicity of the vortex cores are first extracted from the image of the experimental wake. The centers of the point vortices are assumed to be located at the geometric centers of the circular regions of vorticity, illuminated by the interference fringes (formed by reflection of the incident light from the two film surfaces) on the flowing soap film. The spatial periodicity is calculated by averaging the streamwise separation between the "image" vortices, i.e. by calculationg the mean of the horizontal distances between the similar vortices shed during successive shedding cycles. The γ for the experiment as well as the correction factor on the background velocity and the stopping time of integration are, in general, identified based on a fitting procedure that entails two steps. The first step involves choosing the optimum γ and the integration end time for the model motion by minimizing the mean squared error between the model Hamiltonian curve and the experimental Hamiltonian data-set. This model Hamiltonian is obtained by plotting the phase portrait for the averaged $\mathbb{P}$ (based on the periodic data from the experiment) and a varying γ and then identifying the γ and integeration time that gives the best fit between the experimental and the model Hamiltonian. The terminal points on the model Hamiltonian over which the equations of motion are integrated are determined by gradient-based projections from the data points to the model curve. In the second step, the correction factor (the measured velocity during the concerned experiments was not accurate and a ± 5 - 10 % error limit was expected, which validates the presence of the correction factor) on the background velocity is determined by minimization of the mean squared error between the model-predicted vortex locations in the co-moving frame reference and the corresponding experimentally observed vortex positions.

The point vortex model assumes that γ, $\mathbb{Q}$, $\mathbb{P}$, and $\mathbb{H}$ are constants of motion. Using the calculated γ for the best-fit case and taking the experimental mean period length as L, the equations (2.7), (2.9), and (3.7) give $\mathbb{Q}$, $\mathbb{P}$, and $\mathbb{H}$ for each period of the wake. The fact that these values are not conserved through the wake illustrates the limitation of the model. However, the values are sufficiently consistent, so that it is possible to use the average values of the quantities as a basis for comparison between the model and the experiment.

For the 2P wake in Fig. 4.1(a), the first step of our fitting procedure reveals two local minima with similar error values, so we report on both cases here. In both cases we determine $\mathbb{Q}$, $\mathbb{P}$, and $\mathbb{H}$ by averaging across all of the experimental positions. In case A, $\gamma = 0.259$, or $\Gamma_1 : \Gamma_2 \approx 0.35 : 1$, and the corresponding phase space representation is shown in 4.3(a), which has an RMS error in the normalized phase-space positions of 0.069. The model phase space trajectory lies on a closed curve in what has been characterized as an *orbiting regime* [29], in which oppositely-signed vortices orbit about one another as time progresses. Starting and stopping points on the model Hamiltonian trajectory, so that the model-predicted motion can fit with the general trend of the experimental phase motion, are marked by squares as shown in Figs. 4.3(a) and 4.3(c).

The first experimental point lies outside of this regime, but the model result shows good agreement with the remainder of the experimental trajectory. The finite time span covered by the experimental data results in the actual motion exploring only a portion of the possible phase space trajectory shown by the model. In particular, the vortices do not have time to fully reveal an orbiting motion. Thus, over the course of the motion, the relative separation of vortices 1 and 2 increases in the spanwise direction while remaining relatively unchanged in the streamwise direction. Taking $c = 1.10$ then gives the comparison between the model

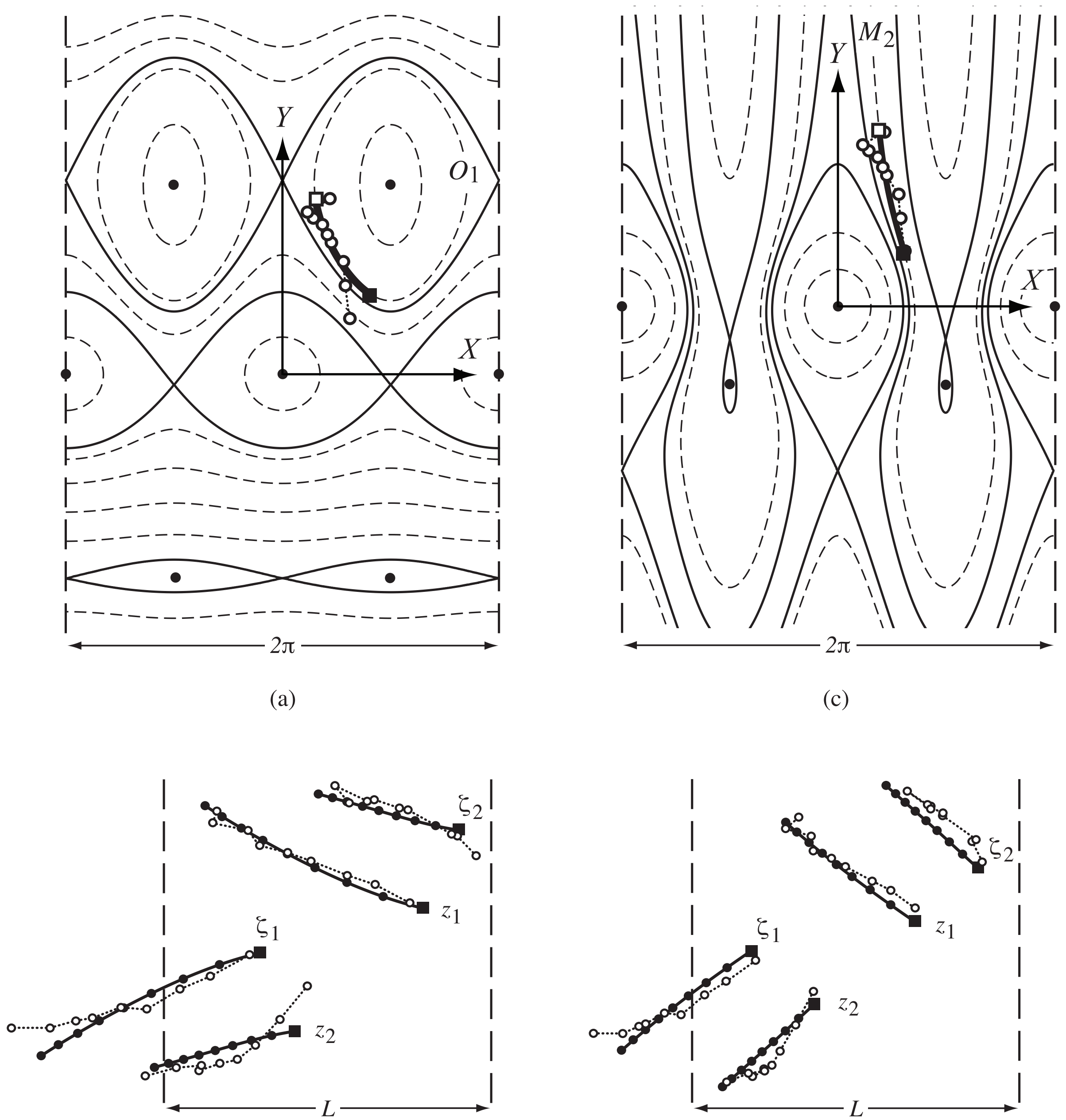

(a) (c)

(b) (d)

Figure 4.3: Comparison of the $N = 4$ model with the 2P wake (experimental wake I) from Fig. 4.1(a) (and also Fig. 1.2(b)). Notation is similar to that in 5.2. (a) **Case A**: Phase space representation for $\gamma = 0.259$ and $\mathbb{Q} + \mathrm{i}\,\mathbb{P} = -0.266 - \mathrm{i}\,0.420$. Experimental phase space positions are again shown with open circles. The model trajectory shown with the heavy line lies along $\mathbb{H} = 0.127$. (b) **Case A**: Vortex trajectories in the model frame of reference corresponding to the phase trajectory in panel (a) are shown with solid lines and circles. Experimental positions transformed with $c = 1.10$ are shown with open circles and are connected sequentially with dotted lines. (c) **Case B**: Phase space representation for $\gamma = 0.454$ and $\mathbb{Q} + \mathrm{i}\,\mathbb{P} = -0.061 - \mathrm{i}\,0.187$. The model trajectory shown with the heavy line lies along $\mathbb{H} = 0$. (d) **Case B**: Vortex trajectories in the model frame of reference corresponding to the phase trajectory in panel (c); experimental positions are transformed with $c = 1.07$. See [6] for the added details of this comparison.

and experimental vortices shown in Fig. 4.3(b); the resulting normalized root mean square (RMS) error in the real space positions is 0.060. The fitted regime here belongs to one of the *orbiting* sub-modes (O_1).

In case B we find $\gamma = 0.454$, or $\Gamma_1 : \Gamma_2 \approx 0.83 : 1$, which gives more uniform vortex strengths than in case A. The corresponding phase space representation is shown in Fig. 4.3(c), which has a normalized RMS error of 0.072. The model trajectory now gives a better fit to the first half of the experimental trajectory, although the remainder of the data is not fit as well. The model trajectory again lies on a closed level curve, but the vertical extent of the curve is much larger than in case A and is not fully shown here. Taking $c = 1.07$ then gives the comparison between the model and experimental vortices shown in Fig. 4.3(d); the corresponding normalized RMS error is 0.054. Thus, case A gives a slightly better fit in phase space, while case B gives a slightly better fit in real space. The model motion is quite similar in both cases A and B, with vortices moving in pairs away from the wake centerline and in the upstream direction. The fitted regime here belongs to one of the *mixed* motion sub-modes (M_2).

Finally an interesting information that is extractable from the comparison of the experiment with the model comes from considering the time scale of vortex motion. Using a scaling argument based on non-dimensionalizing the vortex strengths

$$\frac{\Gamma_e T_e}{L_e^2} = \frac{\Gamma_m T_m}{L_m^2}, \tag{4.1}$$

where Γ_e, T_e, and L_e are the experimental strength magnitude, elapsed time, and spatial period, respectively, and Γ_m, T_m, and L_m are the corresponding model values. Based on the best-fit value of $\Gamma_1/\Gamma_2 = 0.35$ (case A) and 0.83 (case B), the model vortex strength Γ_m can be assumed to be $1.0\,\mathrm{cm}^2/\mathrm{s}$ for the boundary layer vortex (from the roll-up of boundary layers from one side of the foil) and for the trailing edge vortex (from the oscillatory motion at the foil's trailing edge) the strength assumption can be $0.35\,\mathrm{cm}^2/\mathrm{s}$ (case A) and $0.83\,\mathrm{cm}^2/\mathrm{s}$ (case B), and represent the and the trailing edge vortex (from the oscillatory motion at the foil's trailing edge). Further it is assumed that $L_e = L_m = 1.17$ cm, and it has been already found that $T_m = 1.36$ s (case A) and 1.12 s (case B). The corresponding elapsed time for the experiment is $T_e = 8/f = 0.048\,\mathrm{s}$ (vortices in period 1 reach the kth period after $k-1$ shedding cycles). The scaling argument thus predicts an experimental vortex strength of $\Gamma_{BL} \approx 28.3\,\mathrm{cm}^2/\mathrm{s}$ (case A) and $23.3\,\mathrm{cm}^2/\mathrm{s}$ (case B) for the boundary layer vortex and an experimental vortex strength of $\Gamma_{TE} \approx 9.9\,\mathrm{cm}^2/\mathrm{s}$ (case A) and $19.4\,\mathrm{cm}^2/\mathrm{s}$ (case B) for the trailing edge vortex. These values are found to be comparable with the range of values predicted from the scaling arguments of [1]. Assuming a flat plate boundary layer with an outer flow speed of U_e [35], the strength Γ_{BL} is estimated to be

$$\Gamma_{BL} = \frac{1}{2}\int_0^{f_e/2} U_e^2 \;\mathrm{d}t = \frac{U_e^2}{4f_e} \approx 54\,\mathrm{cm}^2/\mathrm{s}. \tag{4.2a}$$

The trailing edge vortex strength is calculated using a simplistic scaling argument [1] which ignores the background free stream flow (thereby underestimating the actual vortex production at the tip),

$$\Gamma_{TE} = \frac{1}{2}\int_0^{f_e/2} V_{TE}^2(t) \;\mathrm{d}t \approx \frac{1}{2}\pi^2 A_e^2 f_e \approx 2.96\,\mathrm{cm}^2/\mathrm{s}, \tag{4.2b}$$

Thus, the order and range of the above values predicted from alternate scaling arguments compare favorably with the values predicted from the model analysis and belong to the same order of magnitude. Experimental measurement of vortex strengths is typically difficult (usually involving sophisticated measurement techniques like particle image velocimetry so as to obtain the velocity field essential to generate the circulation data) and the point vortex model gives a realistic estimate of the vortex circulations.

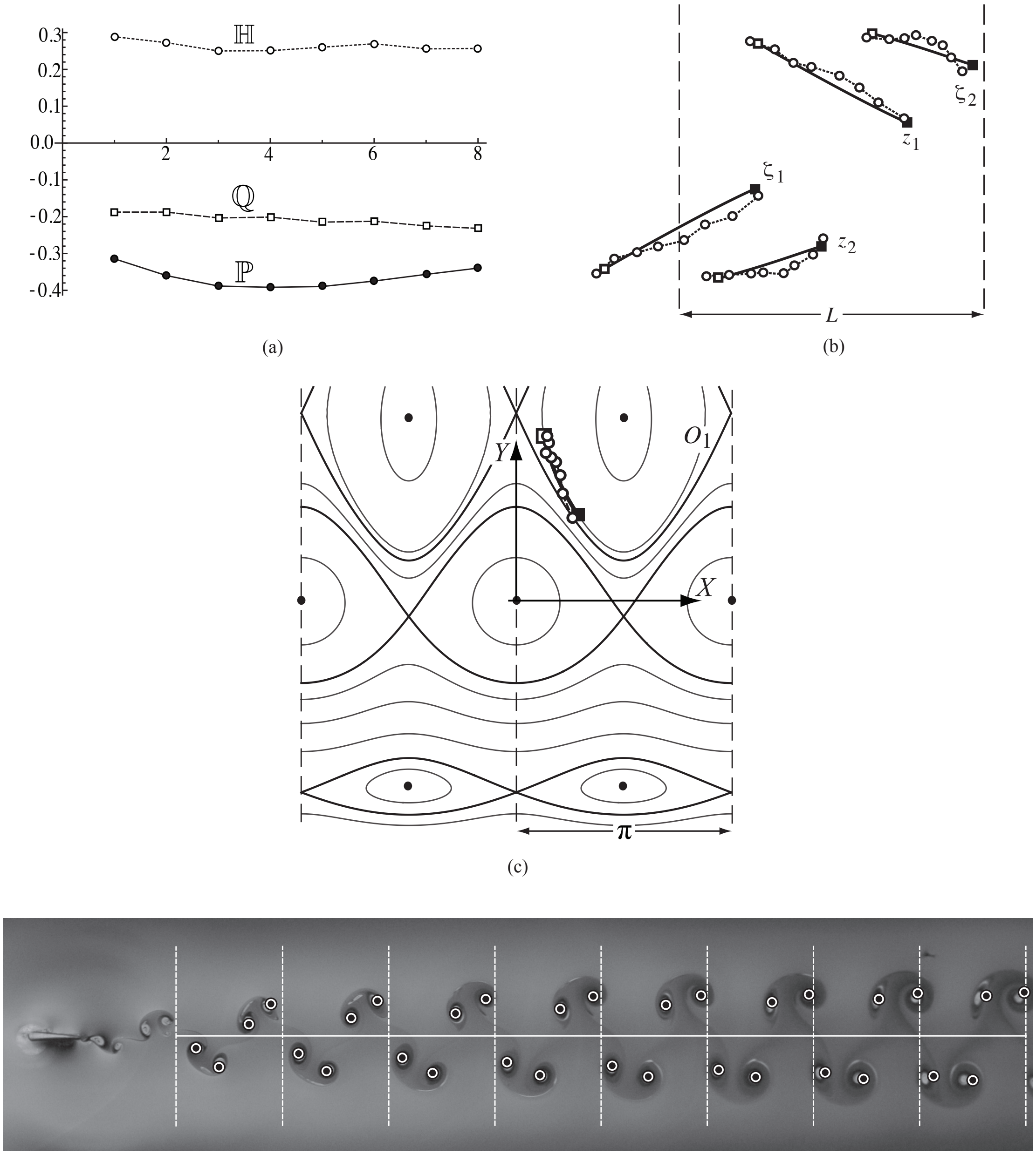

(a) (b)

(c)

(d)

Figure 4.4: Comparison of the point vortex model with the experimental wake II (Fig. 4.1 (b)): (a) Variation of the model constants of motion for the experimental vortex positions. (b) Real-space representation of the experimental data (open circles connected by dashed line) in a co-moving frame ($U = 0$) and the corresponding model trajectories (filled squares and solid lines) obtained by integrating along the level curve indicated in panel (a). Initial positions are marked by the vortex labels. (c) Model phase space representation for $\gamma \approx 0.29$ and $\mathbb{P} = -0.364$. The experimental phase trajectory is marked by open circles joined by dashed line. The model trajectory is marked by filled squares and a heavy line. (d) Experimental wake generated by the flapping foil with chord length $C_e = 0.60\,\text{cm}$ and thickness $D_e = 0.10\,\text{cm}$ in a soap film flowing with a background velocity $U_e = 150\,\text{cm/s}$ at $Re \approx 220$. Flow is from left to right, and the foil flaps up and down with frequency $f_e = 120\,\text{s}^{-1}$ and amplitude $A_D = 1.4$ by rotating about a point near its left edge. The white circles with solid cores mark the postions of the vortices in each spatial period, as predicted by the point vortex model. For both panels (b) and (c), the filled squares mark the starting point of the model trajectory (represented by heavy lines) and the hollow squares the mark end point.

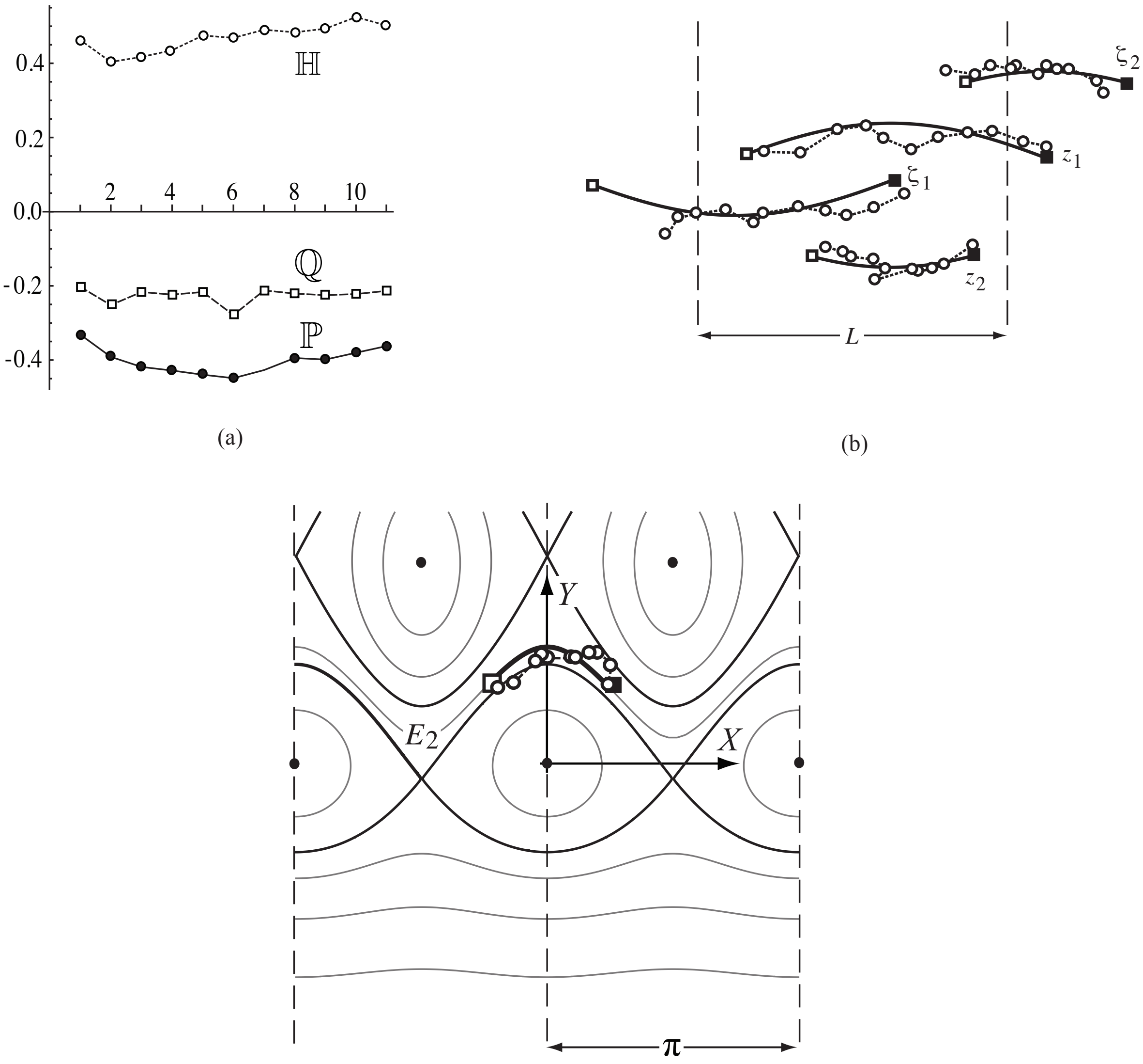

(a)

(b)

(c)

Figure 4.5: Comparison of the point vortex model with the experimental wake III (Fig. 4.1 (c)): (a) Variation of the model constants of motion for the experimental vortex positions. (b) Real-space representation of the experimental data (open circles connected by dashed line) in a co-moving frame ($U = 0$) and the corresponding model trajectories (filled squares and solid lines) obtained by integrating along the level curve indicated in panel (a). Initial positions are marked by the vortex labels. (c) Model phase space representation for $\gamma \approx 0.25$ and $\mathbb{P} = -0.402$. The experimental phase trajectory is marked by open circles joined by dashed line. The model trajectory is marked by filled squares and a heavy line. For both panels (b) and (c), the filled squares mark the starting point of the model trajectory (represented by heavy lines) and the hollow squares mark the end point.

The model is next compared with the experimental wake II (Fig. 4.1 (b)). Here $L = L_e = 1.22$ cm, as estimated from the data. The best-fit analysis gives $\Gamma_1/\Gamma_2 = 2/5$ and thus the scaled values of Γ_1 and Γ_2 are assumed to be $0.40\,\mathrm{cm}^2/\mathrm{s}$ and $1.0\,\mathrm{cm}^2/\mathrm{s}$ respectively. Using the averaged values from the spatial periods, it is possible to obtain $\mathbb{H} \approx 0.263$, $\mathbb{Q} \approx -0.208$ and $\mathbb{P} \approx -0.364$. The experimental (X, Y) phase trajectory belongs to the orbiting O_1 regime and fits well with the level curve for $\mathbb{H} = \mathbb{H}_{avg}$, shown in Fig. 4.4 (c). Further it is seen that $U \approx 1.035\,U_e$ and $\Delta t = 1.305$ units for the best-fit case. Vortex trajectories for the model and the experiment in a co-moving frame are shown in Fig. 4.4 (b) and exhibit a good match. Subsequently Fig. 4.4 (d) compares the model vortex positions with the locations of the experimental vortices, after the imposition of the background flow on to the spatial evolution of the model vortices. The scaling argument in equation (4.1) gives $\Gamma_{BL} \approx 22.5\,\mathrm{cm}^2/\mathrm{s}$ and $\Gamma_{TE} \approx 9\,\mathrm{cm}^2/\mathrm{s}$, which are consistent with the predicted values of $\Gamma_{BL} \approx 46.8\,\mathrm{cm}^2/\mathrm{s}$ and $\Gamma_{TE} \approx 2.91\,\mathrm{cm}^2/\mathrm{s}$ obtained from equations (4.2a) and (4.2b) respectively.

Fig. 4.5 compares the point vortex model with the experimental wake III (Fig. 4.1 (c)). $L = L_e = 1.17$ cm is the period length estimate from the experimental data. The best-fit analysis gives $\Gamma_1/\Gamma_2 = 0.33$ and hence $0.33\,\mathrm{cm}^2/\mathrm{s}$ and $1.0\,\mathrm{cm}^2/\mathrm{s}$ are the assumed scaled values of Γ_1 and Γ_2 respectively. We evaluate $\mathbb{H} \approx 0.469$, $\mathbb{Q} \approx -0.226$ and $\mathbb{P} \approx -0.402$ from the averaged values. The experimental (X, Y) phase trajectory belongs to the exchanging E_2 regime and fits quite well with the level curve for $\mathbb{H} = \mathbb{H}_{avg}$, shown in Fig. 4.5 (c). The best-fit analysis further gives $U \approx 0.99\,U_e$, which is within the estimated error percentage, and $\Delta t = 1.785$ units. Fig. 4.5 (b) compares the model and the experimental wake vortices in a co-moving frame of reference. Scaling in equation (4.1) results in $\Gamma_{BL} \approx 24\,\mathrm{cm}^2/\mathrm{s}$ and $\Gamma_{TE} \approx 8\,\mathrm{cm}^2/\mathrm{s}$. These are consistent with the predicted values of $\Gamma_{BL} \approx 53.5\,\mathrm{cm}^2/\mathrm{s}$ and $\Gamma_{TE} \approx 0.89\,\mathrm{cm}^2/\mathrm{s}$ calculated from equations (4.2a) and (4.2b).

In Fig.4.6 the model has been compared with the experimental wake IV (Fig. 4.1 (d)). From

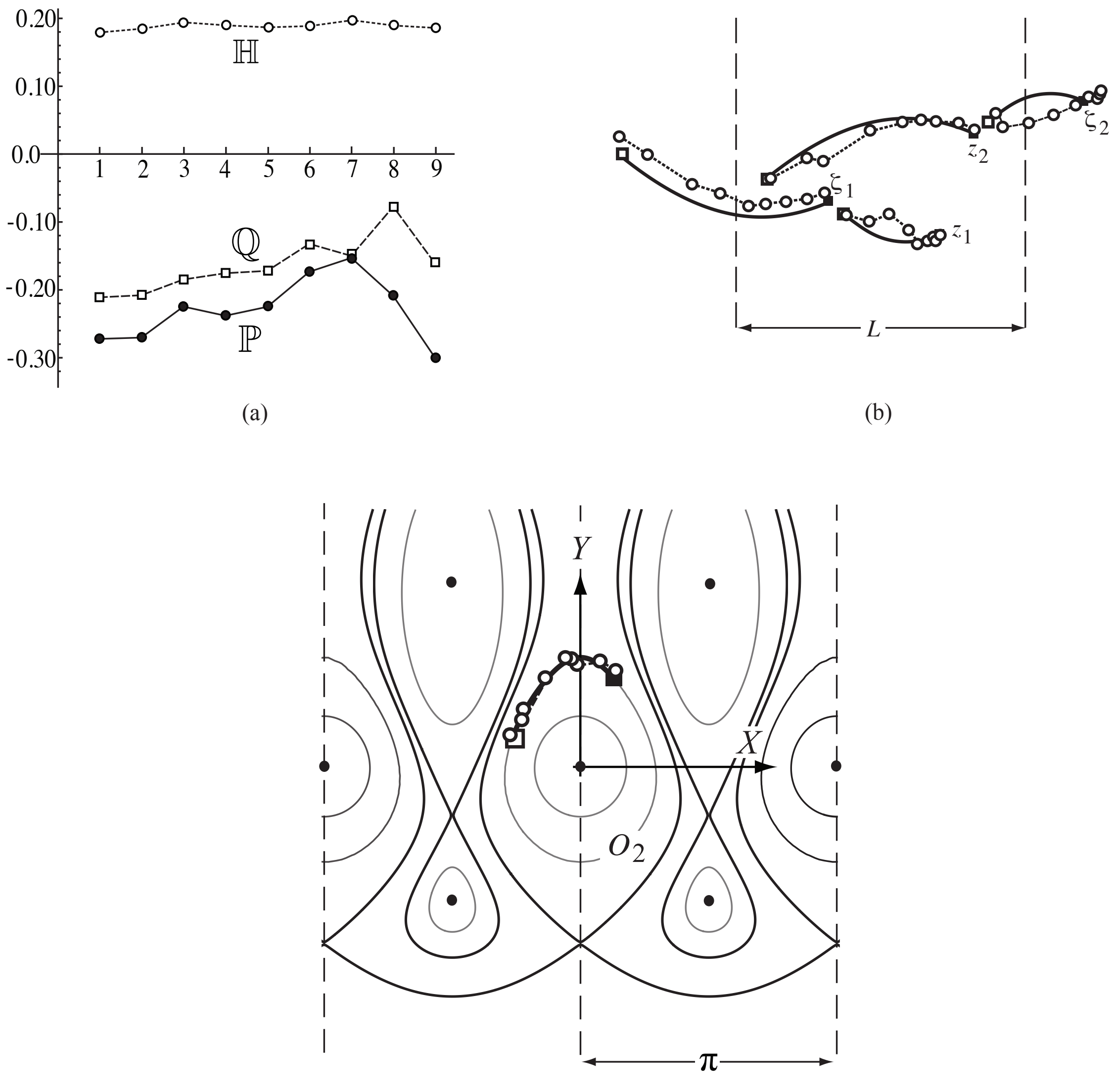

(a)

(b)

(c)

Figure 4.6: Comparison of the point vortex model with the experimental wake IV (Fig. 4.1 (d)): (a) Variation of the model constants of motion for the experimental vortex positions. (b) Real-space representation of the experimental data (open circles connected by dashed line) in a co-moving frame ($U = 0$) and the corresponding model trajectories (filled squares and solid lines) obtained by integrating along the level curve indicated in panel (a). Initial positions are marked by the vortex labels. (c) Model phase space representation for $\gamma \approx 0.32$ and $\mathbb{P} = -0.240$. The experimental phase trajectory is marked by open circles joined by dashed line. The model trajectory is marked by filled squares and a heavy line. For both panels (b) and (c), the filled squares mark the starting point of the model trajectory (represented by heavy lines) and the hollow squares mark the end point.

the experimental data, the period length is estimated to be $L = L_e = 1.01$ cm. The best-fit analysis generates $\Gamma_1/\Gamma_2 = 0.47$ and thus the scaled values of Γ_1 and Γ_2 are assumed to be $0.47\,\text{cm}^2/\text{s}$ and $1.0\,\text{cm}^2/\text{s}$ respectively. Using the averaged values from the spatial periods, we calculate $\mathbb{H} \approx 0.188$, $\mathbb{Q} \approx -0.195$ and $\mathbb{P} \approx -0.240$. The experimental (X, Y) trajectory belongs to the orbiting O_2 regime and fits extremely well with the level curve for $\mathbb{H} = \mathbb{H}_{avg}$, shown in Fig. 4.6 (c). We also obtain $U \approx 1.02\,U_e$ and $\Delta t = 1.205$ units for the best-fit case. Vortex trajectories for the model and the experiment in a co-moving frame are shown in Fig. 4.6 (b) and exhibit a good match. Using the scaling argument in equation (4.1), it can be shown that $\Gamma_{BL} \approx 22\,\text{cm}^2/\text{s}$ and $\Gamma_{TE} \approx 10.5\,\text{cm}^2/\text{s}$, which are consistent with the predicted values of $\Gamma_{BL} \approx 48.69\,\text{cm}^2/\text{s}$ and $\Gamma_{TE} \approx 2.09\,\text{cm}^2/\text{s}$ obtained from equations (4.2a) and (4.2b).

The experimental (X, Y) phase trajectory for the experimental soap film wake V (Fig. 4.1 (e)) is transitional in between the orbiting and the exchanging modes. The existence of this dual nature presents novelty and consequently we perform two separate comparisons of the experimental wake with the point vortex model, assuming orbiting and exchanging motions for the model vortices respectively.

Fig. 4.7 compares the fifth wake assuming orbiting motion. From the averages values of the experimental data, it is found that $L = L_e = 1.16$ cm, and $\mathbb{H} \approx 0.205$, $\mathbb{Q} \approx -0.065$, $\mathbb{P} \approx -0.288$. The best-fit analysis gives $\Gamma_1/\Gamma_2 = 0.78$ and hence the scaled values of Γ_1 and Γ_2 are assumed to be $0.78\,\text{cm}^2/\text{s}$ and $1.0\,\text{cm}^2/\text{s}$ respectively. Further we have $U \approx 0.97\,U_e$, which is within the estimated error percentage, and $\Delta t = 1.79$ units. In this case the phase trajectory is fitted with the orbiting O_2 trajectory corresponding to $\mathbb{H} = \mathbb{H}_{avg}$, as shown in Fig. 4.7 (c). The comparison in the co-moving reference frame is presented in Fig. 4.7 (b) and the fit is satisfactory for a significant downstream wake evolution. The scaling in equation (4.1) gives $\Gamma_{BL} \approx 17.2\,\text{cm}^2/\text{s}$ and $\Gamma_{TE} \approx 13.4\,\text{cm}^2/\text{s}$, which are found to be consistent with

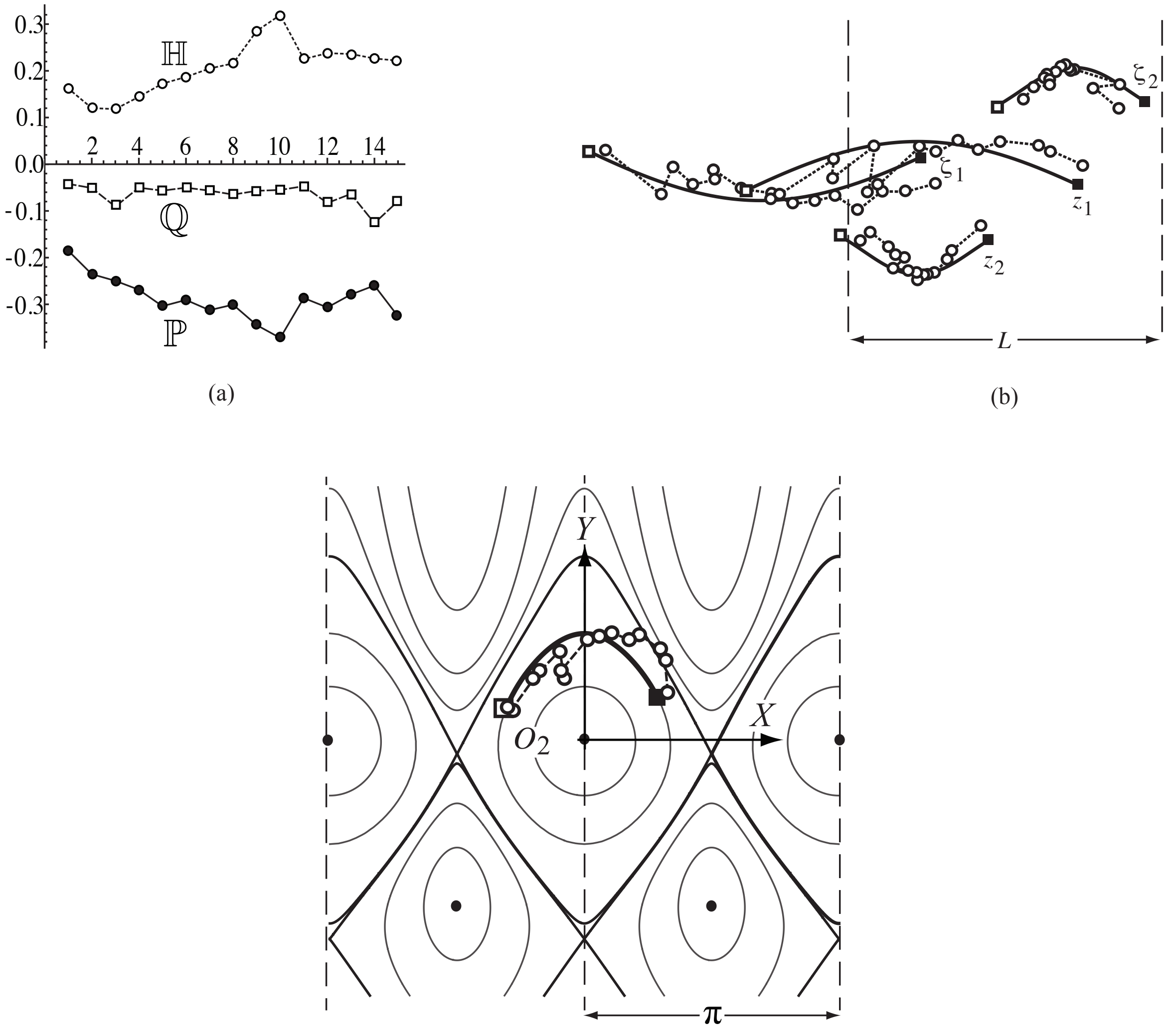

(a)

(b)

(c)

Figure 4.7: **Model regime case I (orbiting mode):** Comparison of the point vortex model with the experimental wake V (Fig. 4.1 (e)): (a) Variation of the model constants of motion for the experimental vortex positions. (b) Real-space representation of the experimental data (open circles connected by dashed line) in a co-moving frame ($U = 0$) and the corresponding model trajectories (filled squares and solid lines) obtained by integrating along the level curve indicated in panel (a). Initial positions are marked by the vortex labels. (c) Model phase space representation for $\gamma \approx 0.44$ and $\mathbb{P} = -0.288$. The experimental phase trajectory is marked by open circles joined by dashed line. The model trajectory is marked by filled squares and a heavy line. For both panels (b) and (c), the filled squares mark the starting point of the model trajectory (represented by heavy lines) and the hollow squares mark the end point.

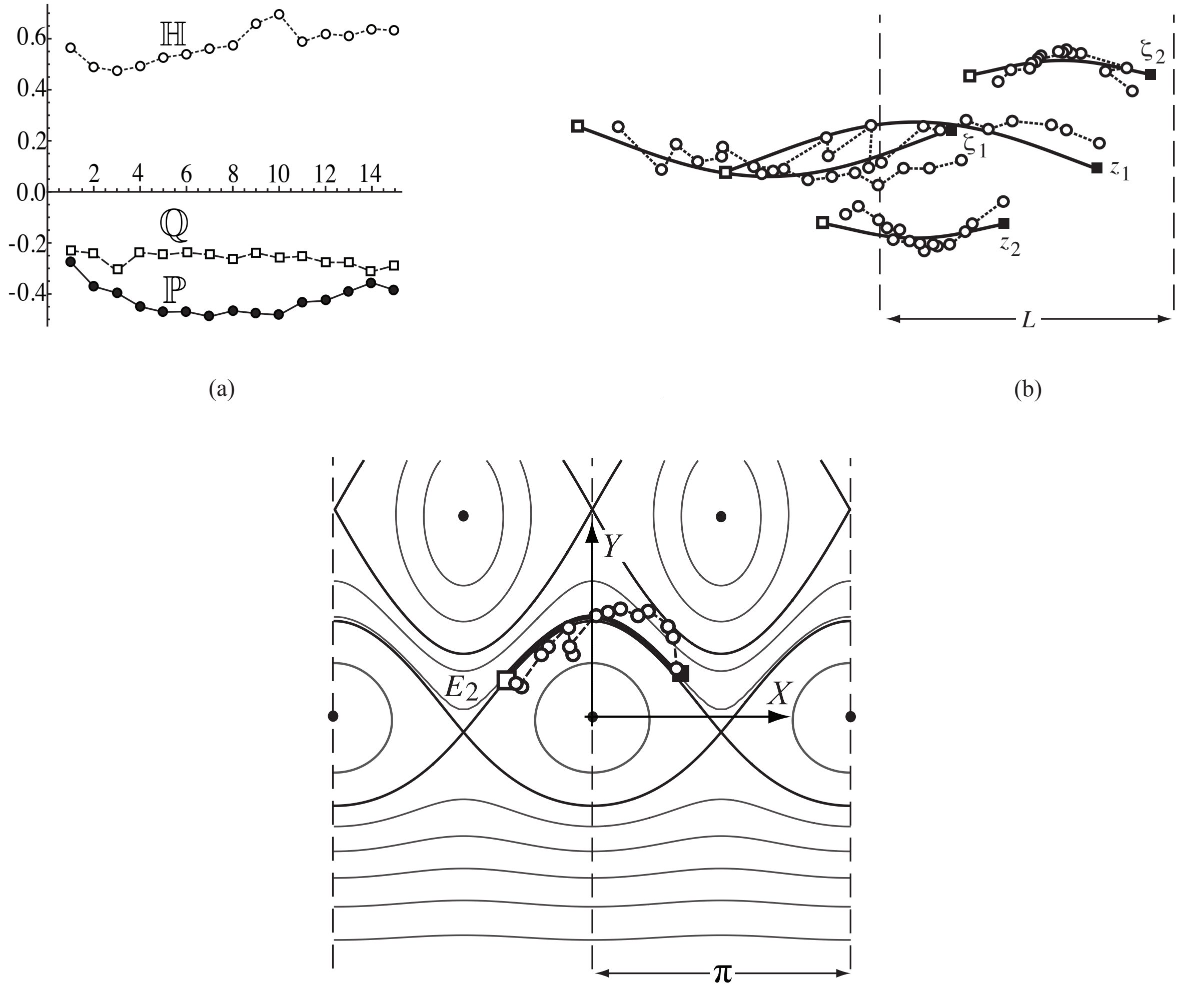

(a)

(b)

(c)

Figure 4.8: **Model regime case II (exchanging mode):** Comparison of the point vortex model with the experimental wake V (Fig. 4.1 (e)): (a) Variation of the model constants of motion for the experimental vortex positions. (b) Real-space representation of the experimental data (open circles connected by dashed line) in a co-moving frame ($U = 0$) and the corresponding model trajectories (filled squares and solid lines) obtained by integrating along the level curve indicated in panel (a). Initial positions are marked by the vortex labels. (c) Model phase space representation for $\gamma \approx 0.23$ and $\mathbb{P} = -0.422$. The experimental phase trajectory is marked by open circles joined by dashed line. The model trajectory is marked by filled squares and a heavy line. For both panels (b) and (c), the filled squares mark the starting point of the model trajectory (represented by heavy lines) and the hollow squares mark the end point.

Table 4.1: Summary of the comparisons of the staggered 2P wake model with experiments

Expt.	$\mathbb{P}$	Model γ	Mode	Motion characteristic
1 (I)	-0.420	0.26	Orbiting (O_1)	Orbiting motion with a large time periodicity.
1 (II)	-0.187	0.45	Mixed (M_2)	Mixed motion (with predominant orbiting characteristics) with a large time periodicity.
2	-0.364	0.29	Orbiting (O_1)	The like-signed base vortices approach each other periodically.
3	-0.402	0.25	Exchanging (E_2)	Typical exchanging motion with bounded transverse separation.
4	-0.240	0.32	Orbiting (O_2)	The like-signed base vortices tend to orbit one another.
5 (I)	-0.288	0.44	Orbiting (O_2)	Transitional location in phase domain. Demonstrates both orbiting and exchanging behaviors.
5 (II)	-0.422	0.23	Exchanging (E_2)	Transitional location in phase domain. Demonstrates both orbiting and exchanging behaviors.

the predicted values of $\Gamma_{BL} \approx 53.64\,\text{cm}^2/\text{s}$ and $\Gamma_{TE} \approx 1.04\,\text{cm}^2/\text{s}$ that have been calculated from equations (4.2a) and (4.2b).

Fig. 4.8 presents the case when the fifth wake is compared with the exchanging E_2 mode type. In this comparison the best-fit analysis generates $\Gamma_1/\Gamma_2 = 0.30$, $U \approx 0.98\,U_e$, $\Delta t = 1.955$ units and the averaged parameter values are $\mathbb{H} \approx 0.578$, $\mathbb{Q} \approx -0.261$ and $\mathbb{P} \approx -0.422$. Fig. 4.7 (b) compares the model and the experimental vortex motions in the co-moving

Table 4.2: Comparison between the averaged experimental and the model values of the horizontal component ($\mathbb{Q}$) of linear impulse

Experiment	Experimental $\mathbb{Q}$	Model $\mathbb{Q}$	Error
1 (I)	-0.266	-0.241	-10.31 %
1 (II)	-0.061	-0.046	-32.61 %
2	-0.208	-0.210	0.95 %
3	-0.226	-0.250	9.60 %
4	-0.195	-0.181	-7.73 %
5 (I)	-0.065	-0.062	-4.84 %
5 (II)	-0.261	-0.269	2.97 %

frame and they match well yet again for a significant downstream. Finally using the scaling in equation (4.1), $\Gamma_{BL} \approx 18.8\,\mathrm{cm}^2/\mathrm{s}$ and $\Gamma_{TE} \approx 5.6\,\mathrm{cm}^2/\mathrm{s}$ are obtained.

Table 4.1 presents a summary of the five model comparisons with the physical experiments. Details of all these five comparisons will follow in [36]. Parts of this work can also be sourced in [32], [33], and [34].

Finally, using equations (2.7) and (3.6), it is possible to theorize the following from the model for the non-dimensionalized horizontal component of linear impulse:

$$\mathbb{Q} = \gamma - \frac{1}{2}. \tag{4.3}$$

Table 4.2 demonstrates the comparison between the model and experimental values of $\mathbb{Q}$.

The error, as a percentage measure, is calculated as follows:

$$E = \frac{\mathbb{Q}_{model} - \mathbb{Q}_{experiment}}{\mathbb{Q}_{model}} \times 100, \tag{4.4}$$

where $\mathbb{Q}_{model}$ is the model value of $\mathbb{Q}$ obtained from equation (4.3), $\mathbb{Q}_{experiment}$ is the experimental value of $\mathbb{Q}$ obtained from using the averaged experimental data-set on the vortex locations from the multiples periods and the model-predicted γ from the discussed fitting procedure. and E is the corresponding error percentage on the $\mathbb{Q}$ measure. The mean error range magnitude of less than ~ 10 % further serves as a validation for the model results.

Chapter 5

Mathematical modeling of three vortex wakes

As discussed in the preceding chapters, when the motion of a bluff body relative to a surrounding fluid consists of a net translation plus a superimposed oscillation, the resulting wake often consists of more isolated vortices than is found in the standard Kármán street. These so-called 'exotic' vortex wakes [37], in which three or more vortices are generated during each oscillation of the body, have been observed in numerous situations, from oscillating cylinders [2] to swimming fish larvae [16] and flapping wings [38], and are known to occur over a fairly broad range of oscillation amplitude and frequency [39].

The case of $N = 3$ vortices (P+S mode) in a periodic strip produces substantially more complicated dynamics than taking say, $N = 2$. Fig. 1.2(c) shows a typical three vortex wake in a periodic domain. There do exist numerous examples of relative equilibrium configurations [40], but most initial conditions lead to relative motion of the vortices. When the sum of the vortex strengths is zero, the dynamics can be reduced to an integrable Hamiltonian system. This problem was considered in detail by [20], who gave a full classification of the dynamics.

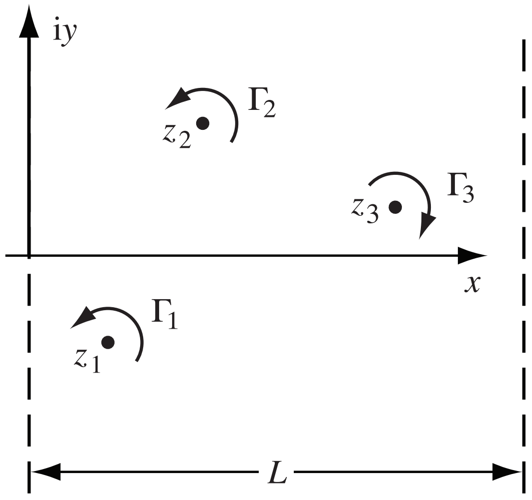

(a)

Figure 5.1: Notation used in the model point vortex system for $N = 3$ vortices per period.

In §5.1, this model is generalized to allow for variations in the relative vortex strengths while still maintaining the spatial symmetry. The details of this work are available in [6].

5.1 Equations for three vortices in a periodic domain

Consider the two-dimensional potential flow produced by periodic arrangements of $N = 3$ point vortices having real-valued strengths Γ_α with $\alpha = 1, 2, 3$. The labeling of the vortices is chosen such that $|\Gamma_1| \le |\Gamma_2| \le |\Gamma_3|$, and the assumption is $0 \le \Gamma_1 \le \Gamma_2$ without any loss of generality. The individual circulations remain constant in this model, so clearly the sum of the vortex strengths,

$$S_1 = \sum_{\alpha=1}^{N} \Gamma_\alpha, \tag{5.1}$$

is a constant of the motion. Since the discussion is motivated by periodic shedding from a bluff body, it is assumed that $S_1 = 0$ in every case considered here.

The treatment, like in the previous chapters, will again be in terms of the dimensionless vortex strength $\gamma = \Gamma_1/\mathbb{S}$, where $\mathbb{S} = \Gamma_1 + \Gamma_2$. It is assumed that this $\mathbb{S} \neq 0$. Now, owing to the considered ordering of the vortex strengths,

$$0 \leq \gamma \leq 1/2. \tag{5.2}$$

The dynamics of three point vortices in a singly periodic domain is integrable when $S_1 = 0$ [20]. In this case, $\mathbb{S} = -\Gamma_3$ (> 0), and the vortex strength ratios can all be given in terms of γ.[1] The choice of $S_1 = 0$ and conservation of linear impulse allows one to write all vortex separations in terms of Z, giving

$$\pi(z_2 - z_3)/L = -\gamma\, Z + \Xi, \tag{5.3a}$$

$$\pi(z_3 - z_1)/L = -(1-\gamma)\, Z - \Xi, \tag{5.3b}$$

where Ξ is defined as the (dimensionless) linear impulse in the form

$$\Xi = \frac{\pi}{L\mathbb{S}} \sum_{\alpha=1}^{N} \Gamma_\alpha\, z_\alpha. \tag{5.4}$$

Combining the equations of motion for vortices 1 and 2 from 1.3b with the expressions for the vortex separations in 2.4 and 5.3 gives

$$\frac{\mathrm{d}Z^*}{\mathrm{d}\tau} = \frac{1}{2\pi\mathrm{i}}\left\{\cot\big(Z\big) - \cot\big(\gamma\, Z - \Xi\big) - \cot\Big[(1-\gamma)Z + \Xi\Big]\right\}, \tag{5.5}$$

where the dimensionless time variable is defined as follows,

$$\tau = \big(\pi^2\mathbb{S}\big)\, t/L^2. \tag{5.6}$$

---

[1] Note that the labeling of the vortices and the definitions of γ, Z, and Ξ differ slightly from that used in [20].

This reduced system can itself be written in (dimensionless) Hamiltonian form with

$$\mathbb{H}(Z;\gamma,\Xi) = \frac{-1}{2\pi}\left\{\ln\left|\sin(Z)\right| - \frac{1}{\gamma}\ln\left|\sin\bigl(\gamma\, Z - \Xi\bigr)\right| - \frac{1}{1-\gamma}\ln\left|\sin\Bigl[(1-\gamma)Z + \Xi\Bigr]\right|\right\}. \quad (5.7)$$

The reduced Hamiltonian system, or phase space representation, can be interpreted as describing the motion of a passive particle in the velocity field produced by a set of vortices in stationary equilibrium. To arrive at this interpretation, note that the three terms in 5.5 (or 5.7) have spatial periods of π, π/γ, and $\pi/(1-\gamma)$, respectively. If $\gamma = p/q$ is rational, with p and q being positive integers and $q \geq 2p$, then these three periods are commensurate with period $m_1\pi$ when

$$m_1 = m_2\; q/p = m_3\; q/(q-p) \qquad m_i \in \mathbb{N},$$

which is satisfied by taking $m_1 = q$, $m_2 = p$, and $m_3 = q - p$. By employing the identity

$$\cot\left(\frac{\pi z}{L}\right) = \frac{1}{M}\sum_{m=0}^{M-1}\cot\left[\frac{\pi}{ML}(z - mL)\right], \quad (5.8)$$

the equation of motion for Z can be written as

$$\frac{\mathrm{d}Z^*}{\mathrm{d}\tau} = \frac{1}{2(q\pi)\mathrm{i}}\left\{\sum_{m=0}^{q-1}\cot\left[\frac{1}{q}\bigl(Z - m\pi\bigr)\right] - \frac{1}{\gamma}\sum_{m=0}^{p-1}\cot\left[\frac{1}{q}\left(Z - \frac{\Xi + m\pi}{\gamma}\right)\right]\right.$$
$$\left. - \frac{1}{1-\gamma}\sum_{m=0}^{q-p-1}\cot\left[\frac{1}{q}\left(Z + \frac{\Xi - m\pi}{1-\gamma}\right)\right]\right\}. \quad (5.9)$$

That is, Z gives the position of a passive particle being advected by three rows of point vortices in a periodic strip of width $q\pi$: q vortices with strength 1 at positions $m\pi$, $m = 0, 1, \ldots, q-1$; p vortices with strength $1/\gamma$ at positions $(\Xi + m\pi)/\gamma$, $m = 0, 1, \ldots, p-1$; and $q-p$ vortices with strength $1/(1-\gamma)$ at positions $(-\Xi + m\pi)/(1-\gamma)$, $m = 0, 1, \ldots, q-p$. If γ is irrational, then the phase space can still be viewed as three parallel rows of point vortices in stationary equilibrium. However, the spacing in each of these rows is incommensurate with that in the other rows, and the phase space consists of the entire complex plane.

For a comprehensive exploration of the dynamics governed by 5.9, see [20]. In 5.2 we apply this model to the specific conditions corresponding to the image in 1.2(a).

The Hamiltonian given in 5.7 and 5.9 satisfies the canonical equations of motion

$$\frac{\mathrm{d}X}{\mathrm{d}t} = \frac{\partial \mathbb{H}}{\partial Y}, \qquad \frac{\mathrm{d}Y}{\mathrm{d}t} = -\frac{\partial \mathbb{H}}{\partial X}. \tag{5.10}$$

Similar to the previous analysis, for given values of γ and Ξ, an initial vortex separation Z corresponds to a unique level curve of $\mathbb{H}$ in the (X, Y) phase space.

Note that $\mathbb{H}(Z; \gamma, \Xi)$ in 5.7 is invariant under the transformation $\{Z \to Z^*, \ \Xi \to \Xi^*\}$. In general (i.e., unless $\mathbb{P} = 0$), the phase space representation is not symmetric about the X axis, so that changing the sign of $\mathbb{P}$ (without changing the sign of Y) corresponds to a reflection of the phase space curves about the X axis. Changing the sign of $\mathbb{P}$ is equivalent to changing the signs of all the point vortices, which reverses the direction of the phase space trajectories and the direction of net vortex translation in physical space.

5.2 Comparison with experiment

The experimental vortex locations are determined from Fig. 1.2(a) by assuming that they are centered on the circular regions seen in the images. In the case of the 2P wake, the model assumes symmetry about the x-axis, so we rotate the experimental image (slightly) to maximize the vortex symmetry about the horizontal axis. For the P+S wake there is no symmetry axis, and thus we assume that the photograph is oriented parallel to the background flow.

Temporal evolution of the experimental vortices are extracted from the instantaneous spatial positions by assuming that the vortex generation is exactly periodic in time, so that the N vortices immediately after the body appear at the subsequent downstream spatial positions at times $t = i/f_e$ for $i = 1, 2, \ldots$, where f_e is the experimentally observed shedding frequency. We then translate each spatially-distributed cluster of N vortices a distance $\pm i\, U_e/f_e$ for $i = 0, 1, 2, \ldots$, where U_e is the speed of the bluff body relative to the background flow. For the experiment in 1.2(a), U_e/f_e is estimated from the wavelength of the cylinder path; for the experiment in 1.2(b), U_e is estimated from the speed of the background flow and f_e from the flapping frequency.

The model description requires specification of the various parameter values. The assumed spatial period, L, is obtained from a given image by averaging the separations between neighboring clusters of experimental vortices. The appropriate values for the remaining parameters depend on the choice of vortex strengths, which includes an assumption of vortex labels due to our restriction on the value of γ in 5.2. The labels and the value of γ based on the two-stage 'best fit' analysis (described in details in Chapter 4.2). The experimental estimate of the linear impulse, Ξ_e, is determined by substituting the assumed strengths and experimental positions into equation (5.4). The experimental estimate of the Hamiltonian, $\mathbb{H}_e$, is determined by substitution into equation (5.7). In general, since the system is dissipative, the values of Ξ_e and $\mathbb{H}_e$ will depend on which experimental vortices are used in the calculation.

The vortex strengths are determinedby fitting a phase space model trajectory to the experimental data. The experimental phase space trajectory is found by evaluating Z in 2.4 for each cluster of N experimental vortices. For a given value of γ, specifying $\Xi = \Xi_e$ generates a unique phase space model representation, and specifying $\mathbb{H} = \mathbb{H}_e$ identifies a unique level curve in that phase space.[2] The initial and final positions on the model phase space trajectory are taken to be the points on the model curve that are closest to the initial and final experimental positions, respectively. The 'best fit' value of γ is chosen to be the value that minimizes the mean squared error between the model phase space trajectory and the experimental phase space trajectory.

For the the P+S wake in 1.2(a), the first step of our fitting procedure finds that $\gamma \approx 0.26$. For simplicity, we assume that $\gamma = 1/4$, or $\Gamma_1 : \Gamma_2 : \Gamma_3 = 1 : 3 : -4$, which enables us to examine the full phase space in a periodic strip of width 4π. Interestingly, $\gamma = 1/4$ is the same value found by[20] via trial and error. Using this value of γ, we determine Ξ_e and $\mathbb{H}_e$ based on the initial locations of the $N = 3$ vortices, as was done in [20]. These assumptions yield the phase space representation shown in 5.2(a). Taking the experimental phase space positions to be the correct values, the model positions give a root mean square (RMS) error of 0.131; this value has been normalized by the strip width, L. For comparison, taking $\gamma = 0.26$ gives a normalized RMS error of 0.128.

The phase space representation in 5.2(a) contains 8 fixed vortices in a periodic strip of width 4π, as described in 5.1. There are also 8 stagnation points in the domain, and the level curves of $\mathbb{H}$ that join the stagnation points divide the phase space into several qualitatively different *regimes of motion*. Model vortex trajectories from within a single regime of motion all display the same qualitative behavior. For a detailed discussion of regimes of motion and bifurcations in phase space structure for the $N = 3$ case, see [20]. The experimental phase space trajectory is well represented by the best fit model trajectory, which lies in the very thin regime of motion that winds around seven of the eight fixed vortices. The large extent of the curve corresponds to vortices 1 and 2 experiencing significant relative separation in both the streamwise and spanwise directions during their motion. Note, however, that if

---

[2] It should be noted here that the modeling approach allows only for consideration of constant values of Ξ and $\mathbb{H}$ for any particular case.

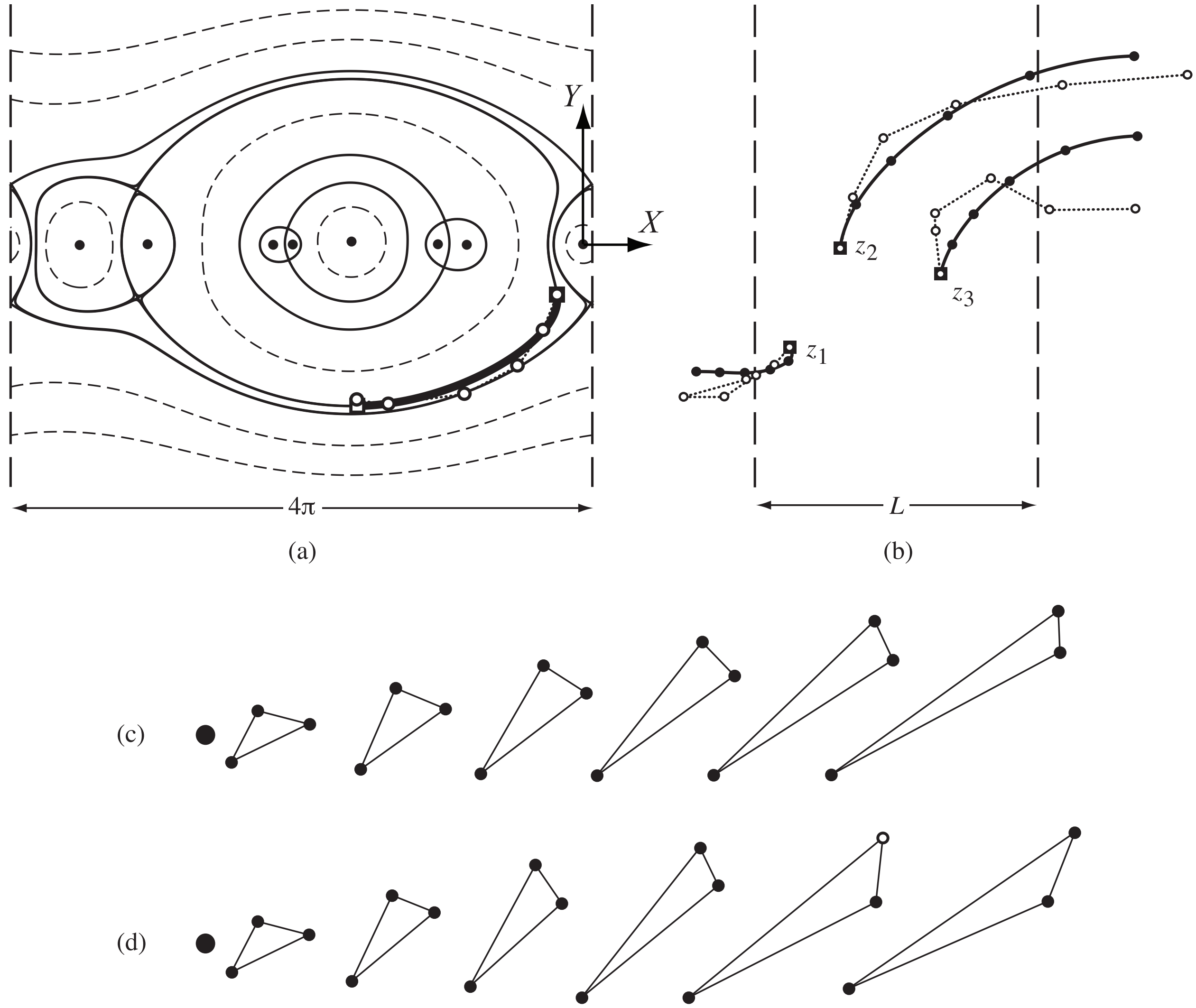

Figure 5.2: Comparison of the $N = 3$ model with the P+S wake from Fig. 1.2(a). (a) Phase space representation for $\gamma = 1/4$ and $\Xi = -1.253 + \mathrm{i}\,0.011$. Stationary phase-space vortices, or stable fixed points, are marked with solid circles. Separatrices, or level curves of $\mathbb{H}$ that join the unstable fixed points, are shown with solid lines; other representative level curves of $\mathbb{H}$ are shown with dashed lines. Experimental phase space positions are shown with open circles and connected with a dotted line. The corresponding model trajectory, for which $\mathbb{H} = -0.032$, is shown with a heavy solid line; the initial and final positions on this trajectory are shown with a solid square and an open square, respectively. The first experimental point coincides exactly with the initial model position. (b) Vortex trajectories in the model frame of reference, for which the fluid velocity goes to zero as $y \to \pm\infty$. Experimental positions transformed with $c = 0.76$ are shown with open circles and are connected with dotted lines to show the time sequence. Model trajectories are shown with solid lines, squares mark the initial positions, and solid circles mark the remaining model vortex locations at the periodic times corresponding to the experimental locations. (c) Stroboscopic images of the model vortex positions in the laboratory frame of reference. Vortices in the same cluster are joined by solid lines. (d) Estimates of the experimental vortex locations in 1.2(a). The open circle marks an estimated location for the vortex that is difficult to identify.

the experimental vortex motion were to continue following the model prediction, the relative vortex separation would be bounded, and the vortices would eventually return to their initial relative configuration.

The model phase space trajectory leads directly, though numerical integration, to the motion of the model vortices in a frame of reference for which the fluid is at rest far from the vortices, as shown in 5.2(b) for the $N = 3$ case. The second step in our fitting procedure (transformation of the instantaneous experimental vortex positions into approximated time-dependent motion by shifting each spatially-distributed cluster of N vortices a distance $\pm i\,U/f$). The estimated wavelength of the vorticity production, U_e/f_e, does not account for expected spatial variations in background velocity or uncertainty in the measured values. Thus we set $U/f = c\,U_e/f_e$ and choose the value of c to minimize the mean squared error between the model and experimental vortex locations in the model frame. For the P+S case, taking $c = 0.76$ gives the transformed experimental trajectories shown in 5.2(b). The resulting RMS error in the normalized real-space vortex positions in the co-moving frame is 0.126.

Chapter 6

Physical applications of vortex wake analysis

6.1 On a mechanism of energy extraction from vortex-induced vibrations

Riverine and oceanic movements of water, in particular the tides and currents existing in the coastal and offshore environments, offer tremendous potential in terms of clean, renewable and ubiquitous power generation. The presently conceived mechanism utilizes new understanding of vortex-induced vibrations to extract mechanical energy from these natural movements of water. Global net energy flux from surface and under-water currents has been estimated to be at 280 trillion watt-hours and the discussed design presents a compact, transportable, maintenance-free, and cost-efficient means of harnessing power from such sources. This section discusses a method for extraction of mechanical energy from a fluid motion, which can subsequently be employed to generate useable electrical energy.

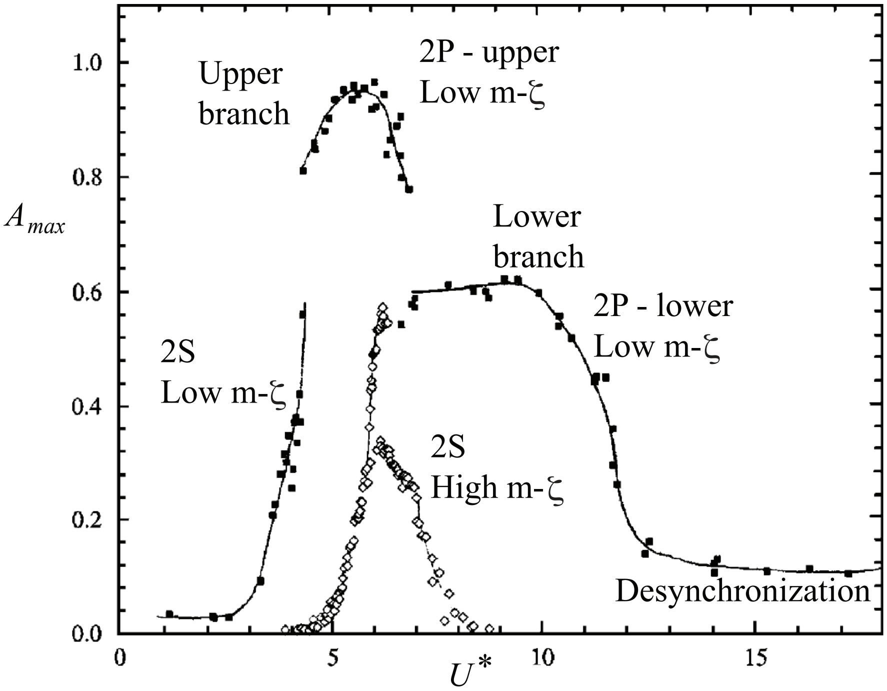

Figure 6.1: Amplitude of body vibration effected by shed vortices reaches a peak during the 2P mode generation. Peak oscillation amplitude A_{max}, normalized relative to the cylinder (bluff body) diameter D, is plotted as a function of U^* which is the flow speed normalized by the system frequency. Here ζ is the system damping coefficient. The plot is reproduced from [7].

6.1.1 Operating principles

Vortex Induced Vibration (VIV) is a well-known phenomenon. When a cylindrical object is placed in a moving fluid, vorticity generated in the object's boundary layer is shed into the downstream wake. This vortex shedding typically alternates from one side of the object to the other, modulating the pressure distribution, thus inducing oscillatory lift on the cylinder that results in vibrations orthogonal to the flow direction. Harvesting the kinetic energy available in these flow-induced high-amplitude oscillations typically requires converting the linear translation to rotary motion of a power generator shaft.

Typical cylinder wakes exhibit the classical alternating vortex street (known as the von Kármán

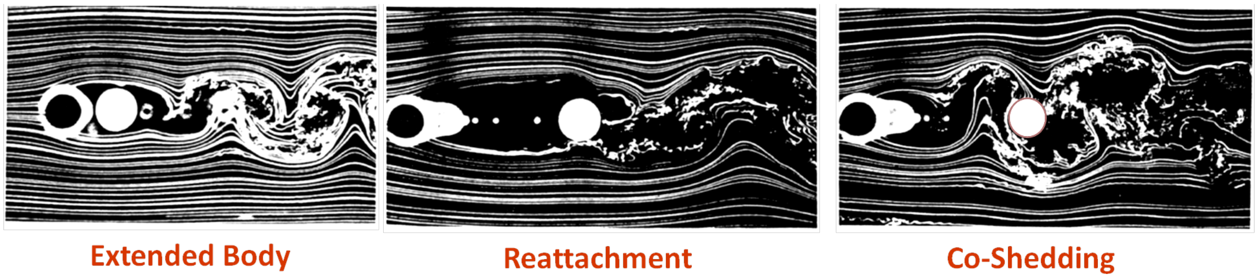

Figure 6.2: *Galloping* phenomenon [8] resulting from the interaction of multiple wakes shed into the flow by multible bluff bodies (one fixed cylinder and one oscillating cylinder).

wake or ‘2S’ mode). Achieving significant vibrations from the 2S mode requires synchronization of the wake with the natural frequency of the structure, thus restricting energy harvesting to very specific flow speeds. This restricted response is the situation commonly familiar from aeroelasticity. However, under conditions such as those produced in coastal waters, oscillating cylinders can produce a ‘2P’ mode wake. In comparison to the common 2S mode, the 2P mode can lead to very large amplitude oscillations that do not depend on the structural frequency, enabling it to be present over a wide range of flow speeds. Numerous experimental observations (see [7], [41]) validate that when a bluff object is submerged in a flow, its amplitude of vortex-induced vibrations attains a peak when the mode of the shed wake belongs to the 2P regime. Fig. 6.1 depicts this phenomenon with the upper branch (representing larger amplitudes) corresponding to 2P wake formation. A larger displacement of the bluff body implies the possibility of extracting more mechanical energy from the system. Through appropriate power conversion mechanisms, the extracted mechanical energy can subsequently be transformed into useful electrical energy. The energy-harvesting potential of this phenomenon remains largely untapped because basic understanding of 2P mode wakes has developed only within the past decade and current harvester designs fail to fully exploit these phenomena.

Turbines are the standard approach for extracting energy from moving flows. However, according to the reports [42] from the Electric Power Research Institute (EPRI), the turbines are not financially viable for flow speeds less than approximately 3 m/s, while most marine currents are slower than 1.5 m/s and most rivers are slower than 1 m/s. VIVACE is the current state-of-the-art water-based energy harvesting system (see [43], [44], and [45]) for typical marine and river applications. The design discussed in this section significantly advances the concepts intially developed by the VIVACE system, by improving upon various major system components and a broader range of applicability and utility.

The new VIV-based energy harvester design, to be discussed in §6.1.2, targets flow speeds of 0.4 - 1.0 m/s, which are more common in off-shore marine and river currents. The primary focus of this project is to leverage the breakthroughs in the understanding of 2P wakes by optimizing the design components such that the wake shed corresponds to a 2P regime (thereby ensuring maximized body vibrations). Additinally, the design also makes use of the unique phenomenon of *galloping* (see Fig. 6.2) which refers to an enhanced body motion owing to the interference of wakes shed by multiple closely spaced bluff objects in the flow. In essence, the design thus includes two closely placed cylinders to generate this galloping effect.

6.1.2 Design of the energy harvester

As per [7], [41], the largest amplitudes of bluff body oscillation that can be expected to be forced by vortex wake-induced forces (oscillating pressures) are in the range 0.6 - 1.4 times the characteristic diameter of the cylindrical bluff body. The current design parameters are so obtained that it can reach the maximum amplitude i.e. $1.2D$ (displacement to an extremum location from the two-cylinder in-tandem orientation with respect to the oncoming flow direction), where D is the diameter of the oscillating cylinder.

Refer to Fig. 6.4(b) for a top view of the design. It consists of 2 cylinders. The lower

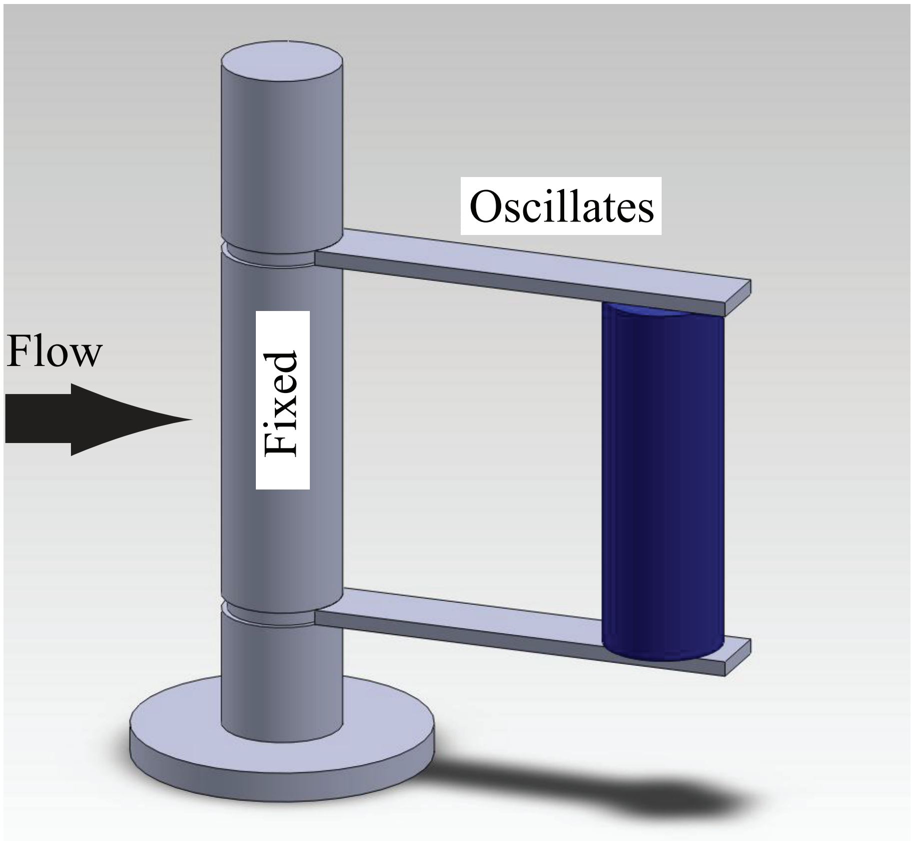

Figure 6.3: Engineering model of the vortex-induced vibration based energy harvester. It consists of one fixed cylinder and one freely oscillating cylinder. The free oscillations of the later are effected by the wake-induced forces. This moving cylinder is attached to a shaft (via support arms) to a shaft that centrally runs through the front cylinder. The motion is thus transmitted to the shaft and through gear transformation this oscillatory motion is converted to unidirectional rotational motion which can then power up a generator. An engineering diagram with more details of the design follows in Fig. 6.6. The vertical orientation of the design will permit mass ratios less than one and will leverage wake interactions. This pictorial representation is a snapshot from the SolidWorks model.

cylinder (or, the front cylinder) is fixed and the flow strikes it first. There is an oscillating outer cylinder which is connected to the front fixed cylinder. The vibration of this second cylinder is because of the combined effects of the wake shed by the front cylinder and from the oscillating pressure generated by the vortex structures shed by itself.

Fig. 6.4(a) shows the general angular displacement of the oscillating cylinder assuming it

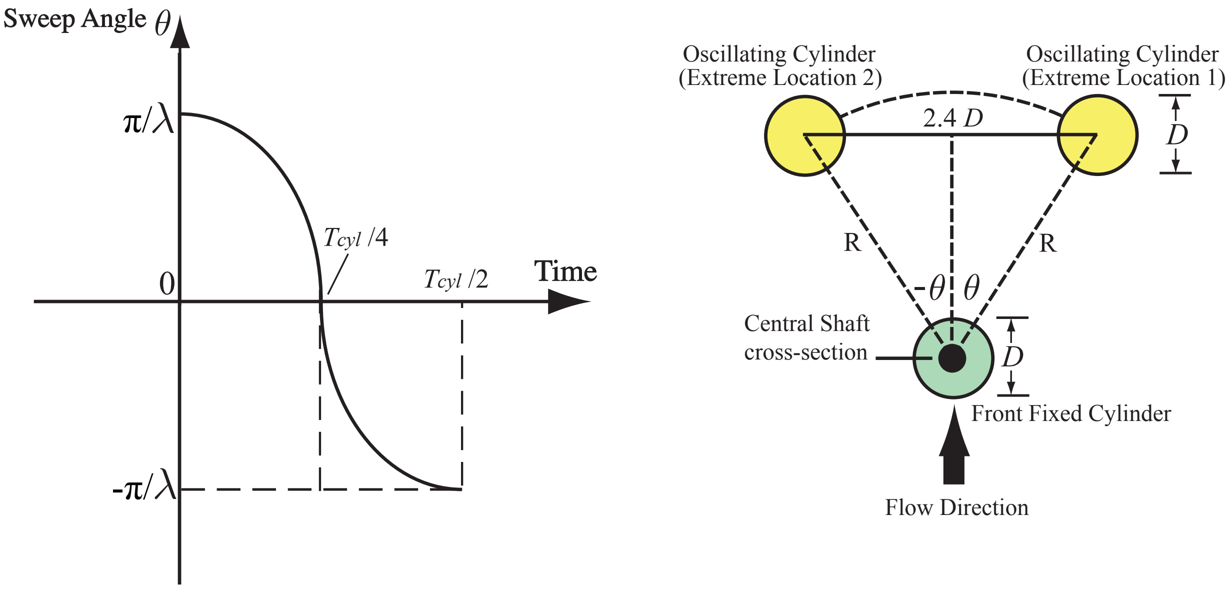

(a) (b)

Figure 6.4: (a) Variation of the angular displacement of the oscillating cylinder from the in-tandem orientation when the oscillating cylinder and the fixed cylinder are in the same line as the flow direction. The angular variation is assumed to be sinusoidally periodic. (b) Top view of the two cylinder harvester design with the assumed peak-to-peak vibration amplitude being $2.4D$, where D is the diameter of both the cylinders in the design.

is at extreme location 1 at time = 0 (as marked in Fig. 6.4(b)). The sweep angle range is $[-\theta, \theta]$ and the in-tandem orientation marks the $\theta = 0$ transition. The angular variation is assumed to be sinusoidally periodic.

Now, suppose that the range of oscillation is $[-\pi/\lambda, \pi/\lambda]$, where $\lambda \in I$ and is greater than 2. The last consideration is to galvanise the estimate by not considering the more ambitious oscillation range where the oscillating cylinder sweeps through 180 °.

From the assumed sinuisoidal angular change, the sweep angle can be written as a functional variation of time (t) in the form

$$\theta = \frac{\pi}{\lambda} \sin\left[\left(\frac{4t}{T_{cyl}} + 1\right)\frac{\pi}{2}\right], \tag{6.1}$$

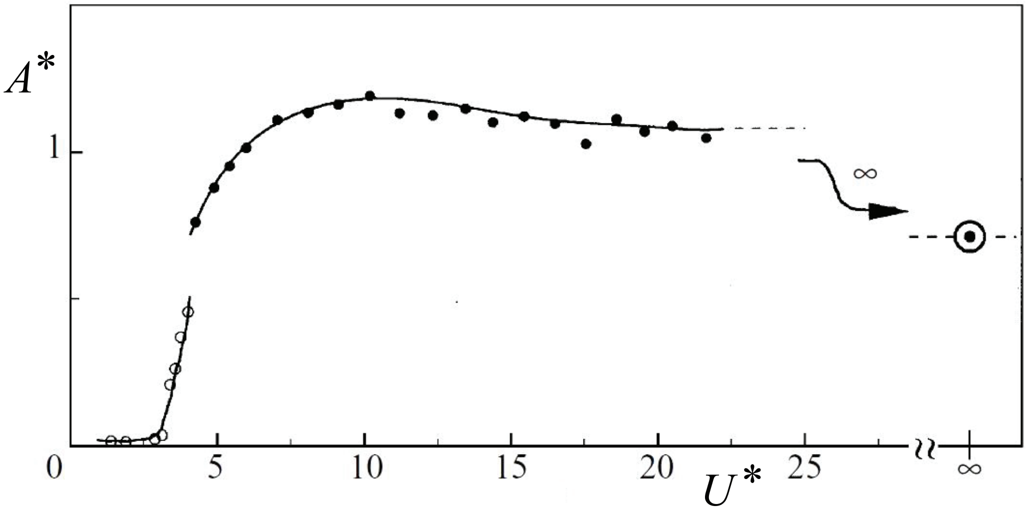

Figure 6.5: When the relative mass is very low, the amplitude response ($A^* = A/D$) is essentially uniform across a wide range of U^* which is the flow velocity normalized with respect to system frequency. The plot is reproduced from [9].

where T_{cyl} is the oscillation period of the outer cylinder. It is to be also noted that from geometry considerations, the angle θ can be expressed in terms of the cylinder diameter D (both the cylinders are of equal diameter) and R which is the center-to-center distance of the overhanging arm between the two cylinders (see Fig. 6.4(b)),

$$\theta = \sin^{-1}\left(1.2\,\frac{D}{R}\right). \tag{6.2}$$

Thus, by taking a time-derivative of equation (6.1), the angular acceleration turns out to be

$$\dot{\theta} = \frac{2\pi^2}{\lambda T_{cyl}}\cos\left[\left(\frac{4t}{T_{cyl}}+1\right)\frac{\pi}{2}\right], \tag{6.3}$$

Let C_{harn} (N.s/m) be the linear viscous damping coefficieny added for energy harnessing. Following the techniques of [45], the formulation for the harnessed power can then be written

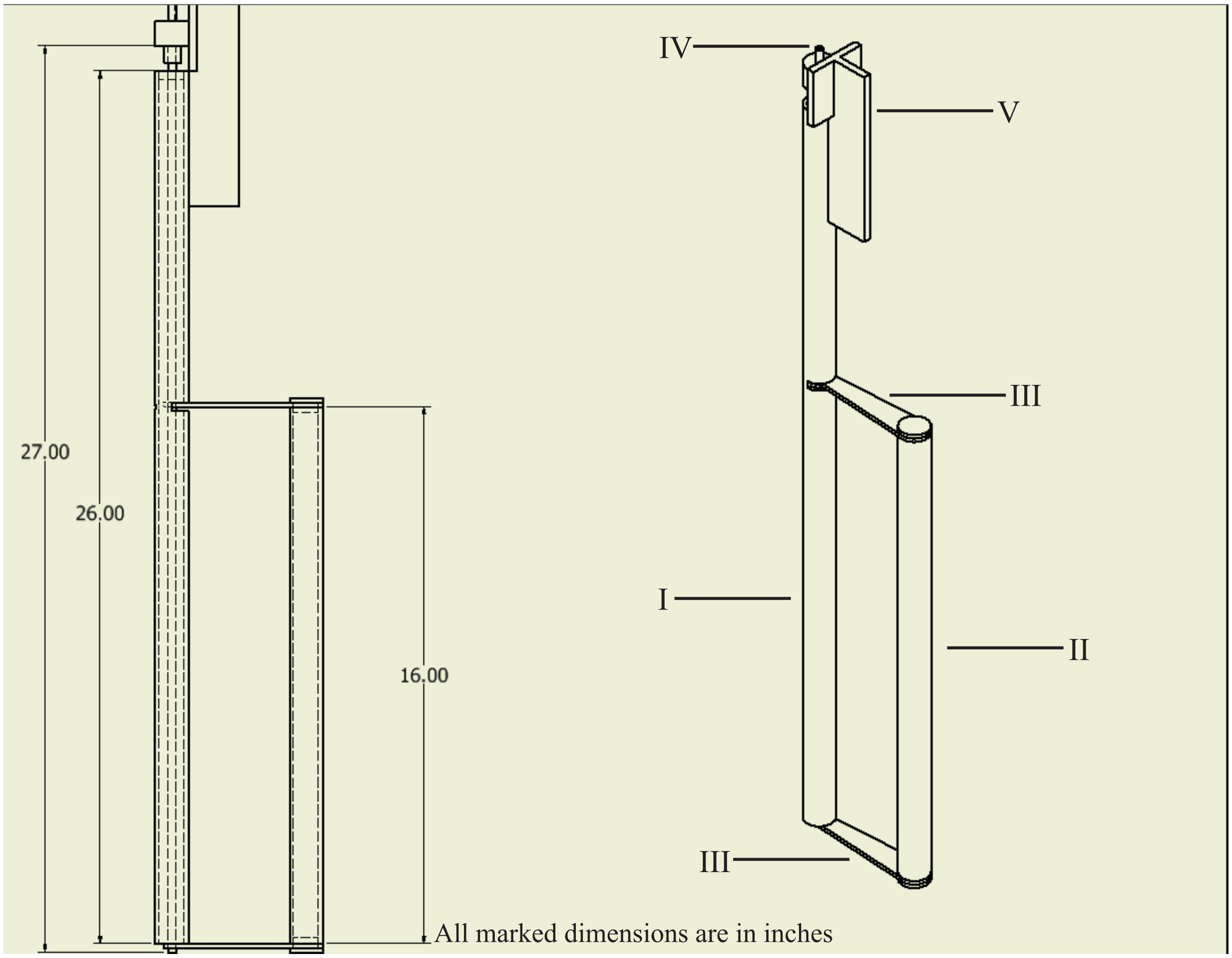

All marked dimensions are in inches

(a) (b)

Figure 6.6: Engineering sketch of the VIV-based energy harvester. In (b), the component **I** is the fixed front cylinder which the oncoming flow first strikes, the component **II** is the oscillating rear cylinder, componenets **III** are the arm-supports which connects the trailing oscillating cylinder to the central drive shaft (component **IV**) passing through the fixed front cylinder, and the component **V** shows the bracket support for installing the power conversion mechanisms like the generator. The shaft (component **IV**) is free to rotate by use of ball bearings and it transmits the motion of the outer cylinder to a gear transformer (installed on the bracket) which converts the alternating motion into uni-directional rotational motion that can power a generator. *Image courtesy: Gary Nave (Graduate Student, Engineering Science and Mechanics, Virginia Tech).*

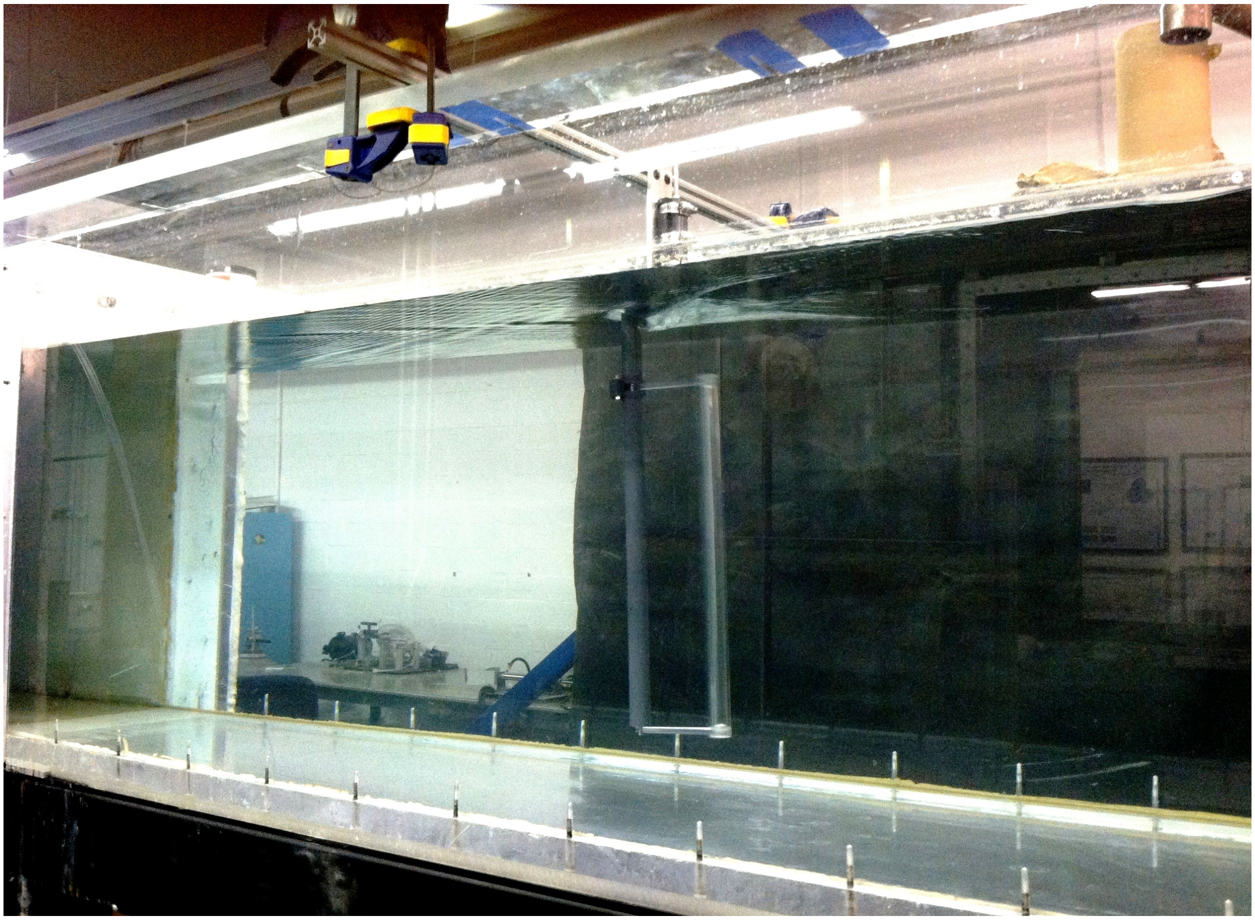

Figure 6.7: The VIV-based energy harvesting mechanism operating in a water tunnel flow. Flow rate of water ≈ 0.45 m/s.

as,

$$P_{harn} = \frac{1}{T_{cyl}} \int_{0}^{T_{cyl}} C_{harn} \left(R\dot{\theta}\right)^2 dt, \tag{6.4}$$

Putting in the information on angular acceleration from equation (6.3), the harnessed power attains the form,

$$P_{harn} = \frac{2}{\lambda^2} \frac{\pi^4 R^2 C_{harn}}{T_{cyl}^2}. \tag{6.5}$$

Through observation of the vibration amplitude, the extremum values (say, θ_{max}) of the sweep angle can be calculated using equation (6.2). The time period (T_{cyl}) also can be measured during the experiments. These data coupled with the other system parameters give the estimation for the harnessed power using equation (6.5).

An interesting step of the design process as to what should be the optimum cylinder diameters still remains. The natural frequency of the system has been estimated to approximately $f_n = 3.90$ Hertz. Fig. 6.5 is used next to identify the cylinder dimensions. $U^* = 8.0$ is targetted to ensure a large enough vibration amplitude (where U^* is the flow velocity that has been normalized with respect to the system frequency) . Now, let U be the flow velocity and as a working value, it is assumed to be 0.70 m/s which is a common current speed off the coasts of Virginia, USA. Therefore, we have

$$U^* = \frac{U}{f_n D}, \tag{6.6a}$$

whereby,

$$D = \frac{U}{f_n U^*} = 2.25\, cm \approx 0.89\, inch. \tag{6.6b}$$

For ease of fabrication, the cylinder diameter is preliminarily taken to be 1 inch. As a first trial, the overhanging arm-length R was chosen to be $4D$. Fig. 6.3 represents the pre-fabrication envisioned model and Fig. 6.6 shows the corresponding engineering sketches. All the concerned components are also marked and their functions are discussed in the caption of Fig. 6.6. Preliminary experiments have been performed with the first prototype and Fig. 6.7 presents a snapshot of the working setup. Work will continue at Virginia Tech to optimize the energy extraction device with targets of commercial deployment.

6.2 Fluid-structure interactions: soap film wakes

Coupled motions of the solid body in the flow field and the shed vortices frequently give rise to complex interaction phenomena. Prediction of the dynamics of the body owing to the body-vortex interactions is of fundamental importance. In his lectures, Arnold Sommerfield once observed, "Kármán's real aim in his investigation of the vortex street was to establish an analytic drag formula". The Kármán's drag law [46] is as follows:

$$\tilde{D} = \frac{\rho\Gamma b}{\tau} + \frac{\rho\Gamma^2}{2\pi h}\left(1 - \frac{\pi b}{h}\tanh\frac{\pi b}{h}\right), \tag{6.7}$$

where $\tilde{D}$ is the drag force (averaged over a time interval τ, which is the period of the Eulerian flow field in the wake), Γ is the individual vortex circulation magnitude in the two rows of vortices, ρ is the fluid density, a is the streamwise offset of the alternating vortices, b is the transverse separation of the two rows of vortices, and h is the vortex-to-vortex spacing within a row of identical periodic vortices along the wake. Following the same inspiration, comprehension of the relationship between the "wake signature" of a flow and the motion of the body that generates such a wake will constitute a key component of this thesis.

The Kármán model, however, assumes a periodic wake with vortex patterns that repeat downstream (this is a case of *relative equilibrium* with the shape and size of the wake configuration always staying invariant as it evolves in the streamwise direction). Therefore, this is the main point of contrast between the Kármán vortex street and any other vortex-dominated exotic wake, like the 2P or P+S regimes. For these, there would typically be an evolution of the vortex locations from periodic strip to periodic strip as the pattern progresses downstream. This requires a novelty in approach while trying to explore the dynamic response that such a wake can induce on the structure.

Viscous effects are concentrated in the boundary layers surrounding the solid body. The vortex shedding involves a roll-up of these boundary layers along the edges of the body. However, despite this predominant role of viscosity in the formation of the vortical structures, the viscous forces acting on the structure can be ignored as a good first approximation. This paves the way for the use of a potential flow model involving point vortices. The strength of the shed vortex is adjusted so as to ensure that it cancels the singularity being generated at the shedding location on the solid body. This is necessary to satisfy the regularity condition of finite fluid velocity at the shedding corners. The model, designated in literature [47] as the unsteady point vortex method, assumes that the intensity of a shed vortex (Brown-Michael vortices [48]) increases monotonically to reach an extremum; subsequent to which it has a steady intensity and a new unsteady vortex is shed into the flow. Thus, this model looks at the flow domain surrounding the body and the vortices there, which exert a direct influence on the structure during their shedding process. It is, however, to be noted here that the effects of the remainder of the sheet is neglected in this unsteady point vortex model.

The (steady) point vortex model proposed in Chapter 3 considers the evolving dynamics of the vortices in the mid-wake region and assumes that the individual vortex strengths remain invariant as they propagate downstream. An important next step in terms of continuing work from this thesis is to combine the knowledge about the mid-wake dynamics with the near-body effects explorable from the unsteady point vortex model [47].

Quantitative comparison between the model results and the vortex dynamics observed in the experimental wakes substantiates the point vortex model (see Chapter 4). Although a flowing soap film is relatively more complex compared to an incompressible Newtonian flow [49], still “soap film systems” [50] have been often used to perform experiments that enforce the essentially two-dimensional wake behavior. As mentioned previously, the soap-film experiments, discussed hitherto in the preceding sections, have been performed by a collaborator group led by Dr. Anders Andersen at the Technical University of Denmark

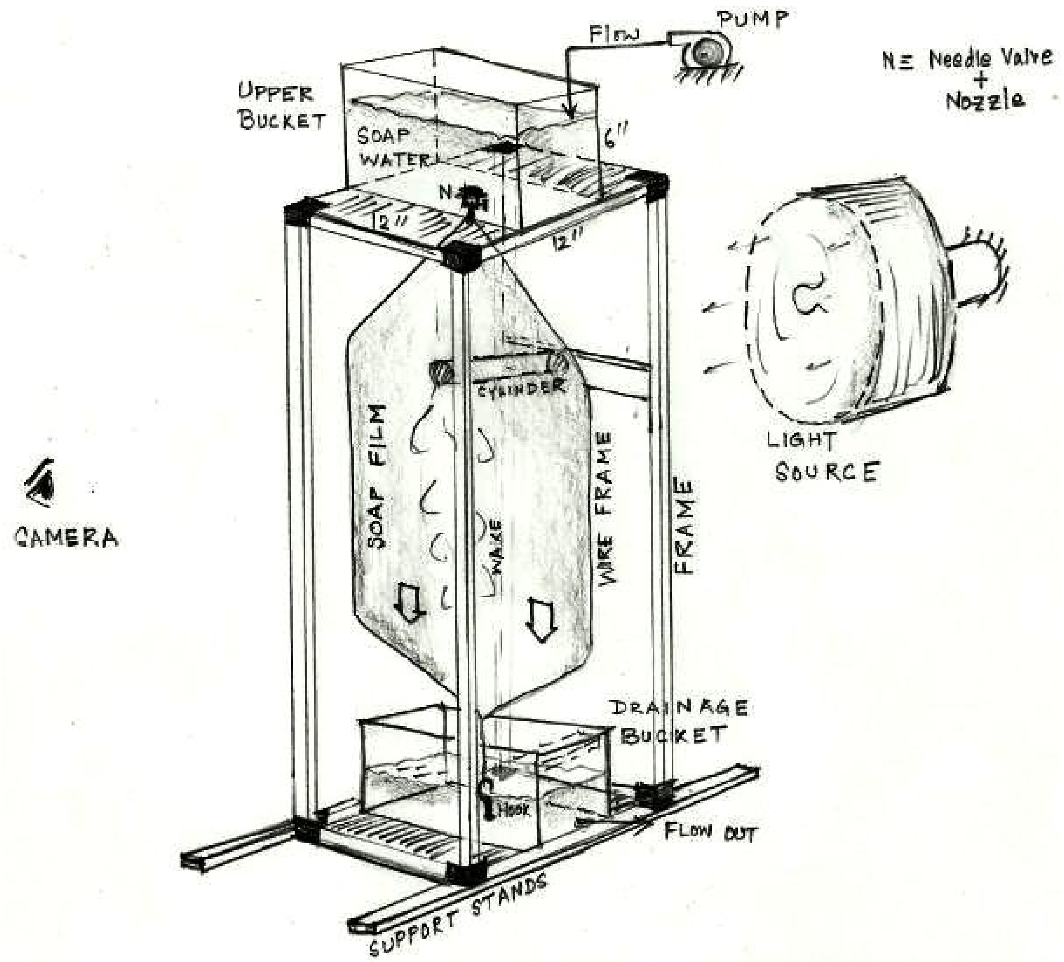

Figure 6.8: An artistic rendering of the experimental set-up generating wakes in flowing soap films flowing under pressure head (maintained by an overhead reservoir). Artistic rendering is done by the author.

(DTU). The investigated wakes are formed by forced oscillations of a rigid foil on a vertically flowing soap film. Simple harmonic pitching oscillations are imparted to the symmetric foil and it penetrates the test section perpendicularly. Scaled comparisons of the model with these experiments demonstrate a good match and hence allow for a prediction of the trajectories and intensities of the individual vortices.

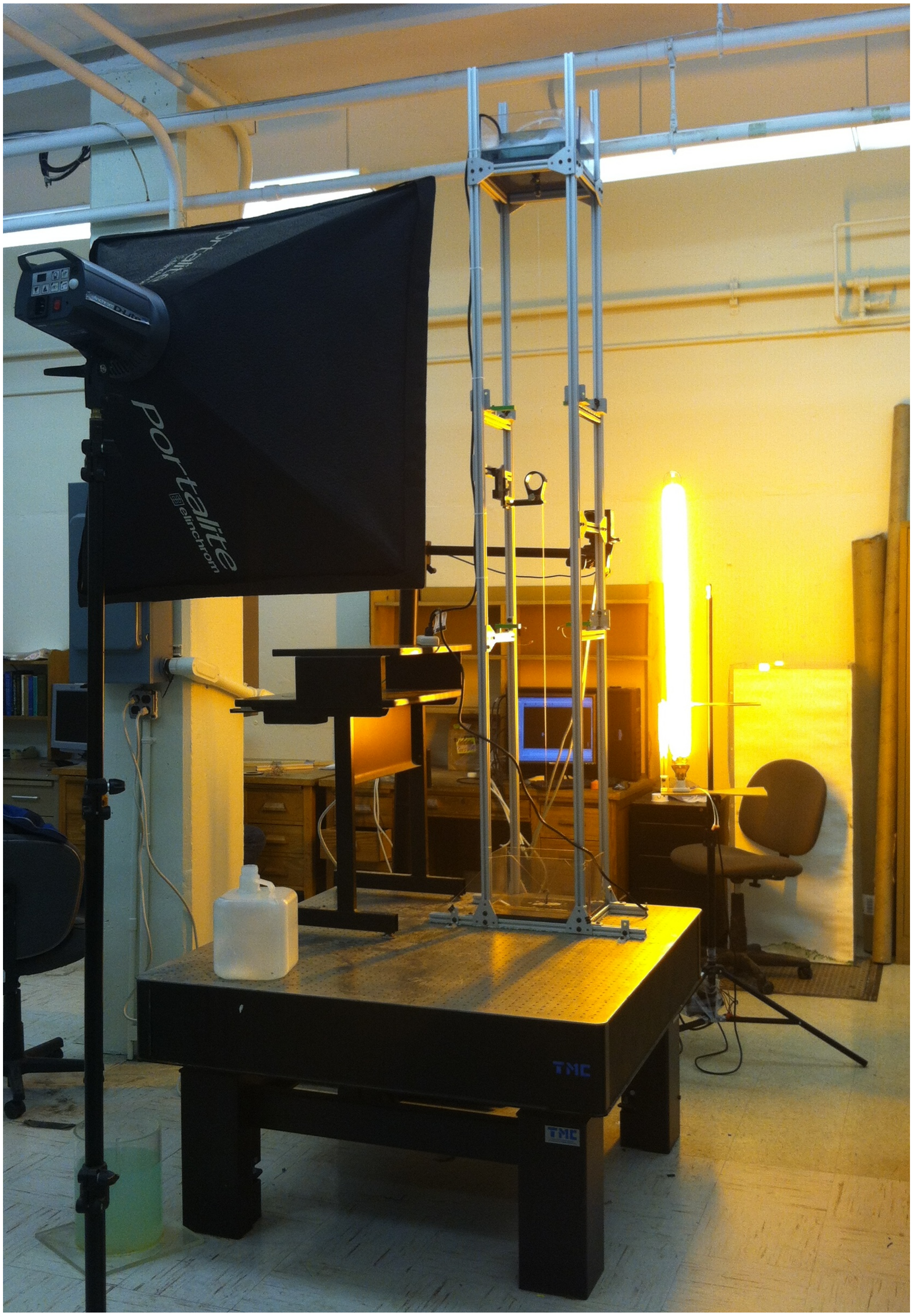

Figure 6.9: Developed experimental setup. A constant pressure head is maintained in the top container and the vertically flowing film will be held by plastic fish wires. The light source which is currently in use is a sodium lamp (yellow, monochromatic) of 180 Watt intensity.

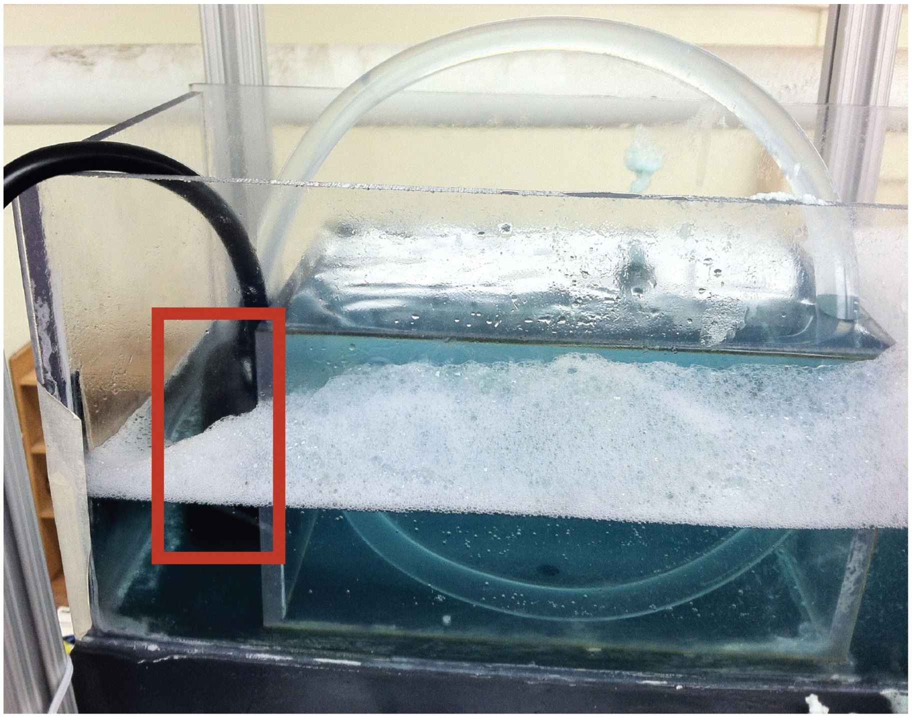

Figure 6.10: Mechanism fabricated to ensure a constant pressure head. Location: top reservoir at an elevation in the experimental setup. The pump which maintains the constant head is marked in red.

6.2.1 Design of the setup and prelimary experiments

Wake shedding experiments involving free motion of bluff bodies on soap film flows have been performed. Fig. 6.11 presents the preliminary experimental snapshots. Figs. 6.8 and 6.9 portray the general plan of the experimental set-up. It involves a gravity-driven, vertically flowing soap film which functions as almost a two-dimensional flow. An overflow mechanism at the top reservoir (see Fig. 6.10) ensures a constant pressure head at the nozzle exit and the planar film, held between two thin plastic wires, flows vertically down. The soap water concentration used is 1.5 % by volume. Owing to the air drag the flow attains a terminal velocity, and in the test section, the flowing film can be considered to have a uniform free stream velocity profile and a constant thickness. Typical background velocities are expected to be approximately 150 cm/s. The soap film is illuminated from the rear by

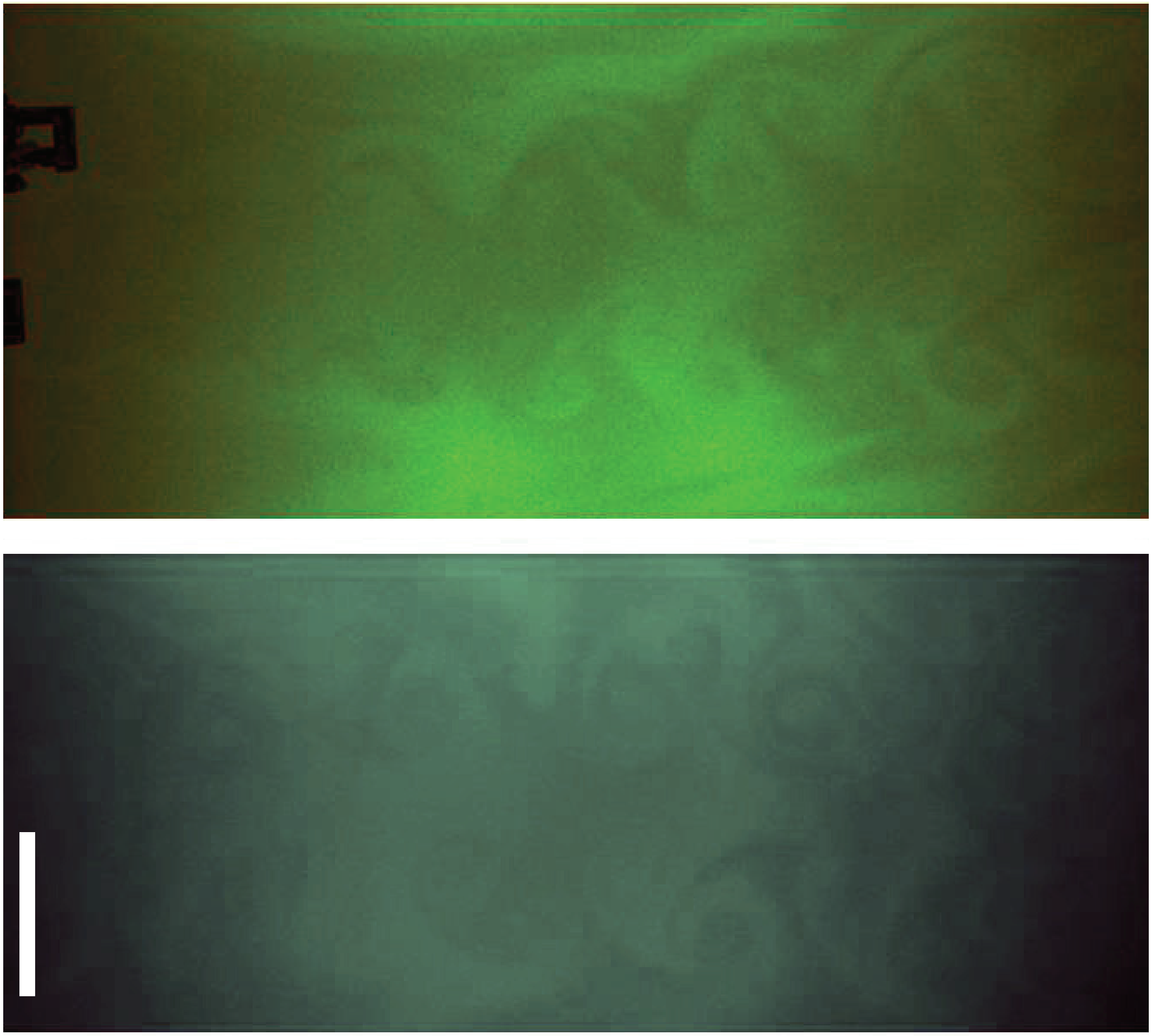

Figure 6.11: Preliminary representative soap film wake experiments with two staggered circular section cylinders acting as bluff bodies. The frame rate of the camera capture is 30 fps. The light source used is a 16 Watt monochromatic, green sodium lamp. The snapshots have been edited on Photoshop to facilitate the visualization of the vortex structures. Scaling: vertical dimension of the white rectangle ≈ 20 mm.

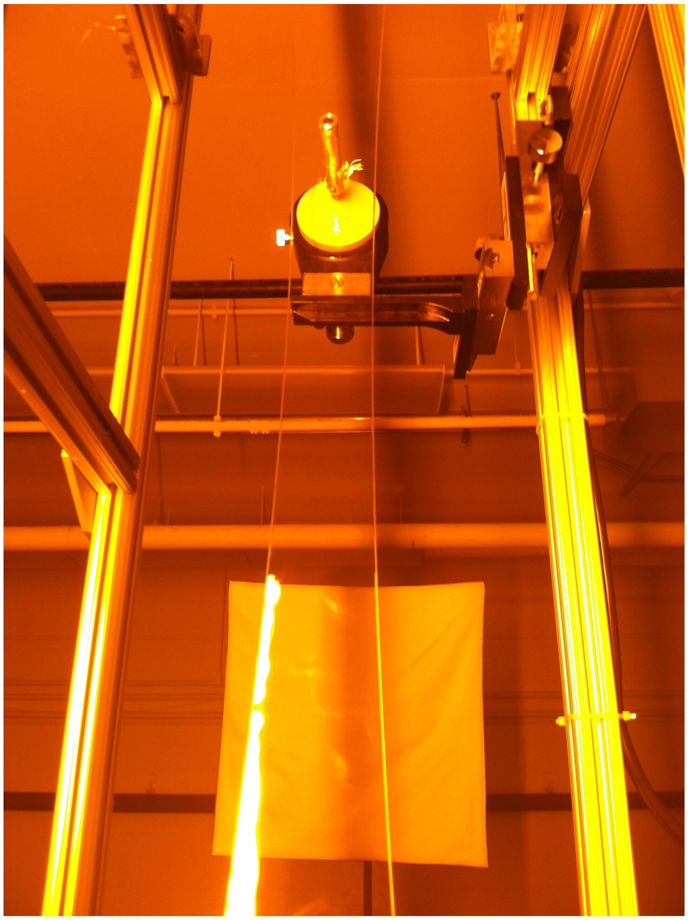

Figure 6.12: Soap film formation on a wire frame (the vertical flow is gravity-controlled). For this particular representation, the bluff body piercing the film section is a fixed circular cylinder.

a monochromatic light source. This is essential to ensure the distinct visualization of the vortex cores through the interference fringes formed by light reflecting from the two film surfaces. Stability of the soap film has been a key issue while performing the experiments and it has been surmised that adding glycerol to the soap water solution can prevent the film from breaking apart.

The primary motive for setting up this experimental setup is to, in future, validate body motion data (free motion under wake-induced forces) with the model predictions. The experiments, therefore, look at *freely* oscillating bluff bodies and the resultant wakes. Free oscillation necessitates that the fluid forces from the flow are dominant on the structure. In the case of soap film, this can be achieved by immersing a thin circular ring (or, disk) in the flow, held by a tethered mechanism. The frequency-amplitude response data for free oscillations in soap film in relation to the different wake modes can be obtained from critical observation of the experimental parameters and the wake patterns. Continuing work will focus on obtaining more rigorous data on these aspects.

Chapter 7

Summary

Complex as well as simple vortex-dominated wakes are observable in a wide variety of flow systems across a broad range of Reynolds numbers. The vortices can have an appreciable effect on the object shedding them and on other objects that are in the flow field and interact with the wake system. In this respect, the structure and dynamics of the wake are crucial. The areas of application are varied, ranging from atmospheric flows to insect flights and even fish propulsion. Some typical examples would be the established engineering systems, as for instance tethered structures in oceans [51], bridges and heat exchangers; and emerging systems like biomimetic or bio-inspired micro-air vehicles [52]. Advances in the comprehension and analysis of the complex vortex-dominated wakes of bluff bodies have played a pivotal role in the progress of many of the engineering sciences.

However, Theodore von Kármánś vortex street model [10, 11, 12] for the 2S mode (with two counter-rotating staggered vortcies per cycle), developed in 1911-12, is even to this day the most important theoretical framework for studying and predicting the dynamics and effects of vortex wakes. So, the frequent occurence of complex exotic wakes makes it fundamentally significant to set up a more robust model to study these various types of wake structures.

This thesis investigates some of the most commonly prevalent complex wake arrangements [13]. In particular, mathematical models have been developed for vortex wakes with four vortices and three vortices per cycle of wake shedding. The four vortex wake belongs to the 2P regime and has two vortex pairs in each period. Generally, each of the vortex pairs consists of two counter-rotating vortices. It should, however, be noted that there are cases in which the pairing vortices have the same circulation sign and the vortices tend to orbit one another. This configuration is termed the 2C mode [17], indicative of the presence of the co-rotating pairs. Through the mathematical developments in this thesis, it has been implicitly assumed that this 2C mode is a special case in a more general definition of 2P wakes, comprising all bluff body wakes with periodic release of four vortices into the flow domain. In the 2P regime, however, the two pairs of vortices can arranged symmetrically or staggered about the centreline of the wake. Both the geometries have been studied in this thesis. The thesis explores, in details, the dynamics of such wakes using a reduced order[1] two-dimensional potential flow model consisting of four vortices with strengths $\pm\Gamma_1$, $\pm\Gamma_2$ arranged symmetrically and antisymmetrically in a periodic strip. It is to be noted here that it has been long known through experimental observations [53] that the paired vortices in a 2P wake often have unequal magnitudes. Thus, the inequality of the vortex intensities in a vortex pair makes the treatment closer to reality and generalizes the model from [29]. Assumption of a spatial periodicity, based on the arrangement of the vortices in the experimental wakes, yields an integrable Hamiltonian dynamical system. The dynamic modes exhibited in the model are classified using a bifurcation analysis of the phase space topology consisting of the level curves of Hamiltonian. Wakes shed from oscillating airfoils

---

[1] The model reduction essentially entails three steps, namely, (a) going down from the *Navier-Stokes equations* to the *Euler equations* through non-consideration of the viscosity effects and eventually to following the vortex cores or the coherent vortex structures in the flow domain, (b) approximating the vortex cores to be represented by point vortices with concentrated vorticities at points, and (c) using the orientational symmetry in the experimentally observed wakes to impose spatial constraints on the point vortex model leading to a two-dimensional phase space representation of the resultant relative vortex motion.

on flowing soap film compare satisfactorily with the predictions generated from the model. Finally, similar reduced order modeling techniques (as applied to mathematize the 2P regime) have been used to develop a model for the P+S mode wakes, with three vortices in each shedding cycle. Model results have been compared satisfactorily with an experimental wake and the observations match well with results in literature.

The thesis finally delves into some possible areas of application of vortex wake analysis. It has introduced a mechanism of clean, renewable, and ubiquitous energy extraction from riverine and marine flows using vortex-induced vibrations of bluff bodies. Vortex shedding from bluff bodies typically alternates from one side of the object to the other, modulating the pressure distribution and causing the object to oscillate orthogonal to the flow direction. The flow velocities targetted for this project are beyond the lower limit of the operational range of the currently established hydrokinectic energy harvesters. Preliminary validative experiments have been performed by placing the designed energy harvester in laboratory-scale water tunnel flows. The specifics of the design so as to optimize the energy extraction capabilities of the device forms a part of this thesis work. It is to be noted here that 2P regime corresponds to a peak in the vibration amplitude of the bluff body shedding the wake and hence the design primarily endeavors to utilize this phenomenon (as a larger displcement field implies the potential of a larger magnitude of available mechanical energy which can be extracted from the flow) along with the concept of *galloping*. The latter is a common physical phenomenon involving enhanced body vibration owing to the interaction of vortex wakes shed from multiple bodies. Finally, the thesis describes another experimental setup that has been fabricated to observe vortex wake formations in gravity-driven laminar soap film flows with an eventual target of exploring free vortex-induced motion. The motive is to correlate the body dynamics with the "signature" of the wake. The design of the experiment includes a vertically oriented soap film flowing down under constant pressure head. The flow occurs through a wired network with bluff bodies piercing the flow or embedded on the film. Bright monochromatic light illuminates the film and the interference fringes formed by reflecting light from the two film surfaces facilitate the identification of the vortex cores.

Hence, the **INTELLECTUAL MERIT** of the present thesis includes a more complete understanding of complicated wake geometries, with special emphasis on systems with four vortices in each period; this being one of the predominantly occurring wake configurations. The key problems, that have been addressed, can be summarized as follows:

1. Systemic exploration and characterization of the dynamic modes belonging to the 2P regime of vortex wakes.
2. Applying the same reduced order modeling methods to study the dynamics of P+S mode wakes.
3. Validation of the modeling framework and the model predictions through comparisons with wakes generated during physical experiments.
4. A better understanding of the effects exerted by the dynamics and structure of complex vortex-dominated wakes on the vibration response of the bluff body and exploration of the possible applications.

The **BROADER IMPACTS** of this treatise will hence include enabling advances for a deeper insight into richness of vortex wake dynamics. This, in turn, has the potential to shed light on the propulsive mechanisms involving wake shedding and would lead to a better working knowledge of forces exerted on the structure by the wake vortices in a flow field. The thesis also explores some important and useful applications based on vortex-induced vibrations. Currently, designs of real engineering systems, whether for suppressing vortex-induced vibrations or for utilizing them, are primarily based on the theoretical framework of the von Kármán model. The current research broadens the state of the art by relating the complex “wake signature” of a flow and the corresponding motion of the body generating that wake.

Bibliography

[1] T. Schnipper, A. Andersen, and T. Bohr. Vortex wakes of a flapping foil. *Journal of Fluid Mechanics*, 633:411–423, August 2009.

[2] C. H. K. Williamson and A. Roshko. Vortex formation in the wake of an oscillating cylinder. *Journal of Fluids and Structures*, 2:355–381, 1988.

[3] Anders Andersen, Tomas Bohr, and Teis Schnipper. Separation vortices and pattern formation. *Theoretical and Computational Fluid Dynamics*, 24(1-4):329–334, March 2010.

[4] M. Fayed, R. Portaro, Amy-Lee Gunter, H. A. Abderrahmane, and Hoi Dick Ng. Visualization of flow patterns past various objects in two-dimensional flow using soap film. *Physics of Fluids*, 23(9):091104, 2011.

[5] A. Andersen, T. Bohr, and T. Schnipper. Separation vortices and pattern formation. *Theoretical and Computational Fluid Dynamics*, 24(1-4, SI):329–334, MAR 2010.

[6] M. A. Stremler and S. Basu. On point vortex models of exotic bluff body wakes. *Accepted for publication at the Fluid Dynamics Research (FDR)*, 2014.

[7] C. H. K. Williamson and R. Govardhan. A brief review of recent results in vortex-

induced vibrations. *Journal of Wind Engineering and Industrial Aerodynamics*, 96(6):713–735, 2008.

[8] D Sumner, SJ Price, and MP Paidoussis. Flow-pattern identification for two staggered circular cylinders in cross-flow. *Journal of Fluid Mechanics*, 411(1):263–303, 2000.

[9] R Govardhan and CHK Williamson. Resonance forever: existence of a critical mass and an infinite regime of resonance in vortex-induced vibration. *Journal of Fluid Mechanics*, 473:147–166, 2002.

[10] Theodore von Kármán. Über den Mechanismus des Widerstandes, den ein bewegter Körper in einer Flüssigkeit erfärt. 1. Teil. *Nachr. Ges. Wiss. Göttingen. Math.-Phys. Kl.*, pages 509–517, 1911.

[11] Theodore von Kármán. Über den Mechanismus des Widerstandes, den ein bewegter Körper in einer Flüssigkeit erfärt. 2. Teil. *Nachr. Ges. Wiss. Göttingen. Math.-Phys. Kl.*, pages 547–556, 1912.

[12] Theodore von Kármán and H. Rubach. Über den Mechanismus des Flüssigkeits- und Luftwiderstandes. *Phys. Z.*, 13:49–59, 1912.

[13] C. H. K. Williamson and R Govardhan. Vortex-induced vibrations. *Annual Review of Fluid Mechanics*, 36:413–455, 2004.

[14] R. Govardhan and C. H. K. Williamson. Modes of vortex formation and frequency response of a freely vibrating cylinder. *Journal of Fluid Mechanics*, 420:85–130, October 2000.

[15] S. Jung, K. Mareck, M. Shelley, and J. Zhang. Dynamics of a deformable body in a fast flowing soap film. *Physical Review Letters*, 97(134502):134502, September 2006.

[16] Ulrike K. Müller, Jos G. M. van den Boogaart, and Johan L. van Leeuwen. Flow patterns of larval fish: undulatory swimming in the intermediate flow regime. *Journal of Experimental Biology*, 211(2):196–205, January 2008.

[17] C. H. K. Williamson. Evolution of a single wake behind a pair of bluff bodies. *Journal of Fluid Mechanics*, 159(Oct):1–18, 1985.

[18] F. Flemming and C. H. K. Williamson. Vortex-induced vibrations of a pivoted cylinder. *Journal of Fluid Mechanics*, 522:215–252, January 2005.

[19] A. W. Maue. Zur Stabilität der Kármánschen Wirbelstrasse. *Z. Angew. Math. Mech. (ZAMM)*, 20:129–137, 1940.

[20] H Aref and M.A. Stremler. On the motion of three point vortices in a periodic strip. *Journal of Fluid Mechanics*, 314:1–25, May 1996.

[21] A. Friedmann and P. Poloubarinova. Über fortschreitende Singularitäten der ebenen Bewegung einer inkompressiblen Flüssigkeit. *Recueil de Géophysique*, Tome V, Fascicule II, Leningrad:pp. 9–23, 1928. (Russian with German summary).

[22] G. R. Kirchhoff. Vorlesungen uber mathematische physik. mechanik. page 466, 1876.

[23] Garrett Birkhoff and Joseph Fisher. Do vortex sheets roll up? *Rendiconti del Circolo matematico di Palermo*, 8(1):77–90, 1959.

[24] H Aref and MA Stremler. Four-vortex motion with zero total circulation and impulse. *Physics of Fluids*, 11(12):3704–3715, Dec 1999.

[25] Saikat Basu and Mark Stremler. Point vortex modeling of symmetric four vortex wakes. *Bulletin of the American Physical Society*, 58, 2013.

[26] S. Basu and M. A. Stremler. Mathematical modeling of symmetric wakes with four vortices per shedding period. *Manuscript to be submitted to the Theoretical and Computational Fluid Dynamics*, 2014.

[27] U. Domm. Über die wirbelstrassen von geringster instabilität. *ZAMM-Journal of Applied Mathematics and Mechanics/Zeitschrift für Angewandte Mathematik und Mechanik*, 36(9-10):367–371, 1956.

[28] H. Aref, M. A. Stremler, and F. L. Ponta. Exotic vortex wakespoint vortex solutions. *Journal of fluids and structures*, 22(6):929–940, 2006.

[29] M. A. Stremler, A. Salmanzadeh, S. Basu, and C. H. K. Williamson. A mathematical model of 2P and 2C vortex wakes. *Journal of Fluids and Structures*, 27(5-6, SI):774–783, Jul-Aug 2011.

[30] B Eckhardt and H Aref. Integrable and chaotic motions of four vortices ii. collision dynamics of vortex pairs. *Philosophical Transactions of the Royal Society of London A*, 326(1593):655–696, November 1988.

[31] S. Basu and M. A. Stremler. On the motion of two point vortex pairs with wake-inspired glide-reflective symmetry in a periodic strip. *Manuscript to be submitted to the Physics of Fluids*, 2014.

[32] Saikat Basu, Mark Stremler, Teis Schnipper, and Anders Andersen. Mathematical modeling of "2p" mode vortex wakes. *Bulletin of the American Physical Society*, 55, 2010.

[33] Saikat Basu and Mark Stremler. A mathematical model of laminar wakes with four vortices per period. In *APS Meeting Abstracts*, volume 1, page 21001, 2011.

[34] Saikat Basu, Mark Stremler, Teis Schnipper, and Anders Andersen. Modeling the dynamics of four-vortex bluff body wakes. *Bulletin of the American Physical Society*, 57, 2012.

[35] L. Prandtl and O. G. Tietjens. *Fundamentals of Hydro- and Aeromechanics*. Dover, 1934.

[36] S. Basu, M. A. Stremler, T. Schnipper, and A. Andersen. On the dynamics of vortices in experimental 2p wakes. *Manuscript to be submitted to the Journal of Fluid Mechanics*, 2014.

[37] H. Aref, M. A. Stremler, and F. L. Ponta. Exotic vortex wakes - point vortex solutions. *Journal of Fluids and Structures*, 22(6-7):929–940, Aug-Oct 2006.

[38] Max F. Platzer, Kevin D. Jones, John Young, and Joseph C. S. Lai. Flapping-wing aerodynamics: progress and challenges. *AIAA Journal*, 46(9):2136–2149, 2008.

[39] T. L. Morse and C. H. K. Williamson. Fluid forcing, wake modes, and transitions for a cylinder undergoing controlled oscillations. *Journal of Fluids and Structures*, 25(4):697–712, May 2009.

[40] MA Stremler. Relative equilibria of singly periodic point vortex arrays. *Physics of Fluids*, 15(12):3767–3775, DEC 2003.

[41] A. Khalak and C. H. K. Williamson. Motions, forces and mode transitions in vortex-induced vibrations at low mass-damping. *Journal of Fluids and Structures*, 13(7):813–851, 1999.

[42] R Bedard, M Previsic, O Siddiqui, G Hagerman, and M Robinson. Epri survey and characterization–tidal in stream energy conversion (tisec) devices. Technical report, Technical Report EPRI-TP-004 NA, EPRI, 2005.

[43] Michael M Bernitsas, Kamaldev Raghavan, Y Ben-Simon, and EM Garcia. Vivace (vortex induced vibration aquatic clean energy): A new concept in generation of clean and renewable energy from fluid flow. *Journal of Offshore Mechanics and Arctic Engineering*, 130(4):041101, 2008.

[44] Michael M Bernitsas, Y Ben-Simon, Kamaldev Raghavan, and EM Garcia. The vivace converter: model tests at high damping and reynolds number around 10^5. *Journal of Offshore Mechanics and Arctic Engineering*, 131(1):011102, 2009.

[45] JH Lee and MM Bernitsas. High-damping, high-reynolds viv tests for energy harnessing using the vivace converter. *Ocean Engineering*, 38(16):1697–1712, 2011.

[46] J. L. Synge. Mathematical investigation of the thrust experienced by a cylinder in a current, the motion being periodic. *Proceedings of the Royal Irish Academy. Section A: Mathematical and Physical Sciences*, 37:95–109, 1924.

[47] S. Michelin and S. G. Llewellyn Smith. An unsteady point vortex method for coupled fluid-solid problems. *Theoretical and Computational Fluid Dynamics*, 23(2):127–153, 2009.

[48] C. E. Brown. Effect of leading-edge separation on the lift of a delta wing. *Journal of the Aeronautical Sciences (Institute of the Aeronautical Sciences)*, 21(10), 1954.

[49] J. M. Chomaz and B. Cathalau. Soap films as two-dimensional classical fluids. *Phys. Rev. A*, 41:2243–2245, Feb 1990.

[50] M. Gharib and P. Derango. A liquid film (soap film) tunnel to study two-dimensional laminar and turbulent shear flows. *Physica D: Nonlinear Phenomena*, 37(1):406–416, 1989.

[51] R. D. Blevins. Flow-induced vibration. *New York, Van Nostrand Reinhold Co., 1977. 377 p.*, 1, 1977.

[52] W. Shyy, Y. Lian, J. Tang, D. Viieru, and H. Liu. *Aerodynamics of low Reynolds number flyers*, volume 22. Cambridge University Press, 2007.

[53] Owen M. Griffin and Steven E. Ramberg. Vortex shedding from a cylinder vibrating in line with an incident uniform flow. *Journal of Fluid Mechanics*, 75(part 2):257–271, 1976.